



저작자표시-비영리-변경금지 2.0 대한민국

이용자는 아래의 조건을 따르는 경우에 한하여 자유롭게

- 이 저작물을 복제, 배포, 전송, 전시, 공연 및 방송할 수 있습니다.

다음과 같은 조건을 따라야 합니다:



저작자표시. 귀하는 원저작자를 표시하여야 합니다.



비영리. 귀하는 이 저작물을 영리 목적으로 이용할 수 없습니다.



변경금지. 귀하는 이 저작물을 개작, 변형 또는 가공할 수 없습니다.

- 귀하는, 이 저작물의 재이용이나 배포의 경우, 이 저작물에 적용된 이용허락조건을 명확하게 나타내어야 합니다.
- 저작권자로부터 별도의 허가를 받으면 이러한 조건들은 적용되지 않습니다.

저작권법에 따른 이용자의 권리는 위의 내용에 의하여 영향을 받지 않습니다.

이것은 [이용허락규약\(Legal Code\)](#)을 이해하기 쉽게 요약한 것입니다.

[Disclaimer](#)

이학박사 학위논문

**Electrical transport of carbonized
polymer and (PV-EDOTV) copolymer**

탄화된 고분자와 (PV-EDOTV) 공중합체의
전기적 수송

2017 년 2 월

서울대학교 대학원

물리천문학부

김 경 호

Electrical transport of carbonized polymer and (PV-EDOTV) copolymer

탄화된 고분자와 (PV-EDOTV) 공중합체의
전기적 수송

지도 교수 박 영 우

이 논문을 이학박사 학위논문으로 제출함

2017 년 2 월

서울대학교 대학원

물리천문학부

김 경 호

김경호의 이학박사 학위论문을 인준함

2017 년 2 월

<u>위 원 장</u>	<u>강 병 남</u>	<u>(인)</u>
<u>부위원장</u>	<u>박 영 우</u>	<u>(인)</u>
<u>위 원</u>	<u>전 현 수</u>	<u>(인)</u>
<u>위 원</u>	<u>양 범 정</u>	<u>(인)</u>
<u>위 원</u>	<u>장 성 호</u>	<u>(인)</u>

Electrical transport of carbonized polymer and (PV-EDOTV) copolymer

Kyung Ho Kim

Supervised by

Professor Yung Woo Park

A Dissertation

Submitted to the Faculty of

Seoul National University

in Partial Fulfillment of

the Requirements for the Degree of

Doctor of Philosophy

December 2016

Department of Physics and Astronomy

Graduate School

Seoul National University

Abstract

Electrical transport of carbonized polymer and (PV-EDOTV) copolymer

Kyung Ho Kim

Department of Physics and Astronomy

The Graduate School

Seoul National University

Electrical transport in nanofibers of conducting polymers is probed by comparing its transport to that of carbonized polymer nanofibers. Also, electrical transport properties of the newly synthesized copolymer film, poly (2,5-dioctyloxy-*p*-phenylene vinylene-*alt*-3,4-ethylenedioxythiophene vinylene) are investigated. In principle, nanofibers of conducting polymers in this study, polyacetylene (PA) and polyaniline (PANI), has been a test bed of one dimensional (1D) conductors due to their inherent 1D polymer chain structures. However, ubiquitous disorders in this system complicates its analysis within the well-defined transport models. We induce dramatic changes in the 1D chain structure of polymer nanofibers by carbonizing at 800 °C and compare transport between pristine and carbonized nanofibers. Raman spectroscopy reveals that almost amorphous carbons where aromatic rings are randomly distributed are formed after carbonization as confirmed by the existence of broad graphite D and G bands. Crosslinking of adjacent polymer chains accompanying carbonization is expected to lessen the originally proposed collective transport along Luttinger liquid islands connected by intra-chain tunnel junctions. However, we found similar transport behaviors in carbonized polymer nanofibers

compared to the pristine nanofibers in terms of current-voltage characteristics in wide ranges of temperature and electric field. In the limiting transport regimes of both the Ohmic conductivity at low bias ($\frac{eV}{k_B T} \ll 1$) and the non-Ohmic conductivity at high bias ($\frac{eV}{k_B T} \gg 1$), electrical conductivity follows the Efros-Shklovskii variable range hopping (ES-VRH) conduction, which display themselves as apparent power law temperature and electric field dependences of conductance as well. Moreover, all I - V curves collapse into a single universal curve for both carbonized and pristine nanofibers. The universal curve displays power law dependence of normalized current as a function of normalized voltage, which crossovers between Ohmic and superlinear transport regimes at voltages where the carrier's electrical energy for a single hop is comparable to the carrier's thermal energy. The possibility of Luttinger liquid in conducting polymer nanofibers was solely drawn from the power law scaling and power law transport behaviors observed in these systems having in mind the 1D polymer chain structures. However, the persistency of the characteristics even after carbonization shows that the basis of the Luttinger liquid transport in polymer nanofibers is not evident. The primary finding: the universal power law scaling in the ES-VRH conduction and in the carbonized polymer nanofibers, is crucial to understand physics behind the scaling and the transport of polymer nanofibers. The universal power law scaling in the ES-VRH conduction shows that the scaling can arise from the ES-VRH, not necessarily from the Luttinger liquid. Moreover, similar transport in pristine and carbonized polymer nanofibers suggests that the ES-VRH is the dominant transport mechanism of pristine polymer nanofibers as well.

In the magneto-transport of carbonized polymer nanofibers, we observed negative magneto-conductance (MC), i.e., decrease of conductance in magnetic field, where the magnitude of MC decreases as the source-drain electric field and temperature increases. On the electric field dependence of MC, we analyze that shortening of hopping length by electric field reduces the MC. The overall behavior

of MC supports the ES-VRH conduction in carbonized nanofibers.

The magneto-resistance (MR) of a FeCl₃ doped copolymer film, poly (2,5-dioctyloxy-*p*-phenylene vinylene-*alt*-3,4-ethylenedioxythiophene vinylene), displays a crossover from negative (i.e., resistance decrease in magnetic field) to positive (i.e., resistance increase in magnetic field) values while temperature dependence of conductivity follows the ES-VRH conduction. We ascribe the crossover to the competition of the two mechanisms: the interference effect of scattered waves in the course of hopping and the shrinkage of localized electron wave function due to magnetic fields. At low magnetic fields where the interference effect is dominant and the effect of magnetic field to the wave function is not significant, negative magneto-resistance appears. Conversely, the shrinkage of wave function becomes more significant at higher magnetic field, which gives rise to the crossover to the positive MR.

.....

Kew words: Conducting polymer nanofiber, Carbonization, Universal scaling of conductance, Variable range hopping, Phenylene-vinylene-EDOT copolymer, Magneto-transport

Student number: 2009-22960

Contents

1. Introduction	1
1.1 Introduction of Conducting Polymers	1
1.2 Outline of the Thesis	3
2. Backgrounds	7
2.1 Universal Scaling and One-Dimensional Transport of Conducting Polymers	7
2.2 Variable Range Hopping Conduction.....	10
2.3 Magneto Resistance in Variable Range Hopping	14
3. Electrical Transport of Carbonized Polymer Nanofiber ...	25
3.1 Introduction.....	25
3.2 Experimental	28
3.2.1 Synthesis of Polyacetylene Nanofibers.....	28
3.2.2 Synthesis of Polyaniline Nanofibers.....	30
3.2.3 Carbonization of Polymer Nanofibers.....	30
3.2.4 Electrode Fabrication.....	31
3.2.5 Raman Spectroscopy and Electrical Measurement.....	34
3.3 Results and Discussions	34
3.3.1 Raman Spectroscopy and Carbonization.....	34
3.3.2 Conductivity, Morphology, and Air Stability.....	36
3.3.3 Measurement Using Graphene Electrodes.....	39
3.3.4 Temperature Dependence of Current-Voltage Characteristics.....	41
3.3.5 Universal Scaling of Carbonized Polymer Nanofibers.....	47

3.3.6 CPA Cross-junction.....	49
3.3.7 Threshold Voltage and Contact Resistance.....	54
3.3.8 Magneto Conductance.....	59
3.3.9 Comparison of Electrical Transport between Polymer Nanofibers and Carbonized Polymer Nanofibers.....	63
3.4 Conclusion	66
4. Electrical Transport of Poly (2,5-dioctyloxy-<i>p</i>-phenylene vinylene-<i>alt</i>-3,4-ethylenedioxythiophene vinylene)	75
4.1 Introduction.....	75
4.2 Experimental	77
4.2.1 Sample Preparation.....	77
4.2.2 Doping and Electrical Measurements.....	78
4.3 Results and Discussion.....	78
4.3.1 Pristine and Doped Copolymer.....	78
4.3.2 Temperature Dependence of Conductivity.....	80
4.3.3 Magneto Resistance.....	82
4.4 Conclusion.....	87
5. Conclusion.....	93

List of Figures

1.1	Conductivity of conducting polymers..	2
1.2	Optical microscope images and polymer structures of dispersed PA and PANI nanofibers.....	3
2.1	Schematic of biased asymmetric double well potential coupled with environment.....	8
2.2	A simulated curve of Eq. 2.1.	8
2.3	The energy-momentum diagram illustrating the Efros-Shklovskii VRH.	12
2.4	Two simulated wave functions of $\psi(x) = \exp(-x/\xi)$ centered at $x = 0$ and $x = 10$..	15
2.5	Schematic of charge carrier hopping from site A to site B with other sites between the two.....	18
3.1	The universal power law scaling behavior (Eq. 2.1) of PA and PANI nanofibers.....	27
3.2	Magneto-conductance ($\Delta I/I$) of PA, PANI, PT nanofibers at 1.5 K.....	27
3.3	Possible cross-linking processes of PA and PANI during carbonization up to 800 °C.....	28
3.4	Photograph of aligned PA film and SEM image of the film.....	29
3.5	Experimental flow of carbonized polymer nanofiber measurement.....	31
3.6	AFM images of CPA with Ti/Au electrodes on top and CPANI with Ni/Au electrodes on top.	31

3.7	Optical microscope image of patterned epitaxial graphene electrodes grown on SiC.....	33
3.8	Schematic of the fabrication process of graphene electrodes.....	33
3.9.	Raman spectra of PA, PANI, CPA, and CPANI nanofibers.	34
3.10	Relation between crystallite size L_a and the ratio I_D/I_G and the full width at half maximum (FWHM) of G band.....	36
3.11	G mode (E_{2g}) is the stretching motion of sp^2 carbons and the D mode (A_{1g}) is the breathing motion of aromatic rings	36
3.12	Conductivities ($T > 200$ K) and diameters of 17 PA, 9 PANI, 33 CPA, and 15 CPANI two-probe devices.....	37
3.13	Statistics of conductivity and diameter of 17 PA, 9 PANI, 33 CPA, and 15 CPANI devices.	38
3.14	Morphology retaining carbonization of PANI nanofibers and change of diameters after carbonization.	38
3.15	Stability of CPANI nanofibers in a simple nitrogen box.	39
3.16	Comparison of room temperature conductivity of PANI nanofibers on graphene and on Au electrodes.....	40
3.17	AFM phase images of CPANI fibers on graphene electrodes and I - V measurement	41
3.18	I - V (E - J) characteristics of CPA and CPANI nanofibers..	44
3.19	The temperature dependence of the Ohmic conductance at low bias voltages and the bias electric field dependence of the non-Ohmic conductance at low temperatures ($T < \sim 10$ K) and high voltages ($V > \sim 1$ V).....	45

3.20	Temperature dependence of conductance at various fixed source-drain voltages and the voltage dependence of conductance at various fixed temperatures in the CPA nanofiber.....	45
3.21	Temperature dependence of conductance at various fixed source-drain voltages and the voltage dependence of conductance at various fixed temperatures in the CPANI nanofiber.....	46
3.22	Universal scaling of CPA and CPANI nanofibers.	47
3.23	I - V curves of CPA and CPANI nanofibers plotted in log-log scale.	49
3.24	SEM images of CPA cross junction devices.....	50
3.25	Temperature dependence of I - V characteristics for the CPA-2 nanofiber....	51
3.26	Temperature dependence of the Ohmic conductance for the CPA-2 nanofiber.	52
3.27	Temperature dependence of I - V characteristics for the CPA-3 nanofiber ...	52
3.28	The bias voltage dependence of the non-Ohmic conductance at low temperatures ($T < 10$ K) and high voltages ($V > \sim 20$ V) of the CPA-3 nanofiber...	53
3.29	Temperature dependence of I - V characteristics in linear scale for the cross-junction between the CPA-2 and the CPA-3 nanofibers.....	53
3.30	I^*dV/dI vs V plot of the CPA-1, CPA-2, CPA-3, and the cross-junction between the CPA-2 and the CPA-3 nanofibers and evaluated threshold voltages...	56
3.31	I^*dV/dI vs V plot of the CPANI nanofiber (CPANI-1) at 1.5 K and 6 K.....	56
3.32	Current vs $(V-V_t)/V_t$ plot in double logarithmic scale for CPA-1, CPA-2, CPA-3, and CPANI-1 nanofiber.....	57
3.33	Two-probe and four-probe measurements of a typical carbonized polymer	

nanofiber at room temperature	58
3.34 MC at fixed source-drain voltages of the CPA nanofiber (CPA-1) for at 1.5 K, 10 K, and 20 K.	61
3.35 MC at fixed source-drain voltages of the CPANI nanofiber (CPANI-1) for at 1.5 K, 6 K, 10 K, 20 K, and 50 K.....	62
3.36 Comparison of universal scaling between pristine and carbonized polymer nanofibers.....	64
4.1 Synthesis scheme for poly(phenylene-vinylene-EDOT-vinylene) copolymer.	75
4.2 Schematics of drop casting of the polymer solution and subsequent solution doping.....	77
4.3 Current density vs electric field curve of a pristine polymer film and doping time dependence of conductance.....	79
4.4 XPS spectra of pristine and FeCl ₃ -doped (PV-EDOTV) copolymer film.	80
4.5 The temperature-dependence of conductivity of the FeCl ₃ -doped (PV-EDOTV) copolymer film	81
4.6 MR of the FeCl ₃ -doped (PV-EDOTV) copolymer film at 1.4, 3.2, and 6.8 K up to 35 T.....	82
4.7 Resistance change at 1.4 K due to magnetic field 35 tesla.....	83
4.8 The temperature-dependence of fitting parameters $ \alpha $ and β in Eq. (4.2).	85

List of Tables

3.1	Fitting parameters of pristine and carbonized polymer nanofibers.....	65
-----	---	----

Chapter 1

Introduction

1.1 Introduction of Conducting Polymers

Electronically conducting polymers form a new class of conducting materials that had been considered as insulators. The conducting plastic is called synthetic metals¹ and as of now, a variety of conducting polymers has been developed and studied with considerable attention². The property of electrical conductivity in polymers was first discovered in 1977, where the conductivity of a polyacetylene (PA) film increased dramatically upon AsF₅ doping³. Conducting polymers consist of macromolecules which have long hydrocarbon chains with bond alternating (single and double bond) structures, which leads delocalized π -electrons responsible for electrical conduction. The energy eigenvalues of the π -electron forms an energy gap between the highest occupied molecular orbitals (HOMO) and the lowest unoccupied molecular orbitals (LUMO), which coerces most of the un-doped conducting polymers semiconducting. The chemical redox reactions between conjugated polymers and dopants such as halogen or alkali atoms supply charge carriers, producing localized donor and acceptor impurity states between LUMO and HOMO, which is termed doping same as that in conventional semiconductors. Interestingly, the range of conductivity of conducting polymers span from that of insulators to platinum⁴ and both the intrinsic metallic and non-metallic properties such as linear temperature dependence of thermopower⁴ and negative temperature coefficient of resistance⁴ have been observed in conducting polymers. Moreover, unique and exotic charge excitations such as solitons^{5,6}, polarons⁶, and bipolarons⁶ due to electron-phonon interaction have been explored in these systems. One example of the exotic properties of the

soliton is the inverse spin-charge relation where charged soliton has spin zero and the neutral soliton has spin 1/2. In principle, polymer nanofibers are simple quasi 1D systems composed of weakly coupled 1D chains. However, in practice, ubiquitous disorder in real samples complicates the analysis of the intrinsic charge transport with the well-defined 1D transport models. In this standpoint, the morphology of conjugated polymers is one of the most crucial factors determining electrical transport. For instance, electrical transport properties of individual polymer nanofibers and that of films are different; conducting polymer nanofibers such as PA, polyaniline (PANI), polythiophene (PT), and polypyrrole (PPY) nanofibers show non-linear current-voltage characteristics⁷⁻¹¹, whereas generally Ohmic conduction for films⁴. In application point of view, several proof of concept devices based on conductive polymers have been shown that span a great range of applications including flexible field-effect transistors¹², actuators¹³, sensors¹⁴, and nano-optoelectronic devices¹⁵.

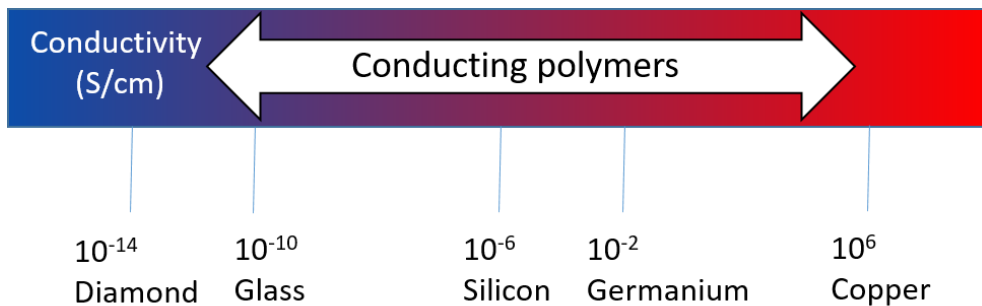


Figure 1.1 Conductivity of conducting polymers

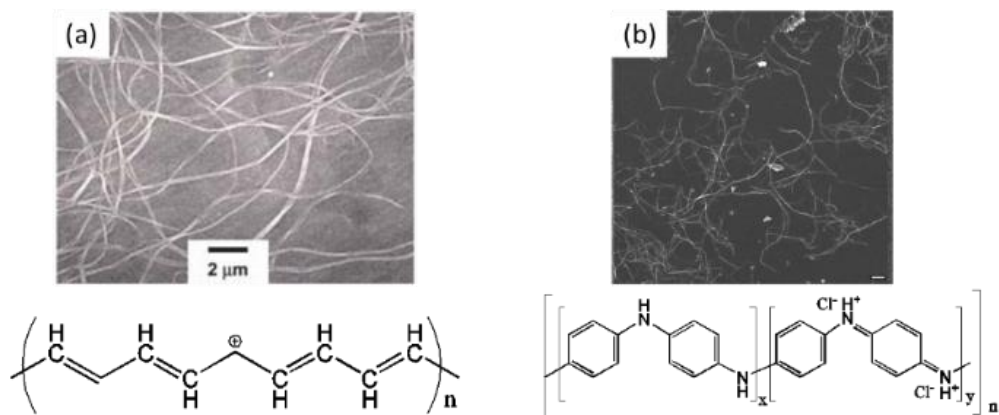


Figure 1.2 Optical microscope images and polymer structures of dispersed PA (a) and PANI (b) nanofibers. Scale bar of (b) is 1 μm . Under the optical images are positively charged soliton of PA (a) and emeraldine salt form of PANI by hydrochloric acid doping (b). (a) and (b) are adapted from ref. [16] with permission of Royal Society of Chemistry and ref. [17] (Copyright (2008) American Chemical Society), respectively.

1.2 Outline of the Thesis

In this dissertation, we investigated electrical transport of polymer systems: carbonized PA and PANI nanofibers¹⁸ and a copolymer film, poly (2,5-dioctyloxy-*p*-phenylene vinylene-*alt*-3,4-ethylenedioxythiophene vinylene) ((PV-EDOTV) copolymer), where phenylene and 3,4-ethylenedioxythiophene (EDOT) is alternatively linked by vinylene units¹⁹. Electrical transport properties are probed in the large range of electric field, magnetic field, and temperatures in these systems.

The thesis is divided by five chapters. In chapter one, introduction of conducting polymer and the scope of the thesis is presented. Theoretical backgrounds used in this thesis are in chapter two and electrical transport properties of carbonized polymer nanofibers and comparison of electrical transport between pristine and carbonized polymer nanofibers are described in chapter three¹⁸. Currently, there is

no consensus on the dominant transport mechanism of polymer nanofibers. In chapter three, we discuss the electrical transport of carbonized polymers where dramatic changes in the structure of conducting polymer nanofibers were taken place by carbonization at 800 °C, transforming the original polymer structure into quasi-amorphous carbon network, yet retaining its nanofibrila morphology. Despite the profound modifications to the 1D polymer chain structure, we found remarkably similar transport properties in the nanofibers before and after carbonization by means of current-voltage (I - V) measurements in the range of $1.5 < T < 300$ K: highly non-linear I - V characteristics, power law dependence of $I(V) \propto V^\beta$ at high bias voltages ($eV \gg k_B T$) and $G(T) \propto T^\alpha$ at low voltages ($eV \ll k_B T$), and universal scaling of conductance. We argue that the unexpected similarity of transport between pristine and carbonized polymers emphasize the importance of carrier localization in polymer nanofibers, and that the transport mechanism of polymer nanofibers for the past reports in literature, is hopping like.

In chapter four, we discuss the electrical transport properties of a newly designed (PV-EDOTV) copolymer film doped by FeCl_3 ¹⁹. The FeCl_3 doped copolymer film follows variable range hopping (VRH) conduction with magnetoresistance (MR) crossover from negative to positive in the VRH conduction regime. The MR in VRH conduction is an interesting topic including quantum physics.

The application of the Efros-Shklovskii VRH (ES-VRH) to both the carbonized polymer nanofibers and the FeCl_3 -doped copolymer film is an interesting result. The ES-VRH conduction has been conventionally applied to inorganic doped semiconductors where a soft gap in the density of states near Fermi level arises from Coulomb interactions. Carrier localization in carbonized polymer nanofibers and the doped copolymer film due to the ubiquitous disorder forming amorphous structures gives rise to the ES-VRH conduction in these polymer systems. In chapter five, the conclusion of the dissertation is described.

Bibliography

1. S. C. Rasmussen, On the origin of ‘synthetic metals’. *Materials Today* (2016).
2. A. J. Heeger, Semiconducting polymers: the Third Generation. *Chem. Soc. Rev.* **39**, 2354 (2010).
3. C. K. Chiang, *et al.*, Electrical conductivity in doped polyacetylene. *Phys. Rev. Lett.* **39**, 1098 (1977).
4. A. B. Kaiser, Systematic conductivity behaviour in conducting polymers: Effect of heterogeneous disorder. *Adv. Mater.* **13**, 927 (2011).
5. A. J. Heeger, S. Kivelson, , J. R. Schrieffer, and, W. P. Su, Solitons in conducting polymers. *Rev. Mod. Phys.* **60**, 781 (1988).
6. J. L. Bredas, and G. B. Street, Polarons, Bipolarons and Solitons in Conducting Polymers. *Acc. Chem. Res.* **18**, 309 (1985).
7. A. Choi, *et al.* Suppression of the magneto resistance in high electric fields of polyacetylene nanofibers. *Synth. Met.* **160**, 1349 (2010).
8. J. G. Park, *et al.* Tunneling conduction in polyacetylene nanofiber. *Synth. Met.* **135–136**, 299 (2003).
9. A. B. Kaiser, and Y. W. Park, Comparison of tunnelling conduction in polyacetylene nanofibres, CDW and SDW systems. *Synth. Met.* **135–136**, 245–247 (2003).
10. A. Choi, *et al.* Probing spin-charge relation by magnetoconductance in one-dimensional polymer nanofibers. *Phys. Rev. B* **86**, 155423 (2012).
11. A. N. Aleshin, H. J. Lee, Y. W. Park, and K. Akagi, One-Dimensional Transport in Polymer Nanofibers. *Phys. Rev. Lett.* **93**, 196601 (2004).

12. A. N. Aleshin, J. Y. Lee, S. W. Chu, J. S. Kim, and Y. W. Park, Mobility studies of field-effect transistor structures based on anthracene single crystals. *Appl. Phys. Lett.* **84**, 5383 (2004).
13. E. Smela, E. W. H. Jager, and O. Inganäs, Microfabricating Conjugated Polymer Actuators. *Science* **290**, 1540 (2000).
14. J. Janata, and M. Josowicz, Conducting polymers in electronic chemical sensors. *Nat. Mater.* **2**, 19 (2003).
15. H. Sirringhaus, N. Tessler, and R. H. Friend, Integrated Optoelectronic Devices Based on Conjugated Polymers. *Science* **280**, 1741 (1998).
16. M. Kyotani, *et al.* Entanglement-free fibrils of aligned polyacetylene films that produce single nanofibers. *Nanoscale* **2**, 509 (2010).
17. H. D. Tran, Y. Wang, J. M. D'Arcy, and R. B. Kaner, Toward an understanding of the formation of conducting polymer nanofibers. *ACS Nano* **2**, 1841 (2008).
18. K. H. Kim, S. Lara-Avila, H. Kang, H. He, J. Eklöf, S. J. Hong, M. Park, K. Moth-Poulsen, S. Matsushita, K. Akagi, S. Kubatkin, and Y. W. Park, Apparent power law scaling of variable range hopping conduction in carbonized polymer nanofibers. *Sci. Rep.* **6**, 37783 (2016).
19. K. H. Kim, A. Choi, J.-M. Park, S. J. Hong, M. Park, I.-H. Lee, E.-S. Choi, A. B. Kaiser, T.-L. Choi, and Y. W. Park, Magnetoresistance of a copolymer: FeCl₃-doped poly(2,5-dioctyloxy-*p*-phenylene vinylene-*alt*-3,4-ethylenedioxythiophene vinylene). *Synth. Met.* **188**, 30 (2014).

Chapter 2

Backgrounds

2.1 Universal Scaling and One-Dimensional Transport of Conducting Polymers

Unification of electrical transport in conducting polymers, regardless of films or nanofibers, has been demonstrated in an expression formula frequently used to fit the macroscopic current:

$$I = I_0 T^{\alpha+1} \sinh\left(\frac{\gamma e V}{k_B T}\right) \left| \Gamma\left(\frac{1+\beta}{2} + \frac{i\gamma e V}{2\pi k_B T}\right) \right|^2 \quad (2.1)$$

, where I_0 , α , β , γ are the fitting parameters, k_B is the Boltzmann constant, e is the electron charge, and $\Gamma(x)$ is the gamma function¹⁻⁶. The expression for macroscopic current described by Eq. 2.1 has its origin in the microscopic description of electron transfer rates for dissipative tunneling in Caldeira-Leggett models⁷⁻⁹. In a nutshell, these entail an asymmetric biased double-well potential (Fig. 2.1), in which the tunneling rates from the metastable well slightly higher in energy is driven by the coupling to the full phonon bath.

The fitting parameter $I_0 \propto \Delta^2 / \omega^{\alpha+2}$ is proportional to the tunneling frequency Δ and inversely proportional to the characteristic frequency in each well ω . α and β are related to the dissipation coupling strength between the electron and the phonon bath. γ^{-1} is related to the number of tunneling events needed for the charge carriers to traverse the distance between electrodes. In the temperature dependence of conductance, the fitting parameters α and β are the exponents of the

temperature dependence of conductivity, $G(T) \propto T^\alpha$ and the voltage dependence of current, $I(V) \propto V^\beta$, respectively.

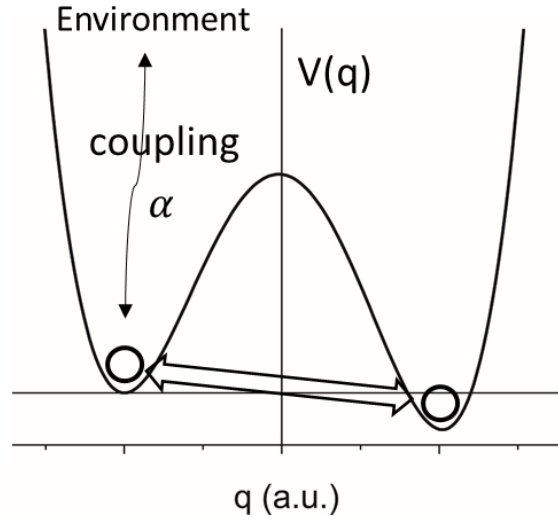


Figure 2.1 Schematic of biased asymmetric double well potential coupled with environment with dissipation coupling strength α and electron tunneling between the two wells. The ball is the electron

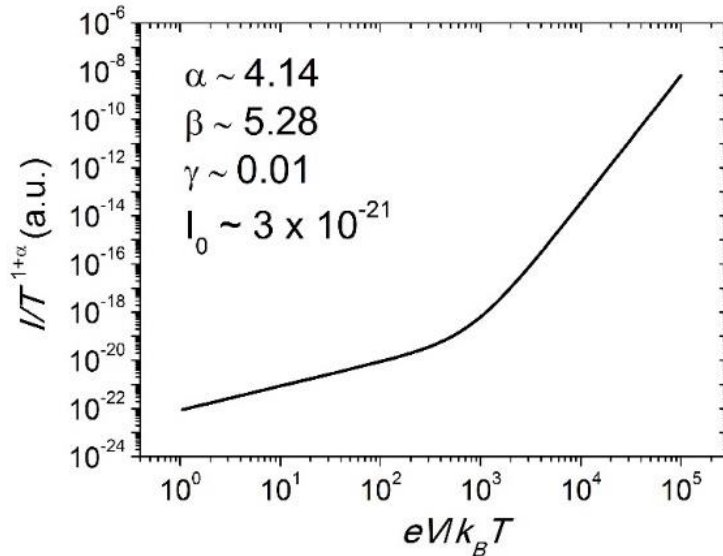


Figure 2.2 A simulated curve of Eq. 2.1 with fitting parameters written in the Figure. It displays power law scaling with a change of slopes.

The functional form of Eq. 2.1 has been observed in a variety of 1D or quasi-1D systems such as carbon nanotubes^{10,11}, MoSe nanowires¹², gold nanowires¹³, NbSe₃ nanowires¹⁴, and Nb₂PdS₅ nanowires¹⁵, and polymer nanofibers^{1,3,16,17}. More generally, Eq. 2.1 is also useful in the phenomenological description of macroscopic quantum tunneling, such as Josephson currents in superconductors, and the tunneling of the magnetic flux within the ring of superconducting quantum interference devices (SQUIDs)^{18,19}. Thus, Eq. 2.1 appears as a very versatile expression that encompasses the physics of a variety of systems and transport mechanisms.

Though Eq. 2.1 has its microscopic origin in dissipative quantum tunneling, fitting the macroscopic current in quasi-1D conducting polymer nanofibers or films and a variety of quasi-1D organic and inorganic nanowires to Eq. 2.1 has been interpreted as tunneling between 1D Luttinger liquids (LL). LL is the 1D electron liquid where Coulomb interaction leads to collective transport^{20,21}. The motion of electrons in 1D is inherently collective because there is no bypass, which breaks down the Fermi liquid quasiparticle theory that enables description of interacting particles as non-interacting quasiparticles.

In the LL interpretation of Eq. 2.1, the power law dependence of conductance arises from the power law suppression of tunneling density of states as a function of energies: temperature (T) and voltage (V) due to the collective motion^{20,21}. However, fitting to Eq. 2.1 alone cannot guarantee that the system forms LL, although currents in LL systems satisfy Eq. 2.1⁵. Experimentally, the scaling of Eq. 2.1 has also been observed beyond 1D systems in conducting polymer films such as poly(2,5-bis(3-tetradecylthiophen-2-yl)thieno[3,2-b]thiophene) (PBTTT)^{2,4,6} and poly(3,4-ethylenedioxythiophene)-poly(styrene sulfonate) (PEDOT:PSS)^{2,5}. Accordingly, theories such as polaron hopping in semiconducting polymers², environmental Coulomb blockade (ECB)^{1,5,11,22} and VRH²³⁻²⁵ have been developed to explain these findings. The theory of polaron hopping is based on the dissipative tunneling in the

biased double well potential arising from semiconducting polymer's polaronic effects². ECB is also a dissipative quantum tunneling phenomenon where the charging energy to the isolated metallic island blocks quantum tunneling in the coupling with environments²². The theory of VRH to the Eq. 2.1 take account of influences of electric field where the electric potential energy compensates for the thermal activation energy²⁴. Also correlation with the effective temperature in the VRH and the universal scaling has been raised²³.

Depending on the context, one can assign meanings to the fitting parameters. For instance, in the case of 1D VRH, γ^{-1} is related to L/ξ , where ξ is the localization length and L is the sample length, and α is a function of the number of hops²⁵. In the context of electron tunneling into LL, γ^{-1} is the number of tunneling barriers with the constraints that $\beta = \alpha + 1$ and $\gamma^{-1} = 1$ in single tunneling^{1,3,6,10,12,13,26}; for polaron hopping mediated by nuclear tunneling in semiconducting polymers, γ^{-1} represents the number of hopping events needed for the charge carriers to traverse the distance between electrodes and $\beta = \alpha + 1$ ². These models have all in common α , the exponent of the temperature dependence of conductivity, $G(T) \propto T^\alpha$ and β , the exponent of the voltage dependence of current, $I(V) \propto V^\beta$.

2.2 Variable Range Hopping Conduction

Variable range hopping (VRH) is the hopping conduction between localized states in both organic and inorganic doped semiconductors^{27,28,29}. The term variable range hopping indicates variable hopping length in real space, as a function of temperature or electric field. In semiconductors and polymers, the conduction at high temperature is thermally activated. Therefore, in principle, if the energy difference between neighboring states in real space is larger than thermal activation energy $k_B T$ at low enough temperature, charges (electron or hole) near Fermi level hardly find sites to hop. However, it is still conducting because some other sites that are farther away in

real space require lower activation energy. This is because the energy difference between localized states i and j can be expressed:

$$\Delta E_{ij} = \frac{1}{g(E_F)r_{ij}^d} \quad (2.2)$$

, where $g(E_F)$ is the density of states at the Fermi level, r_{ij} is the distance between the two sites, and d is the dimensionality. In this case, the charge has to tunnel longer distances for the expense of smaller energy difference. Consequently, the hopping length varies as temperature. In total, the hopping conductance can be expressed

$$\sigma = \sigma_0 \exp \left[-\frac{2r}{\xi} - \frac{\Delta E}{k_B T} \right] \quad (2.3)$$

, where ξ is the localization length, or the effective Bohr radius, and r is the hopping length. Maximizing conductivity by optimizing the two terms in the exponential, hopping distance take the form

$$r \propto \xi \left(\frac{T_M}{T} \right)^{1/4} \quad (2.4)$$

, where $T_M = \frac{18}{k_B g(E_F) \xi^d}$ is the Mott characteristic temperature. The resulting conductivity is

$$\sigma = \sigma_0 \exp \left[-\left(T_M / T \right)^{1/4+1} \right] \quad (2.5)$$

In the presence of high Coulomb potential energy²⁷⁻³² between electron and hole left behind during hopping, assuming^{30,31} $E_j - E_i \ll \frac{e^2}{\epsilon r}$, ΔE is simply replaced by Coulomb potential energy $e^2/\epsilon r$, where ϵ is the dielectric permittivity, then the hopping distance optimizing the conductivity is

$$r \propto \xi \left(\frac{T_{ES}}{T} \right)^{1/2} \quad (2.6)$$

, where $T_{ES} = \frac{2.8e^2}{k_B \epsilon \xi}$ is the Efros-Shklovskii (ES) characteristic temperature. Now the conductivity takes the form of Mott 1D VRH (Eq. 2.5) even in higher dimensions.

$$\sigma = \sigma_0 \exp \left[- (T_{ES}/T)^{1/2} \right] \quad (2.7)$$

, where 1/2 in the exponent comes from derivative of $1/r$ in the Coulomb potential energy difference. In this regime, Coulomb interaction between the hopped carrier and the opposite charge left behind requires energy to overcome, which creates energy gap in the density of states called Coulomb gap. Inserting parabolic density of states in Eq. 2.2 also leads to Eq. 2.7. At higher temperatures, thermal activation higher than the Coulomb gap washes out this gap and the Mott VRH recovers.

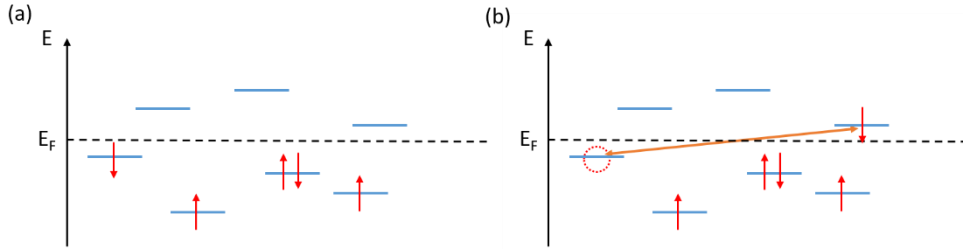


Figure 2.3 The Energy-momentum diagram illustrating the Efros-Shklovskii variable range hopping conduction between localized states where the excitonic Coulomb interaction between hopped charge and the opposite charge left behind is considered.

Temperature dependence in Eq. 2.5, the Mott VRH, is slower than that of simple thermal activation,

$$\sigma = \sigma_0 \exp \left[-\frac{\Delta E}{k_B T} \right] \quad (2.8)$$

, which is exponentially dependent on temperature. The simple thermal activation is called nearest neighbour hopping because at high enough temperatures, the value of the tunnelling term in Eq. 2.3 ($-2r/\xi$) is much higher than that of the simple activation term ($-\Delta E/k_B T$). Therefore, tunnelling to longer distance is not favourable at high temperatures. Consequently, it jumps to nearest neighbour in real-space, which is the first priority, i.e., the determining factor of choosing sites to hop is the distance in real space. However, as temperature decreases, the simple activation term ($-\Delta E/k_B T$) is now comparable to the tunnelling term in Eq. 2.3 ($-2r/\xi$), which is manifested by the crossover from the simple thermal activation to the Mott-VRH or the ES-VRH. At much lower temperatures, the thermal activation term ($-\Delta E/k_B T$) is much higher than the tunnelling term ($-2r/\xi$), which coerces the hopping length to increase to find optimal sites that reduces the thermal activation energy as much as possible. In this sense, as the portion of tunnelling independent of temperature becomes higher in the Mott-VRH and the ES-VRH, the temperature dependence is weaker than that of simple thermal activation. If we compare the Mott-VRH and the ES-VRH, the temperature dependence in the Mott-VRH is faster than that of the ES-VRH as the Coulomb interaction decelerates the temperature dependence of conductivity. It means that the portion of tunnelling in the ES-VRH is larger than that of the Mott-VRH. The Coulomb interaction energy forces the carrier to tunnel longer distances than in the Mott-VRH.

In the presence of both high Coulomb potential energy and high electric field^{30–35}, electric potential energy eEr is added: $\Delta E = e^2/\epsilon r - eEr$. Note that the electric potential energy due to the external electric field alleviate the Coulomb attraction

and reduces the activation energy. Eq. 2.3, thus, has maximum when $E < \frac{2k_B T}{e\xi}$

and the conductivity is dependent on both temperature and electric field. When $E > \frac{2k_B T}{e\xi}$, the condition $\Delta E = e^2/\varepsilon r - eEr > 0$ limits the maximum

conductivity. Therefore, when $\Delta E < 0$, as the applied electric field increase, only the first term in Eq. 2.3 ($-2r/\xi$) influences the conductivity. This requires

cancelling out of thermal activations, $\Delta E = 0$, or $r \propto \xi \sqrt{\frac{E_{ES}}{E}}$, where

$$E_{ES} \propto \frac{k_B T_{ES}}{e\xi}. \quad (2.9)$$

. The resulting conductivity follows,

$$\sigma = \sigma_0 \exp\left[-(E_{ES}/E)^{1/2}\right] \quad (2.10)$$

. This expression is independent of temperature.

2.3 Magneto Resistance in Variable Range Hopping

Magnetoresistance (MR) in this thesis is defined by $[R(B) - R(0)]/R(0)$. The ordinary MR in normal metals is due to the Lorentz force which drives the charge to move forward with drawing helix³⁶. The Lorentz force effectively reduces the speed of charges by a factor of $1 + (\mu B)^2 = 1 + (\omega_c \tau)^2$, where μ is the mobility, B is the magnetic field, ω_c is the cyclotron frequency, and τ is the scattering time, which leads to positive MR (i.e., increase of resistance in magnetic field).

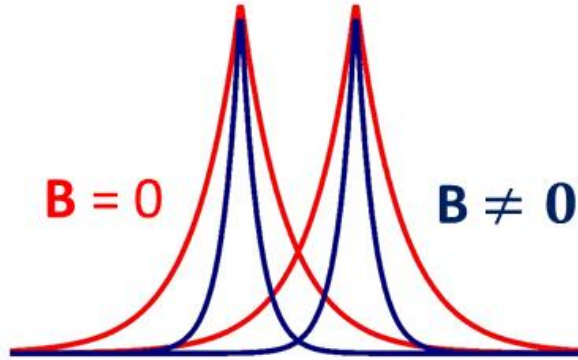


Figure 2.4 Two simulated wave functions of $\psi(x) = \exp(-\frac{x}{\xi})$ centered at $x = 0$ and $x = 10$. The overlap of tails of the two wave functions is related to the tunneling of electron between the two sites. In magnetic field, the wave function shrinks and the overlap decreases.

Conversely, charge carriers are localized in impurity sites such as near dopants due to Coulomb interactions or due to disorders in doped semiconductors and polymer materials. Therefore, the situation is different from that of normal metals in VRH conduction. First of all, motion of electrons is not diffusive; it is thermally activated between localized states, called phonon assisted tunneling. It is an insulator at zero temperature because no free carriers exist. Consequently, the electron wave function localized near dopants or local crystalline sites has been modelled as a hydrogen-like electron wave function that is spherically symmetric²⁹. In this model, the localized wave functions decay exponentially as the distance from the center increases (Fig. 2.4). Remarkably, small perturbations in the tail of wave function influence charge transport dramatically, as the overlap of the wave functions which is represented in the tunnelling term in Eq. 2.3 ($-2r/\xi$) changes significantly. Accordingly, this effect is more considerable at low temperatures where small changes in wave function results in exponentially large MR because the increased hopping distance reduces overlap of the two wave functions at low temperatures.

When uniform external magnetic field in z-direction is applied to the bound electron, the localized electron wave function shrinks in radial direction. We explain here that the shrinkage of wave function originates from the diamagnetic effect that attracts the electron inside. If we express potential energy of a bound electron in a magnetic field as

$$-e^2/\epsilon r - \vec{\mu} \cdot \vec{B} \quad (2.11)$$

, where $\vec{\mu}$ is the magnetic moment, the first term is the Coulomb energy, and the second term is from the interaction between the magnetic dipole moment of the electron and magnetic field. The magnetic moment is composed of two contributions,

$$\vec{\mu} = \vec{\mu}_L + \vec{\mu}_B \quad (2.12)$$

, where the former is due to the angular momentum which is the paramagnetic term, $\vec{\mu}_L$, and the latter is the magnetic moment from the magnetic induction. The additional magnetic moment $\vec{\mu}_B$ is induced by external magnetic field, causing additional potential energy $-\vec{\mu}_B \cdot \vec{B}$. Remarkably, the induced magnetic moment is proportional to the strength of magnetic field and opposite to the field direction. Therefore,

$$\vec{\mu}_B \propto -(x^2 + y^2)\vec{B} \quad (2.13)$$

. Note that the wave function in uniform magnetic field is cylindrically symmetric because the wave function in the absence of magnetic field is spherically symmetric. Consequently, the paramagnetic moment do not change the electron wave function because the eigen-function of L_z (angular momentum in z direction) is $\partial/\partial\varphi$, where φ is the azimuthal angle. Whereas $-\vec{\mu}_B \cdot \vec{B} \propto [-B(x^2 + y^2)] \cdot B$ is positive and represents the potential energy of a harmonic oscillator $F = -k\sqrt{(x^2 + y^2)}$, where

$k = m\omega^2$ and $\omega = \frac{eB}{2m}$, where m is the mass, and k is the spring constant. Therefore,

there is an attractive force toward the center and the wave function shrinks as the magnetic field increases. This shrinkage reduces overlap of wave functions and the resistance of the system increases as a function of the magnetic field.

The potential energy due to $-\vec{\mu}_B \cdot \vec{B}$ is just that of harmonic oscillators²⁹. Therefore, roughly the wave function shrinks by a factor of

$$\Psi(\sqrt{x^2 + y^2}) \propto \exp\left(-\frac{x^2 + y^2}{4\lambda^2}\right) \quad (2.14)$$

, where $\lambda = \sqrt{\hbar/eB}$ is the magnetic length. Therefore, according to literature²⁹, at low magnetic field, where $\lambda \gg \xi$ and $(x^2 + y^2)^{1/2} \ll \lambda^2/\xi$,

($B \ll \frac{6\hbar}{e\xi^2(T_0/T)^{1/2}}$ ³⁷ in the ES-VRH and $B \ll \frac{\hbar[g(E_F)k_B T]^{1/4}}{e\xi^{5/4}}$ in the Mott VRH),

$$\ln[\rho(B)/\rho(0)] = t\left(\xi^4/\lambda^4\right)(T_0/T)^p \quad (2.15)$$

, where $t = 0.0015$ and $p = 3/2$ in the ES-VRH, $t = 5/2016$ and $p = 1/4$ in the Mott VRH ($T_0 = T_{ES}$ or T_{Mott}).

At high magnetic field²⁹, where $\lambda \ll \xi$ and $(x^2 + y^2)^{1/2} \gg \lambda^2/\xi$,

($B \gg \frac{6\hbar}{e\xi^2(T_0/T)^{1/2}}$ ³⁷ in the ES-VRH and $B \gg \frac{\hbar[g(E_F)k_B T]^{1/4}}{e\xi^{5/4}}$ in the Mott VRH),

$$\ln[\rho(B)/\rho(0)] = \left[2.1 \frac{eH}{g(E_F)\hbar\xi_H k_B T}\right]^{1/3} \quad (2.16)$$

,where ξ_H is the localization length in magnetic field is for the Mott VRH. For the ES-VRH²⁹,

$$\ln[\rho(B)/\rho(0)] = \left[3.17 \frac{e^2}{\varepsilon (\lambda^2 \xi_H)^{1/3} T} \right]^{3/5} \quad (2.17)$$

. The diamagnetic effect of the positive MR is dominant when typical energy difference between hopping sites is considerable with the on-site Coulomb energy³⁸. In this regime, only hopping from singly occupied sites to unoccupied sites are possible and spin alignment due to the magnetic field³⁹ hardly gives the MR effect. However, when the typical energy difference between hopping sites is much higher than the on-site Coulomb interaction energy, spin-alignment effect suppresses hopping because only singlet is allowed due to the Pauli exclusion principle. The MR due to the spin-alignment effect saturates at high magnetic fields as whole spins are aligned in the direction of magnetic field³⁹.

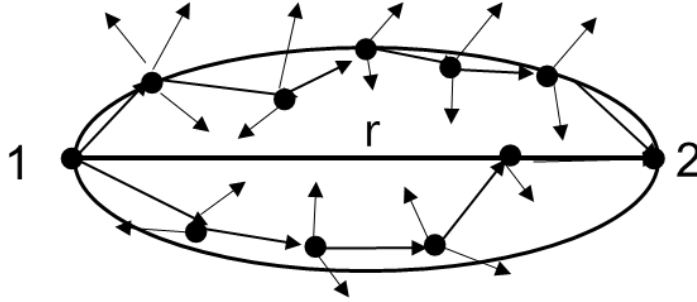


Figure 2.5 Schematic of charge carrier hopping from site A to site B with other sites between the two. The electron hopping from A to B scatters from other sites during tunneling paths and each path interferes at sites two.

Negative MR (resistance decrease, i.e., conductance increase, due to magnetic field) also appears in the VRH conduction⁴⁰⁻⁴³. Conventionally, the negative MR in disordered *metals* is due to time-reversal trajectories⁴⁴. This entails breakdown

of quantum correction in time-reversal trajectories in weak localization regime. If an electron moves from position A to B undergoing scatterings to scatterers such as phonons, defects and charged impurities, many configurations of scattering trajectories from A to B are possible. Among these configurations, self-intersecting trajectories interfere constructively at the intersecting point, which enhances backscattering compared to the classical transport. In magnetic fields, the constructive interference in the self-intersecting trajectory breaks down due to the phase difference in magnetic field, which leads negative MR.

In VRH conduction, the electron is strongly localized, not diffusive. However, the possibility of similar quantum interference effect has been considered. According to the literature, it is possible because the localized electron seeks favorable hopping sites that are far away, leaving many localization sites in between at sufficiently low temperature⁴⁵⁻⁵⁰ and because the hopping is the thermally assisted *tunneling*. When the electron hops, it *tunnels* undergoing scatterings from other localized sites in between (Fig. 2.5). Therefore, there are many configurations of scattering paths in a single hop similar with in diffusive disordered metals. But self-intersecting path are rare because the scattered wave function is not propagating but exponentially decaying. Consequently, the weak localization effect is small. Instead, the conductivity of highly resistive samples is determined by the largest resistance in the resistance network model, where the macroscopic resistance is determined by the percolation through microscopic resistance networks. The fact that the conductivity is exponentially dependent (sensitive) on this highest resistance part leads the system sensitive to the destructive interference. Magnetic field suppresses the destructive interference which mostly contribute to the macroscopic resistance, increasing the macroscopic conductivity. This effect is linear^{46,47,49} with respect to the magnetic field except at very small magnetic field^{48,50} as the phase factor in magnetic field is proportional to the flux.

Bibliography

1. A. N. Aleshin, H. J. Lee, Y. W. Park, and K. Akagi, One-Dimensional Transport in Polymer Nanofibers. *Phys. Rev. Lett.* **93**, 196601 (2004).
2. K. Asadi, *et al.* Polaron hopping mediated by nuclear tunnelling in semiconducting polymers at high carrier density. *Nat. Commun.* **4**, 1710 (2013).
3. A. Choi, *et al.* Probing spin-charge relation by magnetoconductance in one-dimensional polymer nanofibers. *Phys. Rev. B* **86**, 155423 (2012).
4. E. S. H. Kang, and E. Kim, Multi-barrier field-emission behavior in PBTBT thin films at low temperatures. *Sci. Rep.* **5**, 8396 (2015).
5. A. J. Kronemeijer, *et al.* Universal scaling in highly doped conducting polymer films. *Phys. Rev. Lett.* **105**, 20 (2010).
6. J. D. Yuen, *et al.* Nonlinear transport in semiconducting polymers at high carrier densities. *Nat. Mater.* **8**, 572 (2009).
7. G. Hermann, and U. Weiss, Quantum tunneling rates for asymmetric double-well systems with ohmic dissipation. *Phys. Rev. Lett.* **54**, 1605 (1985).
8. M. P. A. Fisher, and A. T. Dorsey, Dissipative quantum tunneling in a biased double-well system at finite temperature. *Phys. Rev. Lett.* **54**, 1609 (1985).
9. A. O. Caldeira, and A. J. Leggett, Influence of dissipation on quantum tunneling in macroscopic systems. *Phys. Rev. Lett.* **49**, 1545 (1982).
10. M. W. Bockrath, *et al.* Luttinger-liquid behavior in carbon nanotubes. *Science* **397**, 4 (1999).
11. A. Bachtold, *et al.* Suppression of tunneling into multiwall carbon nanotubes.

- Phys. Rev. Lett.* **87**, 166801 (2001).
12. L. Venkataraman, Y. S. Hong, and P. Kim, Electron transport in a multichannel one-dimensional conductor: Molybdenum selenide nanowires. *Phys. Rev. Lett.* **96**, 1 (2006).
 13. U. Chandni, P. Kundu, S. Kundu, N. Ravishankar, and A. Ghosh, Tunability of electronic states in ultrathin gold nanowires. *Adv. Mater.* **25**, 2486 (2013).
 14. E. Slot, M. A. Holst, H. S. J. Van Der Zant, and S. V. Zaitsev-Zotov, One-dimensional conduction in charge-density-wave nanowires. *Phys. Rev. Lett.* **93**, 1 (2004).
 15. W. Ning, *et al.* Nonlinear transport in quasi-one-dimensional Nb₂PdS₅ nanowires. *Appl. Phys. Lett.* **105**, 172603 (2014).
 16. Z. Zhou, *et al.* One-dimensional electron transport in Cu-tetracyanoquinodimethane organic nanowires. *Appl. Phys. Lett.* **90**, (2007).
 17. A. Avnon, *et al.* Quasi one dimensional transport in individual electrospun composite nanofibers. *AIP Adv.* **4**, 017110 (2014).
 18. G. L. Ingold, H. Grabert, and Eberhardt, U. Cooper-pair current through ultrasmall Josephson junctions. *Phys. Rev. B* **50**, 395 (1994).
 19. D. Massarotti, *et al.* Macroscopic quantum tunnelling in spin filter ferromagnetic Josephson junctions. *Nat. Commun.* **6**, 7376 (2015).
 20. S. Jezouin, *et al.* Tomonaga-Luttinger physics in electronic quantum circuits. *Nat. Commun.* **4**, 1802 (2013).
 21. A. Imambekov, T. L. Schmidt, and L. I. Glazman, One-dimensional quantum liquids: Beyond the Luttinger liquid paradigm. *Rev. Mod. Phys.* **84**, 1253 (2012).

22. M. H. Devoret, *et al.* Effect of the electromagnetic environment on the Coulomb blockade in ultrasmall tunnel junctions. *Phys. Rev. Lett.* **56**, 2419 (1986).
23. H. Abdalla, K. van de Ruit, and M. Kemerink, Effective temperature and universal conductivity scaling in organic semiconductors. *Sci. Rep.* **5**, 16870 (2015).
24. L. Li, N. Lu, and M. Liu, Physical origin of nonlinear transport in organic semiconductor at high carrier densities. *J. Appl. Phys.* **116**, 164504 (2014).
25. A. S. Rodin, and M. M. Fogler, Apparent power-law behavior of conductance in disordered quasi-one-dimensional systems. *Phys. Rev. Lett.* **105**, 106801 (2010).
26. M. Sassetti, and U. Weiss, Transport of 1D Interacting Electrons Through Barriers and Effective Tunnelling Density of States. *Europhys. Lett.* **27**, 311 (2007).
27. N. F. Mott, and E. A. Davis, *Electronic processes in non-crystalline materials.* (1971).
28. A. L. Efros, and B. I. Shklovskii, Coulomb gap and low temperature conductivity of disordered systems. *J. Phys. C Solid State Phys.* **8**, L49 (1975).
29. B. I. Shklovskii, and A. L. Efros, *Electronic properties of doped semiconductors.* (1984).
30. V. N. Prigodin, and A. J. Epstein, Comment on ‘Voltage-Induced Metal-Insulator Transition in Polythiophene Field-Effect Transistors’. *Phys. Rev. Lett.* **98**, 259703 (2007).
31. D. Yu, C. Wang, B. L. Wehrenberg, and P. Guyot-Sionnest, Variable range hopping conduction in semiconductor nanocrystal solids. *Phys. Rev. Lett.* **92**,

- 216802 (2004).
32. A. S. Dhoot, G. M. Wang, D. Moses, and A. J. Heeger, Voltage-induced metal-insulator transition in polythiophene field-effect transistors. *Phys. Rev. Lett.* **96**, 246403 (2006).
 33. N. Ikrelief, D. Bourbie, and K. Driss-Khodja, On the inverse field dependence of conductivity in disordered organic materials. *Appl. Phys. Lett.* **97**, 022101 (2010).
 34. L. V. Govor, I. A. Bashmakov, K. Boehme, and J. Parisi, Electrical field dependence of hopping conduction in self-organized carbon networks. *J. Appl. Phys.* **91**, 739 (2002).
 35. J. H. Wei, Y. L. Gao, and X. R. Wang, Inverse square-root field dependence of conductivity in organic field-effect transistors. *Appl. Phys. Lett.* **94**, 073301 (2009).
 36. A. B. Pippard, *Magneto-resistance in metals*. (1989).
 37. R. Rosenbaum, T. Murphy, E. Palm, S. Hannahs, and B. Brandt, Magnetoresistance of insulating amorphous NixSi1-x films exhibiting Mott variable-range hopping laws. *Phys. Rev. B* **63**, 94426 (2001).
 38. K. A. Matveev, L. I. Glazman, P. Clarke, D. Ephron, and M. R. Beasley, Theory of hopping magnetoresistance induced by Zeeman splitting. *Phys. Rev. B* **52**, 5289 (1995).
 39. A. Kurobe, and H. Kamimura, Correlation effects on variable range hopping conduction and the magnetoresistance. *J. Phys. Soc. Jpn.* **51**, 1904 (1982).
 40. M. Jaiswal, W. Wang, K. A. S. Fernando, Y.-P. Sun, and R. Menon, Magnetotransport in transparent single-wall carbon nanotube networks. *Phys. Rev. B* **76**, 113401 (2007).

41. J. Zhu, *et al.* Carbon nanostructure-derived polyaniline metacomposites: Electrical, dielectric, and giant magnetoresistive properties. *Langmuir* **28**, 10246 (2012).
42. M. Salvato, *et al.* Low temperature conductivity of carbon nanotube aggregates. *J. Phys. Condens. Matter* **23**, 475302 (2011).
43. N. V. Agrinskaya, and V. I. Kozub, Suppression of negative magnetoresistance in Coulomb gap regime: quantum interference and spin effects in CdTe. *Phys. Stat. Sol* **205**, 11 (1998).
44. P. A. Lee, and T. V. Ramakrishnan, Disordered electronic systems. *Rev. Mod. Phys.* **57**, 287 (1985).
45. L. B. Ioffe, and B. Z. Spivak, Giant magnetoresistance in the variable range hopping regime. *JETP* **117**, 551 (2013).
46. B. I. Shklovskii, and B. Z. Spivak, *Scattering and Interference Effects in Variable Range Hopping Conduction*. (1991).
47. W. Schirmacher, Quantum-interference magnetoconductivity in the variable-range-hopping regime. *Phys. Rev. B* **41**, 2461 (1990).
48. M. E. Raikh, and G. F. Wessels, Single-scattering-path approach to the negative magnetoresistance in the variable-range-hopping regime for two-dimensional electron systems. *Phys. Rev. B* **47**, 15609 (1993).
49. V. L. Nguen, B. Z. Spivak, and B. I. Shklovskii, Tunnel hopping in disordered systems. *Sov. Phys. JETP* **62**, 1021 (1985).
50. U. Sivan, O. Entin-Wohlman, and Y. Imry, Orbital magnetoconductance in the variable range hopping regime. *Phys. Rev. Lett.* **60**, 1566 (1988).

Chapter 3

Electrical Transport of Carbonized Polymer Nanofiber

3.1 Introduction

While probing intrinsic transport mechanism of conducting polymers is of utmost importance, its intrinsic behaviour is obstructed by inter-fibril contacts, inter-chain contacts, and structural disorders in the intra-chain level^{1,2}. For example, PA film consists of entangled nanofibrils; each nanofiber consists of 100 – 1000 PA polymer chains that are stacked with disorders. Beyond the inside of the nanofiber, the inter-fibril contact resistance hinders the intrinsic conductivity¹. However, with the advances of chemical synthesis³⁻⁷, dispersion methods⁸, and nanolithography technologies, measurement of electrical transport in a single nanofiber has been pursued for the past decades⁹. Electrical transport of polymer nanofibers can be explained within the frame of VRH¹⁰, electric field induced tunnelling¹¹⁻¹⁴, manifestation of LL and ECB^{15,16}. However, still there is no consensus on the dominant transport mechanism in polymer nanofibers. In this stage, the universal scaling in Eq. 2.1 has been observed commonly in various polymer nanofibers. Figure 3.1 displays the universal power law scaling behaviour of current in both PA and PANI single nanofibers¹⁶. All I - V curves collapse into the scaling function of Eq. 2.1 with power law dependence of $G(T) \propto T^\alpha$ and $I(V) \propto V^\beta$. As introduced in chapter 2.1, this power law scaling behaviour has been interpreted as the evidence

of Coulomb interaction in 1D conduction¹⁵⁻¹⁹. Moreover, in polymer nanofibers, local quasi-particle excitations such as soliton, polaron, and bipolaron due to electron-phonon interaction plays important roles in charge transport^{11,16,20,21}. Especially, soliton excitations are expected in PA due to the degenerate ground state, and polaron and bipolaron excitations in PANI and PT nanofibers due to the non-degenerated ground state^{16,20}. Figure 3.2 shows magneto-conductance (MC) of PA, PANI, and PT nanofibers, displaying only MC of PA becomes zero [Fig. 3.2(a,d)], which has been interpreted as the evidence of soliton conduction because the charged soliton has spin zero, different from electron spin of $1/2$ ^{11,16}. Therefore, the scaling in Fig. 3.1 might be the evidence of Coulomb interaction between solitons in PA, and polarons and bipolarons in PANI and PT quasi 1D nanofibers^{15,16}.

In this chapter, we discuss the charge transport of polymer nanofibers by probing their carbonized counterparts. Figure 3.3 shows the suggested cross-linking processes in carbonized PA (CPA)²² and carbonized PANI (CPANI) nanofibers^{23,24}. The carbonization is performed by the pyrolysis method of hydrocarbons in inert atmosphere²²⁻³⁰. This accompanies dehydrogenation and cross-linking processes, which dramatically modify the inherent 1D structure of polymer chains. In carbonized polymer nanofibers, local excitations in pristine polymer nanofibers are no longer possible. Therefore, comparison of charge transport between pristine and carbonized nanofibers including the effect of quasi-particle excitations and Coulomb interactions are expected to give insights to understand physics behind the electrical transport of polymer nanofibers. Experimental details are described in chapter 3.2 and electrical transport of carbonized polymers together with comparison of charge transport between pristine and carbonized polymer nanofibers are discussed in chapter 3.3. Conclusion of this chapter is given in chapter 3.4.

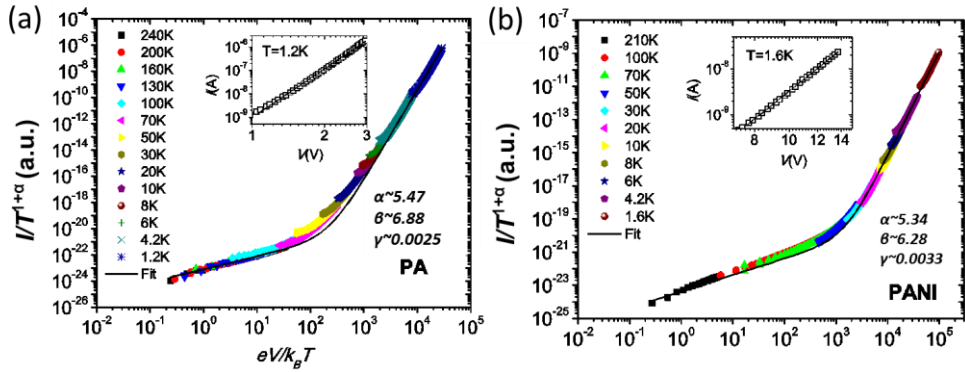


Figure 3.1 The universal power law scaling behavior (Eq. 2.1) PA (a) and PANI (b) nanofibers. Inset Figures display power law dependence of I - V curves at 1.5 K scaled in double logarithmic scales. The Figure is adapted from ref. [16].

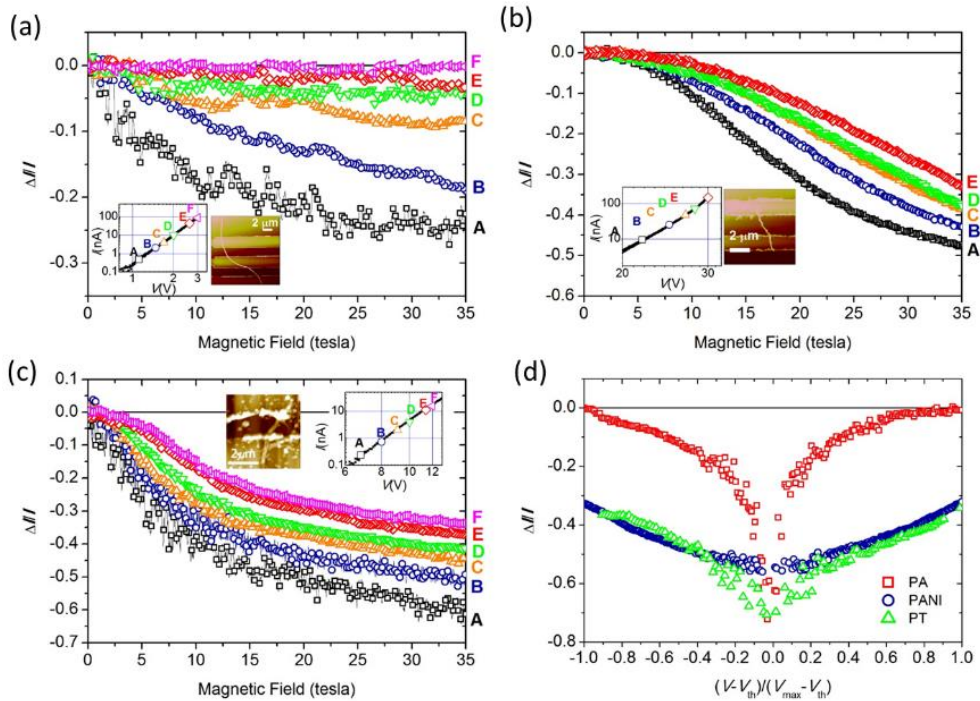


Figure 3.2 Magneto-conductance ($\Delta I/I$) of PA (a), PANI (b), PT (c) nanofibers at 1.5 K. Inset Figures are AFM images of the fibers on top of 2 μm width Pt electrodes and I - V curves at 1.5 K. (d) Magneto-conductance at 1.5 K and 14 tesla as a function of normalized voltages. Magneto-conductance of PA is distinctively approaches to zero at high voltages. Adapted from ref [16]

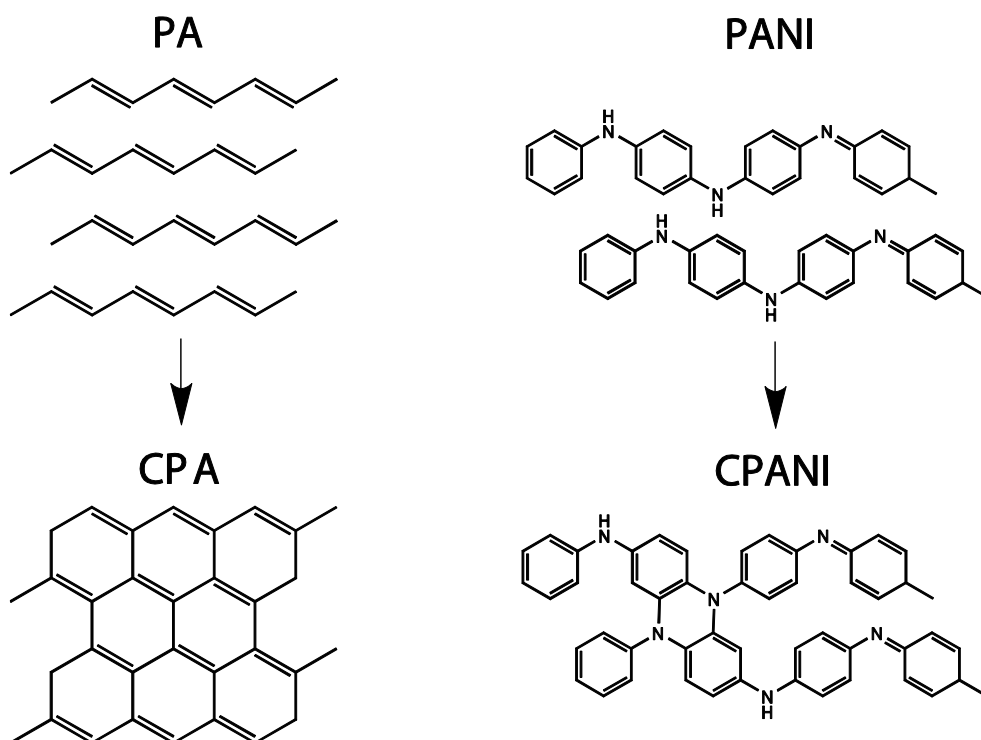


Figure 3.3 Possible cross-linking processes of PA (adapted from ref.[22]) and PANI (adapted from ref.[23], [24]) during carbonization up to 800 °C.

3.2 Experimental

3.2.1 Synthesis of Polyacetylene Nanofibers

PA nanofibers have been produced according to standard protocols. The conventional PA film (Shirakawa method and modified Shirakawa method) is composed of randomly entangled fibrils, which obstructs the dispersion of one fibril. However, advances in synthesis technology using liquid crystals have enabled controlling of morphologies of PA films^{3,4,6}. Nematic and chiral nematic liquid crystals as solvents of catalyst produce ordered reaction fields, giving aligned fibrils

and helically ordered fibrils, respectively. We used the aligned PA film for the easiness of dispersion. The aligned PA film was synthesized from acetylene gas of six-nine grade using a nematic liquid crystal as a solvent for the Ziegler–Natta catalyst, $\text{Ti}(\text{O}-n\text{-Bu})_4/\text{AlEt}_3$. The concentration of $[\text{Ti}]$ was 50 mmol/l and the mole ratio of the co-catalyst, $[\text{Al}]/[\text{Ti}]$, was 4. The nematic liquid crystal was the equimolar mixture of two kinds of phenylcyclohexyl derivatives, *para*-(*trans*-4-*n*-propylcyclohexyl) ethoxybenzene (PCH302) and *para*-(*trans*-4-*n*-propylcyclohexyl) butoxybenzene (PCH304). The nematic liquid crystal containing the catalyst was aligned at 10 °C through gravity flow to make an aligned reaction field on the glass wall of a Schlenk flask. The polymerization was carried out at 10 °C on the reaction field by introducing the acetylene gas for about 30–53 min into the flask. The initial pressure of the acetylene gas was 509–511 Torr. The aligned PA film synthesized was washed with distilled toluene, methanol solution containing 1 N hydrochloric acid, and distilled toluene in turn at room temperature under flowing argon gas, and then was dried in vacuum on a Teflon sheet⁶. The aligned PA film was synthesized from Akagi group in Kyoto University and I received it for the experiment⁶.

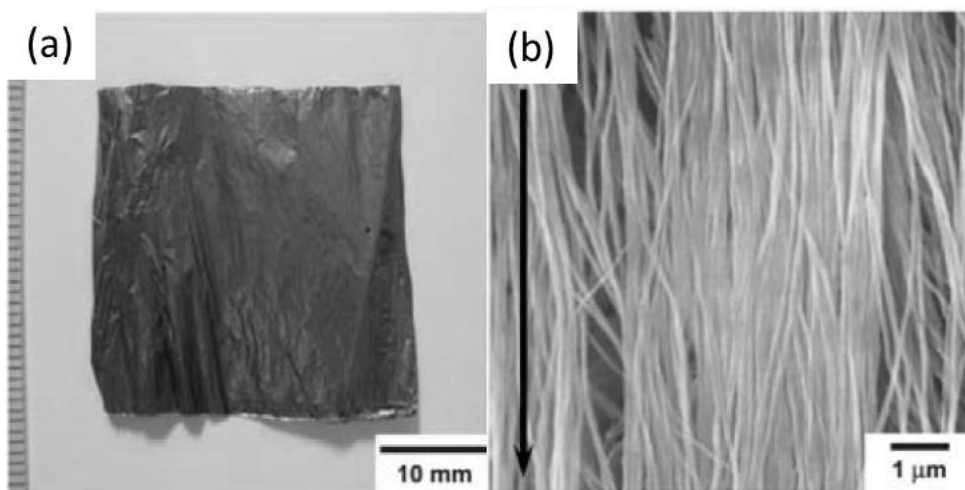


Figure 3.4 Photograph of aligned PA film (a) and scanning electron microscope (SEM) image of the film (b). Adapted with permission from ref. [6] (Copyright (2010) Royal Society of Chemistry).

3.2.2 Synthesis of Polyaniline Nanofibers

PANI has unique redox chemistry where doping and de-doping is reversibly controlled by acid and base, respectively^{5,7}. Emeraldine base form of PANI changes to the salt-form upon acid doping. We synthesized hydrogen chloride (HCl) doped emeraldine salt PANI nanofibers by rapidly mixing aqueous acidic solution of ammonium peroxydisulfate with aqueous acidic solution of aniline and catalytic amount of *p*-phenylenediamine as a promoter for fiber growth. 3.2 mmol of aniline monomers was added in 10 mL of 1N hydrochloric acid and 5 mg of *p*-phenylenediamine was dissolved in small amount of methanol. The two solutions were mixed and the resultant solution was added to the solution of 0.8 mmol of Ammonium peroxydisulfate in 10 mL of 1 N hydrochloric acid. The resulting solution was violently shaken for 10 seconds and left for 1 day⁷.

3.2.3 Carbonization of Polymer Nanofibers

The aligned PA film was dispersed in *N,N*-Dimethylformamide (DMF) with ultrasonication. The entanglement-free fibrils are easily dispersible in organic solvents without surfactant. The dispersed PA nanofibers were drop casted on $6 \times 6 \text{ mm}^2$ Si / SiO₂ (300 nm) substrates and doped by gaseous iodine for one hour. Iodine doping of PA films increase carbonization yield in the subsequent pyrolysis step, preventing thermal decomposition by promoting cross-linking of PA chains upon hydrogen iodide gas removal^{22,27,28}. This iodine doping process is essential for carbonization of PA because without iodine doping, only morphology-less carbons are produced^{29,31,32}. As PANI is already dispersed in solution, nanofibers of PANI were casted on Si/SiO₂ (300 nm) by drop and blowing. Pyrolysis of nanofibers for both drop casted PA and PANI nanofibers took place in a tube furnace at 800 °C for 1 hour under nitrogen flow with 1 °C / min of both heating and cooling ramp rate. Heating time at 800 °C was one hour.

3.2.4 Electrode Fabrication

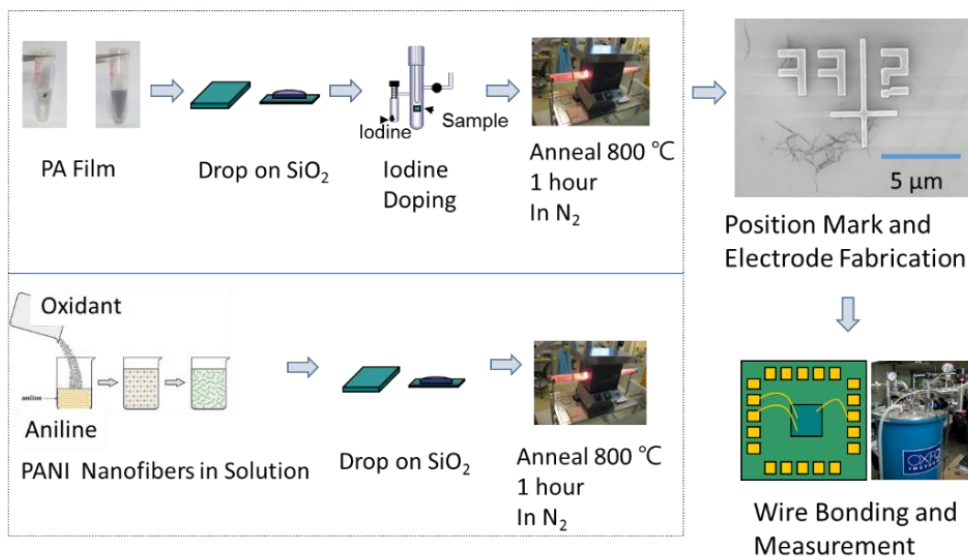


Figure 3.5 Experimental flow of carbonized polymer nanofiber measurement. The synthesized fibers are dispersed on SiO₂ substrates and heated in a tube furnace in inert atmosphere. Position markers and electrodes are patterned using conventional e-beam lithography and electrically connected by gold wire bonding. The 14 T superconducting magnet with the 6517 electrometer were used for measurement. Figure of PANI nanofiber synthesis is adapted with permission from ref. [7] (Copyright (2008) American Chemical Society)

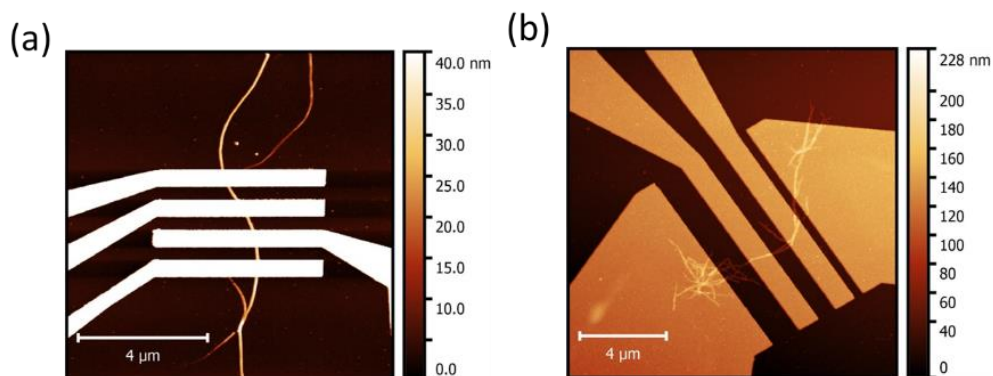


Figure 3.6 AFM images of CPA with Ti/Au electrodes on top (a) and CPANI with Ni/Au electrodes on top (b).

Carbonized polymer nanofibers are randomly distributed on substrates. Accordingly, choosing and locating well separated and long fibers on the substrate is the first step. We fabricated position markers on the substrate after carbonization by standard electron beam (e-beam) lithography to locate one nanofiber. In detail, poly(methylmethacrylate) (PMMA) (EL6 and A2 double layer) is used as a positive resist and marker drawing is performed by Jeol JDX9300 EBL. The pattern is developed by wet etching technique (IPA:H₂O = 93:7 solution for ~4 min). Metal position markers (Ti/Au (5/95 nm)) are evaporated and lifted-off in acetone. Using optical microscope equipped with a CCD camera, pictures of fibers with position markers are used for electrode design in CAD. The same processes used for position marker fabrication is repeated for electrodes on top of fibers in four probe geometry with different metals Ti/Au (5/95 nm), Ni/Au (50/50 nm), Pd (50 nm) (Fig. 3.6).

We also have used graphene as an electrode material. Figure 3.7 displays optical and AFM images of graphene electrodes. We patterned monolayer graphene epitaxially grown on SiC substrates. Graphene is a perfectly flat metal which is good for contacting with nanofibers³³⁻⁴¹. π - π interaction between graphene and sp² carbon materials is expected to promote the quality of contact between the nanofiber and the electrode. We used aluminum (Al) for a protection mask to prevent PMMA residues on top of the electrodes. After deposition of 20 nm of Al on top of monolayer epitaxial graphene on SiC, ZEP-520A (100 nm) was spin-coated and electrodes were patterned by e-beam lithography. The exposed area was developed (oxylene for 1 min) and the Al underneath was wet etched by MF-319 for ~5 sec or dry etched by Cl plasma (Cl, SiCl₄, and Ar, 10 sccm each, for 50 sec). Graphene was etched by oxygen plasma (50 W, 1 min) and ZEP was rinsed by N-Methyl-2-pyrrolidone (NMP). Metal pads for wire bonding was fabricated as shown in Fig. 3.8. PMMA (EL6 and A2 double layer) was coated and standard e-beam lithography was performed. With standard metal evaporation and lift off technique, Ti/Au pads linking graphene electrodes to the electrometers are defined (Fig. 3.7 and 3.8).

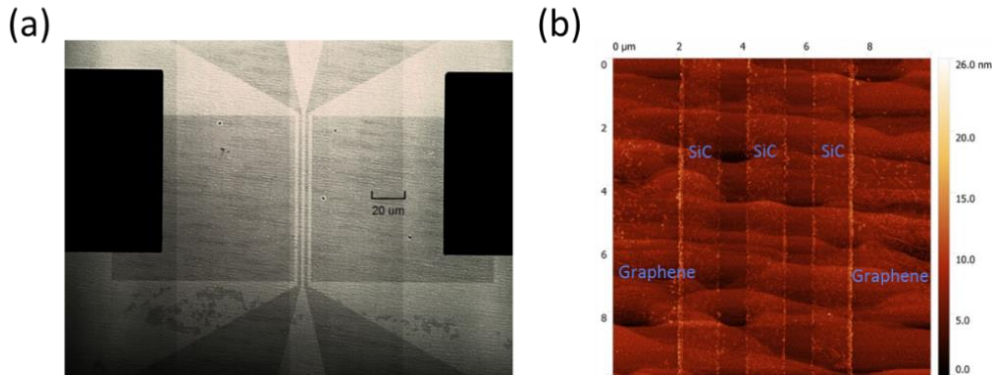


Figure 3.7 (a) Optical microscope image of patterned epitaxial graphene electrodes grown on SiC. Dark patches on graphene are bilayer patches and the black rectangles are Ti/Au pads. (b) AFM topography image of patterned graphene electrode.

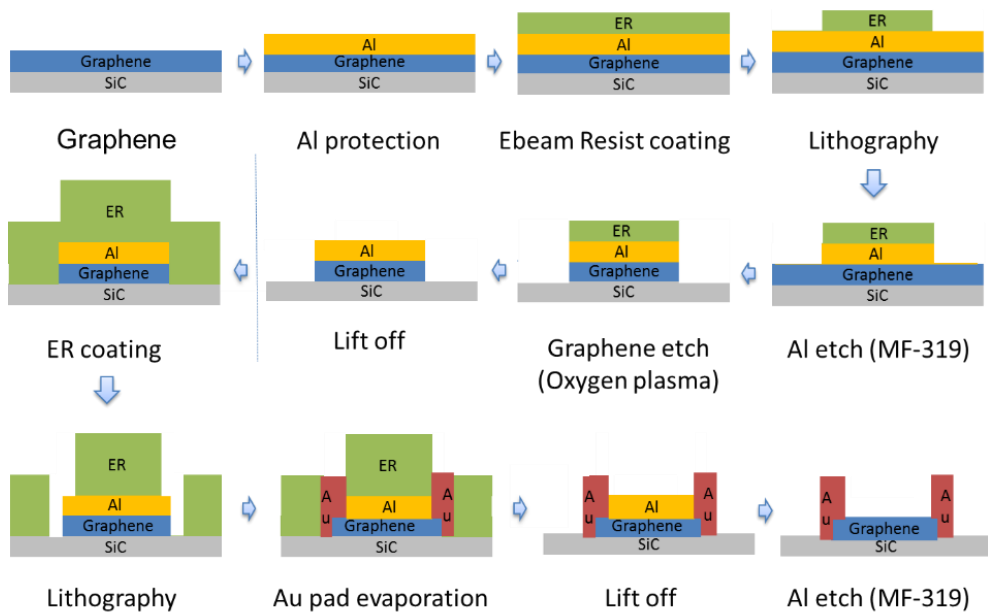


Figure 3.8 Schematic of the fabrication process of graphene electrodes in Figure 3.7.

3.2.5 Raman Spectroscopy and Electrical Measurement

Structural characterization was carried out by Raman spectroscopy, performed on bundles of pristine polymer nanofibers (iodine doped PA and HCl doped PANI) and on carbonized polymer nanofibers drop casted on Si/SiO₂ substrates using a Horiba scientific Raman spectrometer equipped with a spotsize $\sim 1 \mu\text{m}$ ($\lambda = 638 \text{ nm}$). The electrical integrity of the SiO₂ dielectric during the high temperature step was verified at room temperature with measurements in three-terminal source-drain-gate configuration with a Keithley Semiconductor Characterization System 4200. Temperature dependence of the current-voltage (I - V) characteristic was measured in two-probe geometry with a Keithley 6517 electrometer using an Oxford Instruments Maglab system for measurements at temperatures between 1.5 K and 300 K.

3.3 Results and Discussions

3.3.1 Raman Spectroscopy and Carbonization

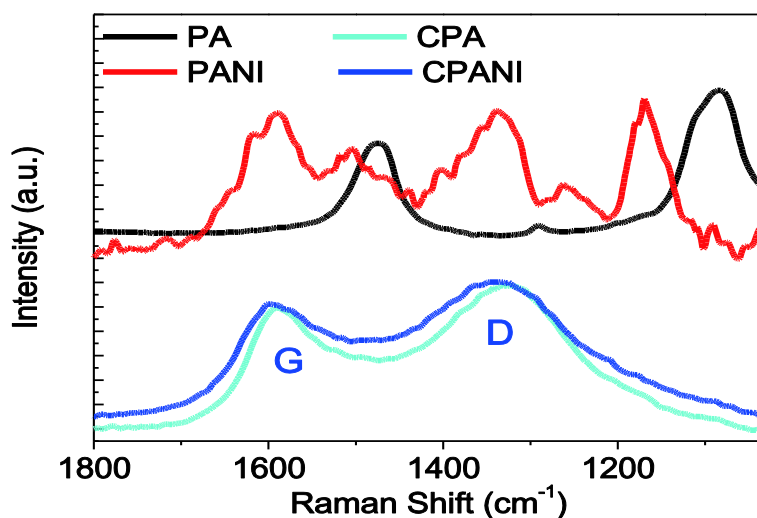


Figure 3.9 Raman spectra of PA and PANI nanofibers show characteristic peaks of trans-PA at 1475 and 1085 cm^{-1} and complex peaks of HCl doped PANI. After carbonization, broad graphite G and disordered D bands were observed in both CPA and CPANI nanofibers. Data for PA and PANI are normalized with respect to the intensity of D band and shifted for clarity.

Figure 3.9 shows the Raman spectra measured on bundles of pristine and carbonized polymer nanofibers on Si/SiO₂ substrates. Before carbonization, we observed characteristic Raman peaks of trans-PA at 1475 and 1085 cm⁻¹ ⁴² which are assigned to C=C stretching vibration and mixed vibration of C-C stretching and C-H in plane bending, respectively^{27,28,42,43}. For HCl doped PANI nanofibers, characteristic peaks at 1620, 1590, 1505, 1405, 1340, 1260, and 1170 cm⁻¹ were observed (1620: C-C stretching of the benzenoid ring, 1590: C-C stretching vibration in the quinonoid ring, 1505: N-H deformation vibration associated with the semi-quinonoid structures, 1405: substituted phenazine segments, 1340: C-N⁺ vibration of the delocalized polaronic structures, 1260: quinonoid forms, 1170 cm⁻¹: C-H bending vibration of the semi-quinonoid rings²³). After carbonization, both nanofibers show broad bands which have local maximum at 1320 (1340) cm⁻¹ and 1590 (1600) cm⁻¹ for CPA (CPANI) which are assigned to disordered (D) and graphitic (G) bands of graphite, corresponds to the breathing mode of aromatic rings and the stretching motion of sp² carbon atoms, respectively. In perfect graphite, G peak is sharp and no D peak appears because the breathing mode is quenched in perfect crystalline structures⁴⁴. Therefore, D peak indicates the degree of defects in almost crystalline case. However, in amorphous carbons, linewidths of the D and G peaks broaden and the D band intensity is proportional to the number of aromatic rings not defects in crystallites⁴⁴⁻⁴⁷. The broad linewidths (FWHM > 100 cm⁻¹) of the G band and the relative intensities of D and G bands I_D/I_G = 1.2 in both carbonized nanofibers indicate that the sp² cluster size is smaller than 1 nm (Fig. 3.10)⁴⁴⁻⁴⁷. The small sp² crystallite size in carbonized polymers, and the evidence by previous XRD^{22,27,28,30}, TEM³² and spectroscopic studies^{22-24,27,28,30} on PA^{22,27,28,32} and PANI^{23,24,30} carbonized under the same conditions, support that carbonization of polymers yields cross-linked polymer chains forming amorphous carbon networks (Fig. 3.3). The carbonized polymers are not crystallized yet as the graphitization occurs at 2600 °C^{22,27,28,30}, which means that carbonized polymers are quasi-amorphous networks of hexagonal carbon bonds.

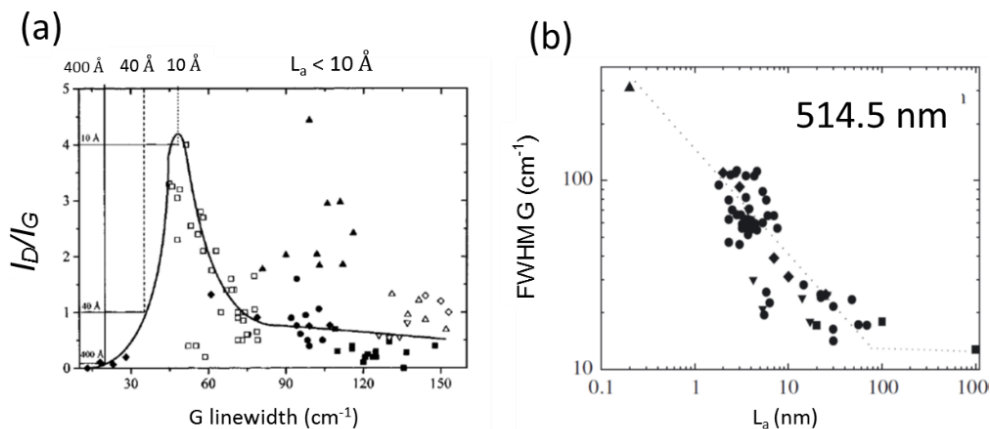


Figure 3.10 Relation between crystallite size L_a and the ratio I_D/I_G (a, adapted from ref. [45] of American Institute of Physics©) and the full width at half maximum (FWHM) of G band (b, adapted from ref. [46] with permission of the Royal Society©)

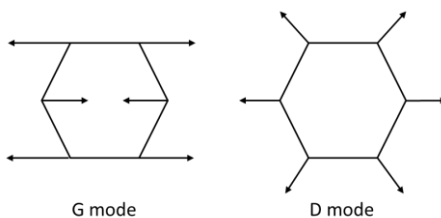


Figure 3.11 G mode (E_{2g}) is the stretching motion of sp^2 carbons and the D mode (A_{1g}) is the breathing motion of aromatic rings

3.3.2 Conductivity, Morphology, and Air Stability

Figure 3.12 and 3.13 display conductivity ($T > \sim 200$ K) and diameters of 17 PA, 9 PANI, 33 CPA, and 15 CPANI two-probe devices. The two-probe conductivity of 15 devices with CPANI (0.03 – 2 S/cm) was found to be somewhat larger than that measured in 33 devices with CPA (0.01 – 0.1 S/cm). If we compare the conductivity of carbonized nanofibers with that of individual pristine nanofibers, we find that CPA displays an order of magnitude lower conductivity than iodine-doped PA nanofibers (0.01 – 100 S/cm), but that the conductivity of CPANI is comparable with that of

HCl doped PANI nanofibers ($0.1 - 1 \text{ S/cm}$)^{16,48}. We obtained diameters analyzing AFM or SEM images. Typical diameters of CPANI ($15 < D < 80 \text{ nm}$) is somewhat smaller than that of PANI ($50 < D < 120 \text{ nm}$) and typical diameters of PA ($10 < D < 80 \text{ nm}$) is comparable to that of CPA ($10 < D < 100 \text{ nm}$). Figure 3.14. displays morphology retaining carbonization of PANI nanofibers by measuring AFM before and after carbonization on the same place. The diameters of fibers decrease after carbonization. Similar reduction of diameter after carbonization has been reported elsewhere⁴⁹. The change of diameters is presumably due to the thermal decomposition of nanofibers in the high temperature heating step⁴⁹.

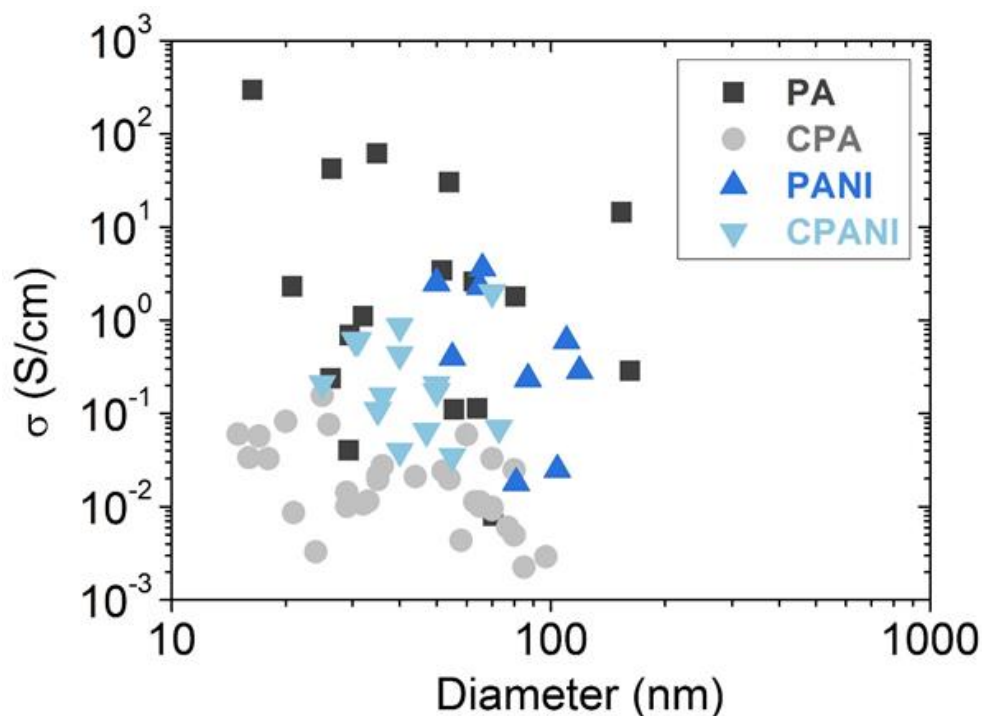


Figure 3.12 Conductivities ($T > 200 \text{ K}$) and diameters of 17 PA, 9 PANI, 33 CPA, and 15 CPANI two-probe devices

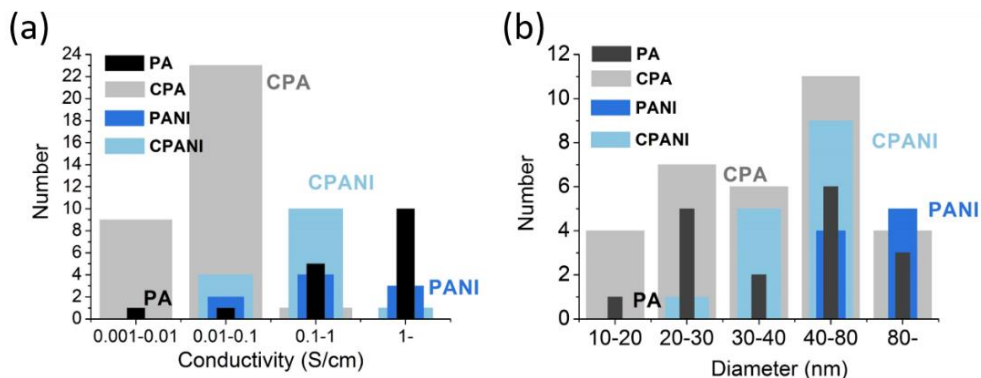


Figure 3.13 Statistics of conductivity (a) and diameter (b) of 17 PA, 9 PANI, 33 CPA, and 15 CPANI devices.

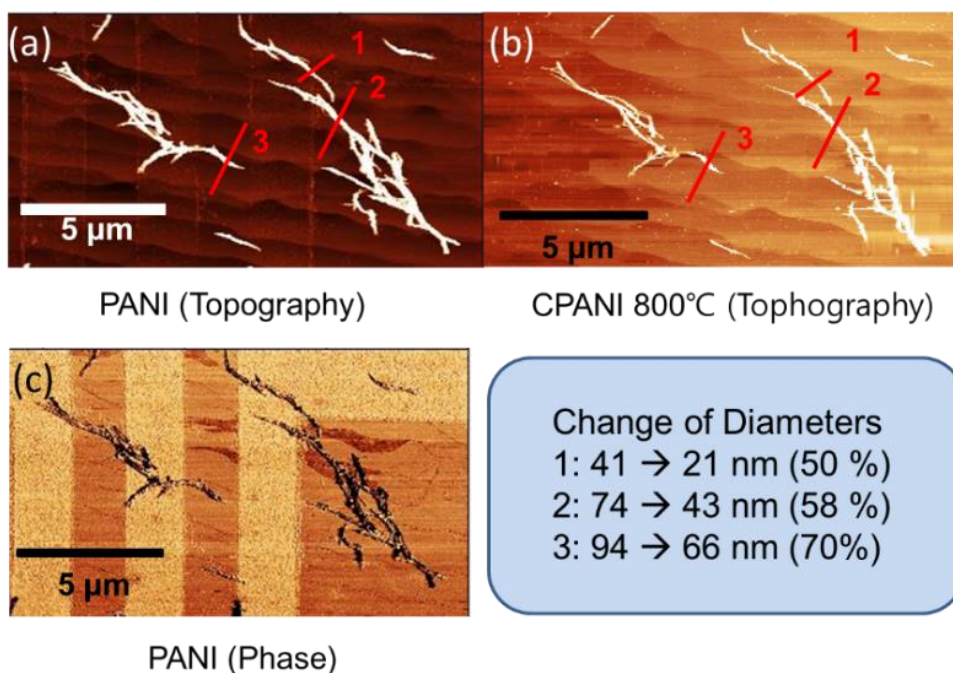


Figure 3.14 Morphology retaining carbonization of PANI nanofibers and change of diameters after carbonization. Comparison between AFM topography of PANI nanofibers on graphene electrodes (a) to AFM topography on the same place after carbonization (b) displays morphology retaining carbonization. Diameters are reduced after carbonization. (c) is the phase picture of PANI on graphene electrodes. In this picture graphene electrode is clearly distinguished from SiC due to the sensitivity of materials in phase information

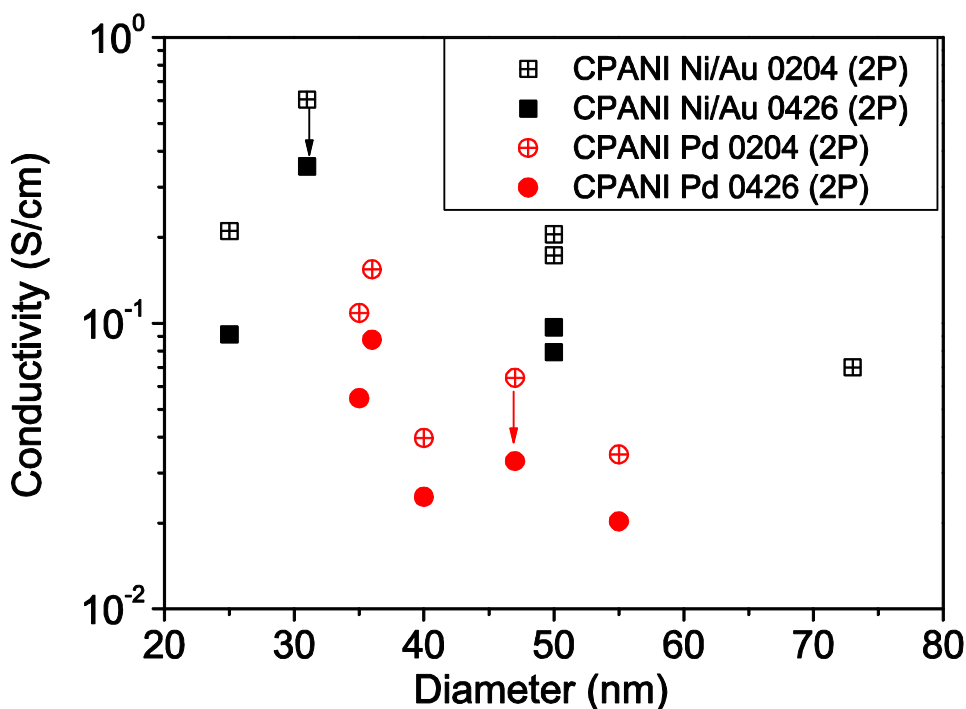


Figure 3.15 Stability of CPANI nanofibers in a simple nitrogen box. The nitrogen box is a simple container with nitrogen flow. About two months later, the room temperature conductivity (two-probe) decreased about factor of two.

Figure 3.15 shows air stability of CPANI nanofibers. The nanofibers are stored in a simple nitrogen box which do not have a load-lock. After about two months later, the conductivity decreased about factor of two. This finding demonstrates that the carbonized fibers need passivation in air.

3.3.3 Measurement Using Graphene Electrodes

Figure 3.16. demonstrates that the graphene electrode is an almost equally good contact material compared to Au electrodes contacting PANI nanofibers. The conductivity of PANI on graphene electrodes is in the same order of magnitude of that in Au electrodes with the same contact area. Figure 3.17(a–c) (individual fibers)

and 3.17(d-f) (bundles of fibers) show AFM pictures and I - V measurements of CPANI nanofiber devices on graphene electrodes. The devices are high temperature (and pyrolysis at 800 °C) compatible. I - V curves are measured on the same device before and after carbonization to evaluate graphene electrodes as a contact material for pristine and carbonized polymers. Generally, resistance increases after carbonization in case of PANI. But rarely, in some contacts such as Fig 3.17(e-f), the resistance decreased after carbonization. These results demonstrate the high temperature compatibility of graphene as a contact material and that the contact is as good as that of Au.

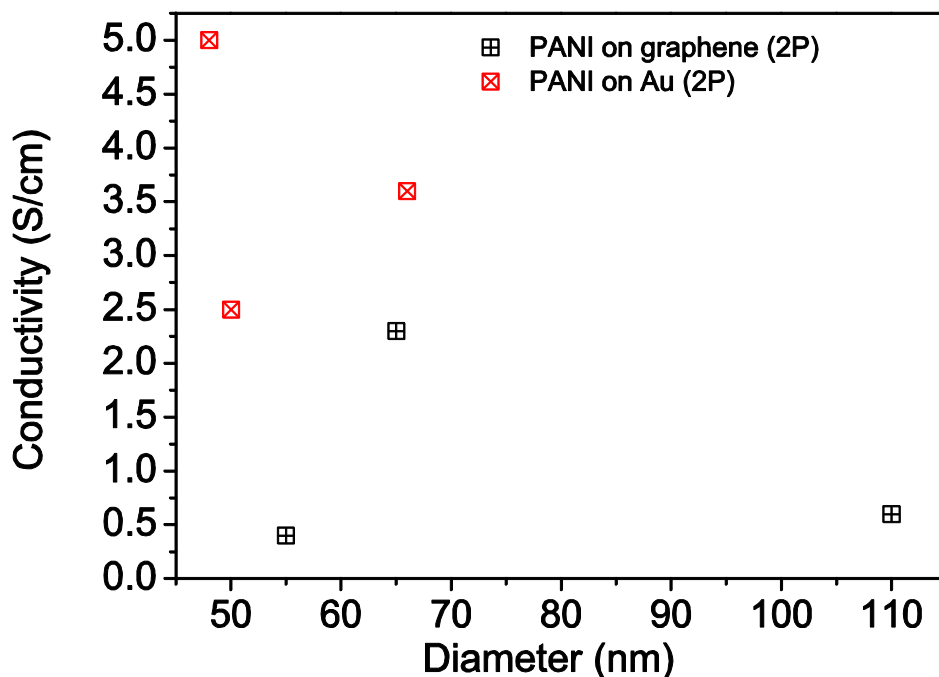


Figure 3.16 Comparison of room temperature two-probe conductivity of PANI nanofibers on graphene and on Au electrodes. The conductivity is in the same order of magnitude. Diameters of the fibers are shown in x-axis.

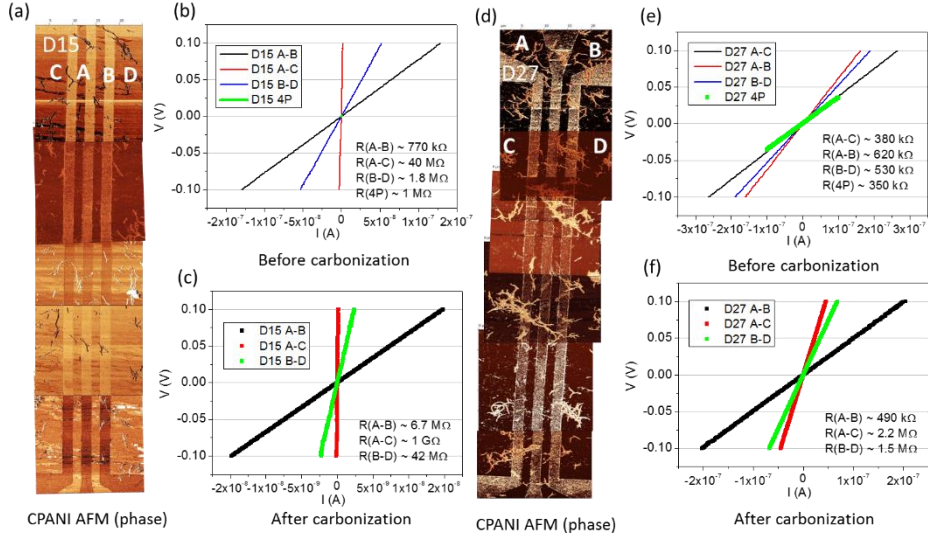


Figure 3.17 AFM phase images of CPANI fibers (a–c, D15) on graphene electrodes and CPANI fiber bundles (d–f, D27). (b,c) I - V curves of D15 before (b) and after (c) carbonization. (e,f) I - V curves of D27 before (e) and after (f) carbonization.

3.3.4 Temperature Dependence of Current-Voltage Characteristics

We discuss I - V characteristics of both CPA (CPA-1, CPA-2, CPA-3) and CPANI (CPANI-1) nanofibers. In this chapter, CPA and CPANI specifically mean CPA-1 and CPANI-1 nanofibers, respectively. Figure 3.18 shows that both CPA and CPANI fibers display qualitatively the same transport properties in the temperature and voltage ranges of this study. The I - V characteristics are highly non-linear at low temperatures and there are transport gaps with threshold voltages of ~ 2.5 V (5×10^4 V/cm) for CPA and ~ 1 V (1×10^4 V/cm) for CPANI nanofibers at 1.5 K. For temperatures below $T < \sim 10$ K, the current voltage characteristic is nearly temperature independent in both CPA and CPANI nanofibers.

Analysis of the non-linear I - V in the two limiting transport regime of the low ($eV/k_B T \ll 1$) and the high bias voltages ($eV/k_B T \gg 1$) reveals that the electron transport in these system is of conventional VRH^{50,51}. Figure 3.19 shows that the conductance, $G = I/V$ in both the low bias Ohmic regime and the high bias non-linear regime follows the characteristic T and V dependence of Efros-Shklovskii VRH (ES-VRH)⁵², respectively. At low bias and $T < 180$ K, the I - V of both CPA and CPANI is Ohmic and well described by $G \propto \exp[-\left(\frac{T_0}{T}\right)^{\frac{1}{2}}]$ [Fig. 3.19(a)], where $T_0 = 2.8e^2/4\pi k_B \epsilon \epsilon_0 r$ is the characteristic temperature with $T_0 = 7500$ K for CPA and $T_0 = 2900$ K for CPANI fibers. Here, ϵ_0 is the permittivity of vacuum, ϵ is the dielectric constant, k_B is the Boltzmann constant, e is the electron charge, and r is the average hopping distance. This temperature dependence is attributed to the ES-VRH, in which the soft Coulomb gap is formed due to the long-range Coulomb interaction of the electron-hole pair created during charge carrier hopping⁵². At $T > 180$ K, deviation from the ES-VRH law is prominent in both fibers. We ascribe the deviation at high temperatures to the contribution of short-range Coulomb interactions which is excluded in the ES-VRH and dominant at high energies. Screening of long range interactions at high temperatures and crossover to a distinct temperature relation due to the contribution of the short-range interaction to the gap have been raised recently⁵³. Moreover, at high bias voltages ($V > \sim 1$ V) and low temperatures ($T < 20$ K), the conductance of both CPA and CPANI is almost temperature independent and follows $G \propto \exp[-\left(\frac{E_0}{E}\right)^{\frac{1}{2}}]$ [Fig 3.19(b)], where E is the electric field and $E_0 = k_B T_0 / 2e\xi$ is the characteristic electric field with $E_0 = 1.2 \times 10^7$ V/cm ($E_0 = 2.5 \times 10^6$ V/cm) for the CPA (CPANI) nanofiber. This inverse square root voltage dependence is expected for the ES-VRH in the limit, $eE\xi \gg k_B T$ and $\xi = 0.3$ nm (0.5 nm) for CPA (CPANI) was obtained by combining T_0 and E_0 , which is consistent with the analysis of Raman spectroscopy⁵⁴⁻⁵⁶.

Figure 3.20 displays temperature dependence of conductance ($G(T)$) at various fixed source-drain voltages, and voltage dependence of conductance ($G(V)$) at various fixed temperatures in the CPA nanofiber. At low voltages, conductance follows power law $G = T^\alpha$ and the temperature dependence weakens as voltage increases. At very high voltages, the conductance is almost temperature independent [Fig. 3.20(a)]. If we fix temperature [Fig. 3.20(b)], the low temperature ($T < 30$ K) conductance is fitted by $G(V) = G_0 \exp[-(V_0/V)]^{1/2}$ and at higher temperatures and modest voltages ($T > 30$ K, $eEr > k_B T$) by $G(V, T) = G_0 \exp(L_c eV/Lk_B T)$, where L_c is the characteristic length which is proportional to the hopping length, and L is the sample length between source and drain electrodes. The value of L_c and L is 2 nm and 500 nm, respectively for the CPA of Fig. 3.20. This dependence is the characteristic of VRH at moderate electric field⁵⁷⁻⁵⁹.

Similar behaviors have been observed in CPANI nanofibers. Figure 3.21 displays the same behavior in CPANI nanofiber. The high electric field ($eE\xi \gg k_B T$) conductance is of the ES-VRH (Fig. 3.21(b)). As the ratio of electric energy to the thermal energy lowers, the conductance is both temperature and electric field dependent. The initial functional dependence $G(V, T) = G_0 \exp(CL_c eV/Lk_B T)$ is attributed to the non-Ohmic VRH conduction in modest electric field. The value of L_c and L is 2 nm and 1000 nm, respectively for the CPANI of Fig. 3.21.

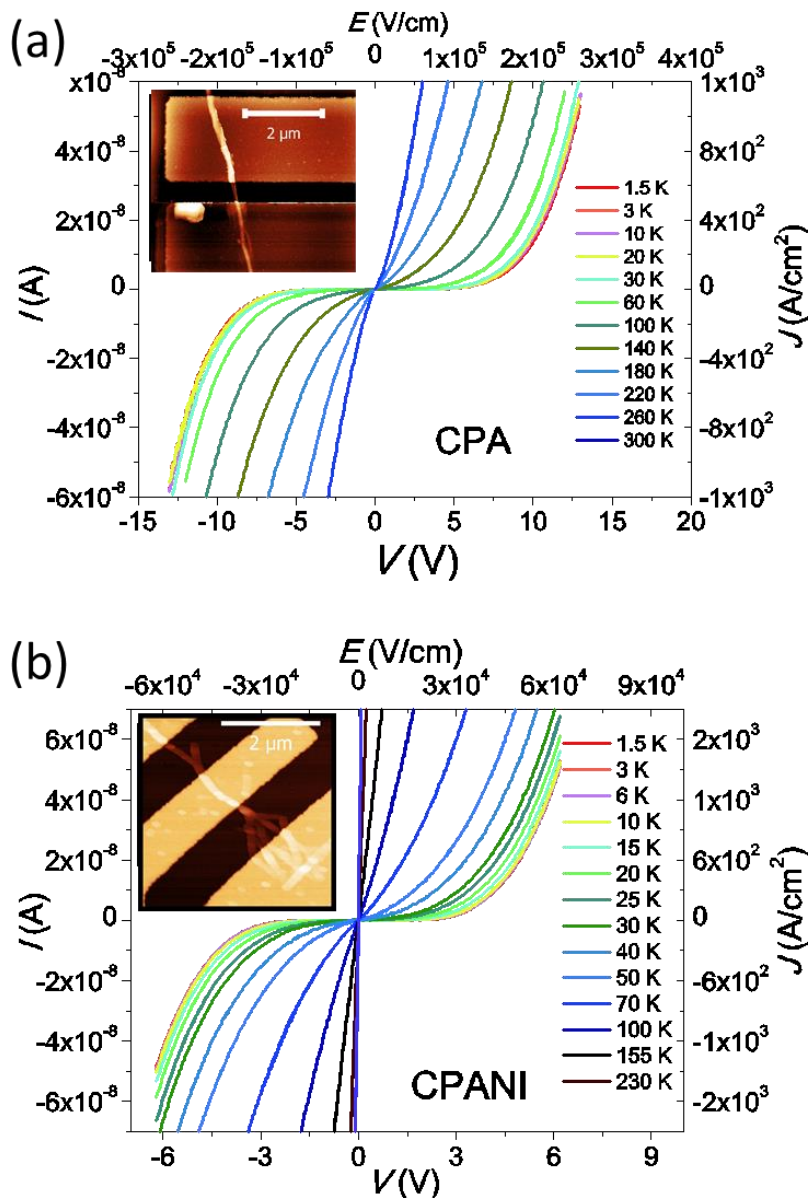


Figure 3.18 I - V (E - J) characteristics of CPA (CPA-1) (a) and CPANI (CPANI-1) (b) nanofibers. Inset images are SEM pictures of CPA-1 (a) and CPANI-1 (b) nanofibers with Ti/Au top contact. Distances between contacts are 500 nm and 1 μ m, respectively for CPA and CPANI nanofibers. Room temperature resistance and conductivity are 40 M Ω , 0.03 S/cm for the CPA and 1 M Ω and 2 S/cm for the CPANI nanofiber. Diameter of the CPA-1 nanofiber is \sim 70 nm and the CPANI-1 nanofiber consists of 5 small parallel nanofibers which have diameters of 10 \sim 15 nm.

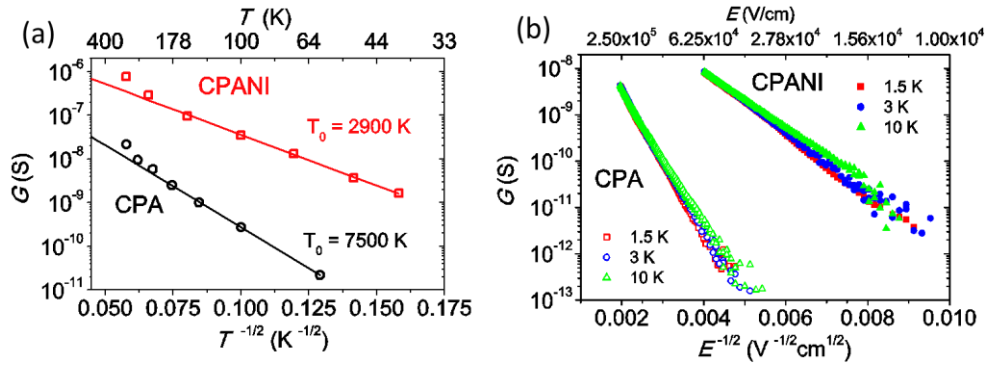


Figure 3.19 (a) The temperature dependence of the Ohmic conductance at low bias voltages follows the ES-VRH, $G(T) \propto \exp[-(T_0/T)]^{1/2}$ at $T < 180$ K and deviates from the ES-VRH at $T > 180$ K. (b) The bias electric field dependence of the non-Ohmic conductance at low temperatures ($T < \sim 10$ K) and high voltages ($V > \sim 1$ V) shows the characteristic of the ES-VRH, $G(E) \propto \exp[-(E_0/E)]^{1/2}$.

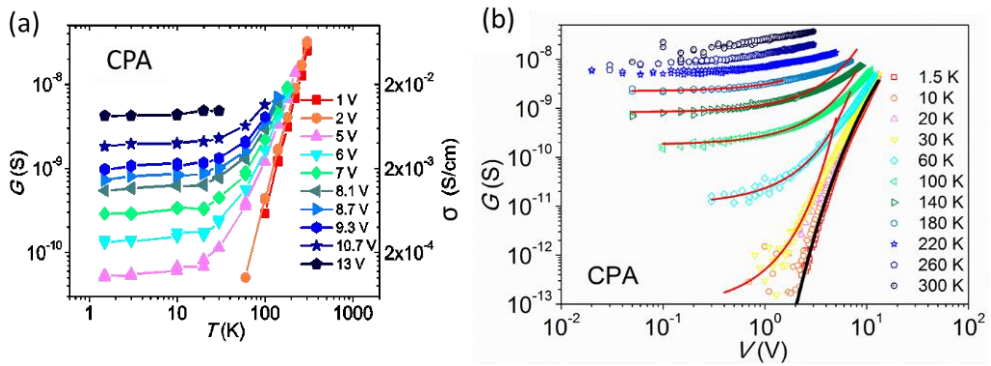


Figure 3.20 (a) Temperature dependence of conductance at various fixed source-drain voltages in the CPA nanofiber. At low voltages, conductance follows power law and at high voltages the conductance becomes almost temperature independent. (b) Voltage dependence of conductance at various fixed temperatures in the CPA nanofiber. Red and black lines are the fitting curves $G(V, T) = G_0 \exp(L_c eV / Lk_B T)$ and $G(V) = G_0 \exp[-(V_0/V)]^{1/2}$, respectively.

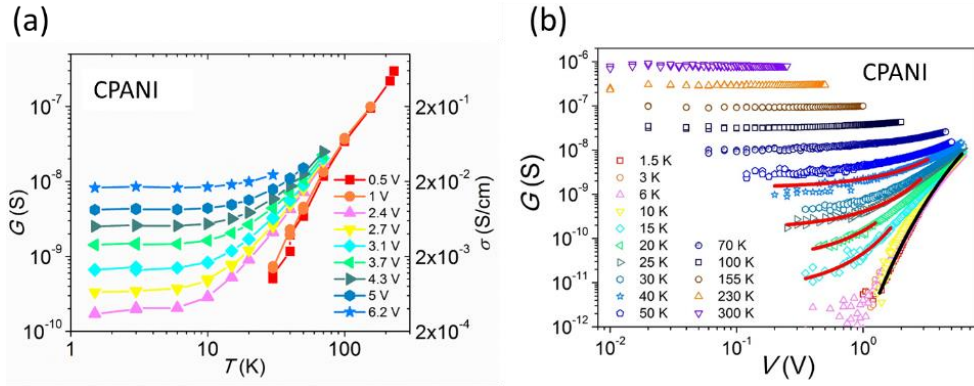


Figure 3.21 (a) Temperature dependence of conductance at various fixed source-drain voltages in the CPANI nanofiber. At low voltages, conductance follows power law and at high voltages the conductance becomes almost temperature independent. (b) Voltage dependence of conductance at various fixed temperatures in the CPANI nanofiber. Red and black lines are the fitting curves $G(V, T) = G_0 \exp(CeV/k_B T)$ and $G(V) = G_0 \exp[-(V_0/V)]^{1/2}$, respectively.

3.3.5 Universal Scaling of Carbonized Polymer Nanofibers

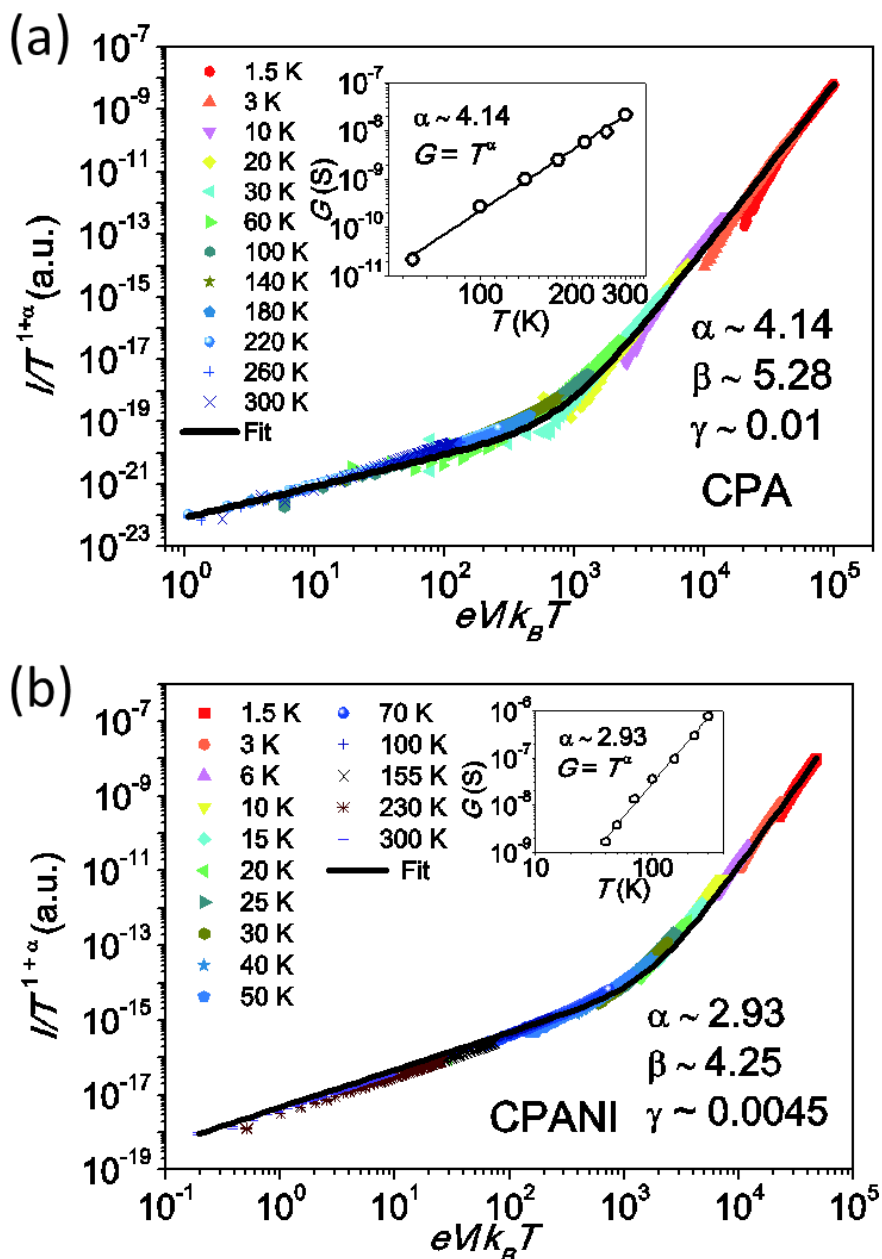


Figure 3.22 Universal scaling of CPA and CPANI nanofibers. $I/T^{\alpha+1}$ vs $eV/k_B T$ plot of both CPA (a) and CPANI (b) nanofibers. Inset shows power law dependence of Ohmic conductance, $G(T) \propto T^\alpha$ in both CPA (a) and CPANI (b) nanofibers. Fit to Eq. 1 (black curves) gives fitting parameters I_0 , β , and γ .

With the ES-VRH behavior in the limited range of T and V discussed in chapter 3.3.4, Eq. 2.1 gives the opportunity to describe the data in the entire range of parameters of our study. Remarkably, it is hard to distinguish between the stretched exponential temperature dependence, $G(T) \propto \exp[-(T_0/T)]^{1/2}$ and the power law temperature dependence, $G(T) \propto T^\alpha$ in low bias Ohmic regime due to the limited range of temperature. If we plot the Ohmic conductance in log-log scale, the Ohmic conductance mimics power law behavior $G(T) \propto T^\alpha$ with $\alpha = 4.14$ for CPA and $\alpha = 2.93$ for CPANI nanofibers (Inset of Fig. 3.22). Similar is the non-Ohmic $I-V$ at low temperatures as shown in Fig. 3.23. This means that the apparent power law $G(T) \propto T^\alpha$ (Inset of Fig. 3.22) and $I(V) \propto V^\beta$ (Fig. 3.22, 3.23) in certain parameter ranges might arise from the ES-VRH. Using the power law exponent α , we plotted all $I-V$ curves for all temperatures as $I/T^{\alpha+1}$ vs $eV/k_B T$ according to Eq. 2.1 and found that all $I-V$ curves collapse into a single curve for both CPA and CPANI (Fig. 3.22). The fitting parameters using Eq. 2.1 are $\gamma^{-1} = 100$ for CPA and $\gamma^{-1} = 205$ for CPANI nanofibers. Remarkably, these values are comparable (same order of magnitude) with number of tunneling barriers (γ^{-1}) obtained in pristine PA and PANI polymer nanofibers¹⁶ (summarized in Table 3.1).

Having in mind the considerable disorder and the ES-VRH behavior of carbonized polymer fibers, we interpreted the apparent power law scaling in carbonized polymer fibers within the framework of VRH⁶⁰⁻⁶². We considered the 1D-VRH model developed by Rodin and Fogler⁶⁰, the electric field compensated VRH model proposed by Li *et al.*⁶¹, and the implementation of effective temperature concept in VRH proposed by Abdalla *et al.*⁶² as possibilities. Since carbonized polymers have undergone cross-linking of polymer chains, the explanation of Li *et al.* and that of Abdalla *et al.* which do not necessarily include one-dimensional systems are more appropriate to explain our data. Li *et al.* have explained the physical origin of the power law scaling by invoking electric field compensation for thermal activation in VRH in wide range of T and V parameters. Abdalla *et al.*

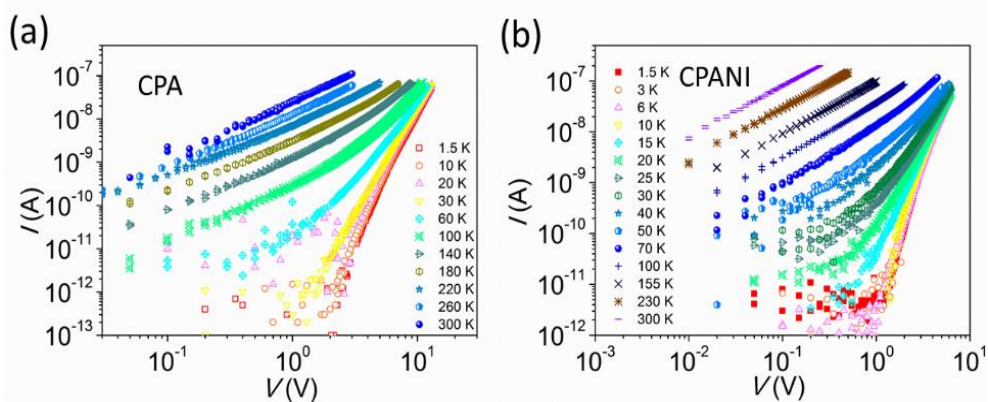


Figure 3.23 I - V curves of CPA (a) and CPANI nanofibers (b) plotted in log-log scale to check the strictness of power law behavior of I - V . As the $G(V)$ follows the ES-VRH, the I - V slightly downturn at low temperatures.

showed that the scaling of Eq. 2.1 is phenomenologically equivalent to the scaling function of the effective temperature, $G \propto T_{\text{eff}}^\alpha$. Physically, the effective temperature concept combines the effects of the high electric field and the lattice temperature, which is reminiscent of the model of Li *et al.*. Importantly, Abdalla *et al.* reproduced the same scaling by numerical simulation incorporating Coulomb interactions in the Miller-Abrahams expression of hopping rates. In the same fashion, we propose that the power law scaling in carbonized polymer fibers is originated from the ES-VRH between local sp^2 carbon sites in the networks of quasi-amorphous carbon bonds.

3.3.6 CPA Cross-junction

A cross-junction of the two different CPA nanofibers is formed accidentally during dispersion on the substrate as in Fig. 3.24. Figure 3.24 is the SEM image of the CPA-2 (A-B) and the CPA-3 nanofibers (C-D). Electrodes (A, B, C, D) of Ti/Au (5/95 nm) were contacted on top of the nanofibers and distance between electrodes are 500 nm, 1.84 μm for A-B and C-D, respectively. Diameter of the CPA-2 (CPA-3) nanofiber is 60 nm (25 nm) and a cross-junction between the CPA-2 and the CPA-3 nanofibers

is formed between electrode B-C and B-D. Electrodes B-C is measured to characterize the cross-junction between the CPA-2 and the CPA-3 nanofibers. The cross-junction of the CPA-2 and the CPA-3 consists of the 510 nm length of the CPA-2 nanofiber with diameter 25 nm and the 870 nm length of the CPA-3 nanofiber with diameter 25 nm. Room temperature resistance of the junction between the two nanofibers was 210 M Ω .

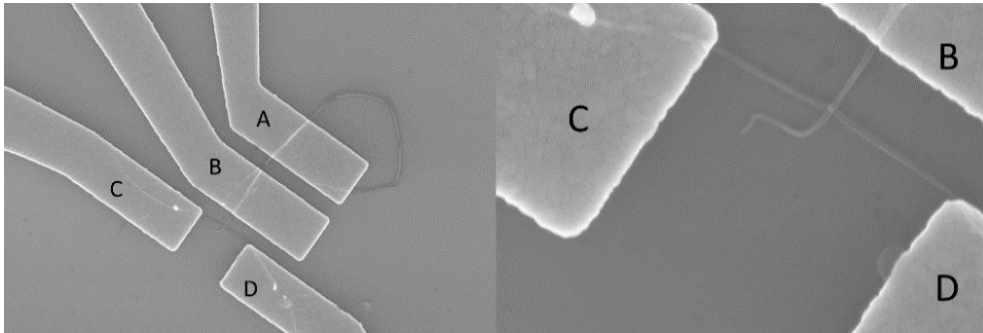


Figure 3.24 SEM images of CPA cross junction devices: the CPA-2 (A-B) and the CPA-3 nanofibers (C-D). Electrodes (A, B, C, D) of Ti/Au (5/95 nm) were contacted on top of the nanofibers and distance between electrodes are 500 nm, 1.84 μ m for A-B and C-D, respectively.

Figure 3.25(a) shows the temperature dependence of I - V characteristics of the contact (A-B). It shows similar behaviors as that of the CPA-1 nanofiber such as non-linearity, transport gap and weak temperature dependence at low temperatures. Other similar behaviors observed in the CPA-1 (For the image of CPA-1, see AFM of Fig. 3.18) nanofiber are also observed in the CPA-2 (A-B) nanofiber such as power law behavior of conductance at low bias and its deviation at high bias voltages [Fig. 3.25(b)], quasi power law behavior of I - V [Fig. 3.25(c)] and the scaling behavior of I - V curves [Fig. 3.25(d)]. Room temperature resistance and conductivity of the CPA-2 nanofiber was 30 M Ω and 0.04 S/cm, similar with those of the CPA-1 nanofiber (40 M Ω , 0.03 S/cm). The CPA-2 nanofiber (A-B) also shows the characteristic of the ES-VRH and the power law dependences (Fig. 3.26).

Figure 3.27(a) shows temperature dependence of I - V characteristics for the CPA-

3 (contact C-D) nanofiber. For CPA-3 nanofiber, the inter-electrode length was relatively long and room temperature resistance was relatively high (240 M Ω , 0.16 S/cm). However, it shows similar behaviors as those of the CPA-1 and the CPA-2 nanofibers such as non-linearity, transport gap and weak temperature dependence at low temperatures. Moreover, other behaviors observed in CPA-1 and CPA-2 nanofibers such as power law behavior of conductance at low bias and weaker temperature dependence at high voltages [Fig. 3.27(b)], quasi power law behavior of I - V [Fig. 3.27(c)] and the scaling behavior of I - V curves [Fig. 3.27(d)] are also observed in the CPA-3 nanofiber. It also shows the characteristic of the ES-VRH at low temperatures (Fig. 3.28).

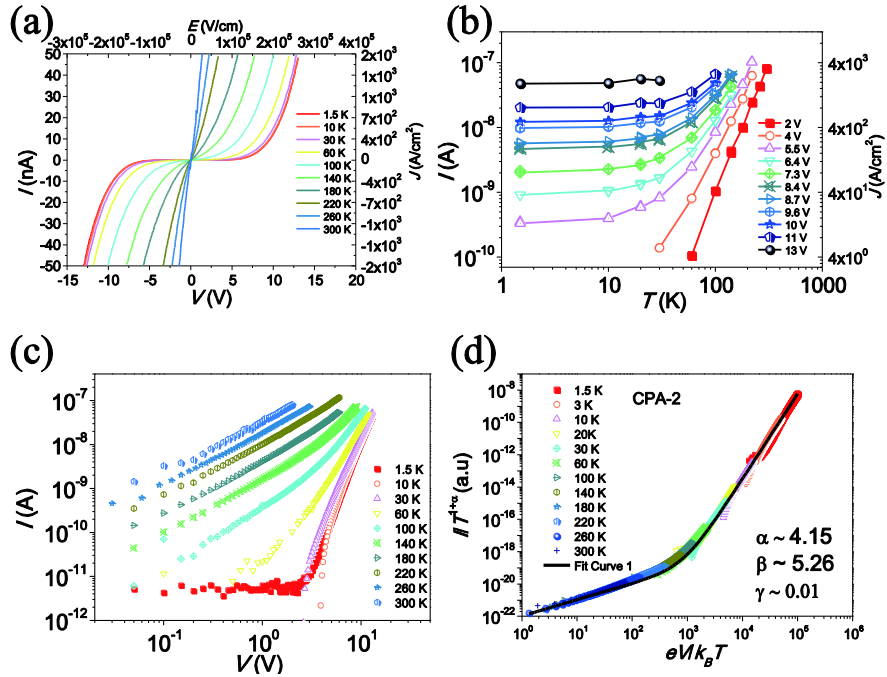


Figure 3.25 (a) Temperature dependence of I - V characteristics for the CPA-2 nanofiber in linear scale. (b) Temperature dependence of current at various source-drain applied voltages. As voltage increases temperature dependence weakens and deviates from power law dependence at low voltages. (c) Temperature dependence of I - V characteristics plotted in double logarithmic scale shows quasi power law behavior. (d) I - V curves from different temperatures collapsed in a single universal curve. α is the exponent of the temperature dependence of conductivity, $G(T) \propto T^\alpha$ and β is obtained from the fitting.

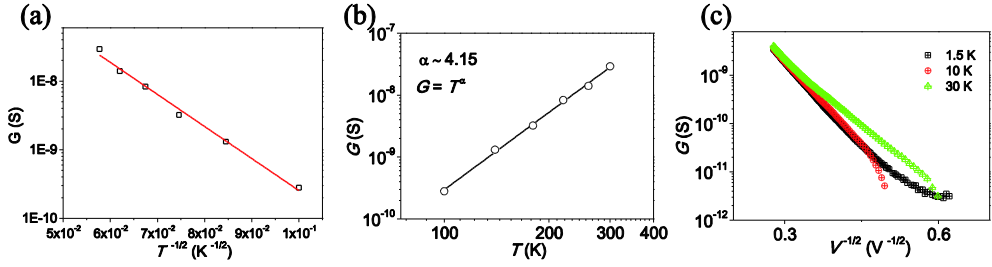


Figure 3.26 The temperature dependence of the Ohmic conductance of the CPA-2 at low bias voltages are plotted as, $G(T) \propto \exp[-(T_0/T)^{\frac{1}{2}}]$ (a) and power law (b). The characteristic temperature was calculated as $T_0 = 11500$ K. (c) The bias voltage dependence of the non-Ohmic conductance at low temperatures ($T < 30$ K) and high voltages ($V > \sim 1$ V) shows the characteristic of ES-VRH, $G(V) \propto \exp[-(V_0/V)^{\frac{1}{2}}]$ in the CPA-2.

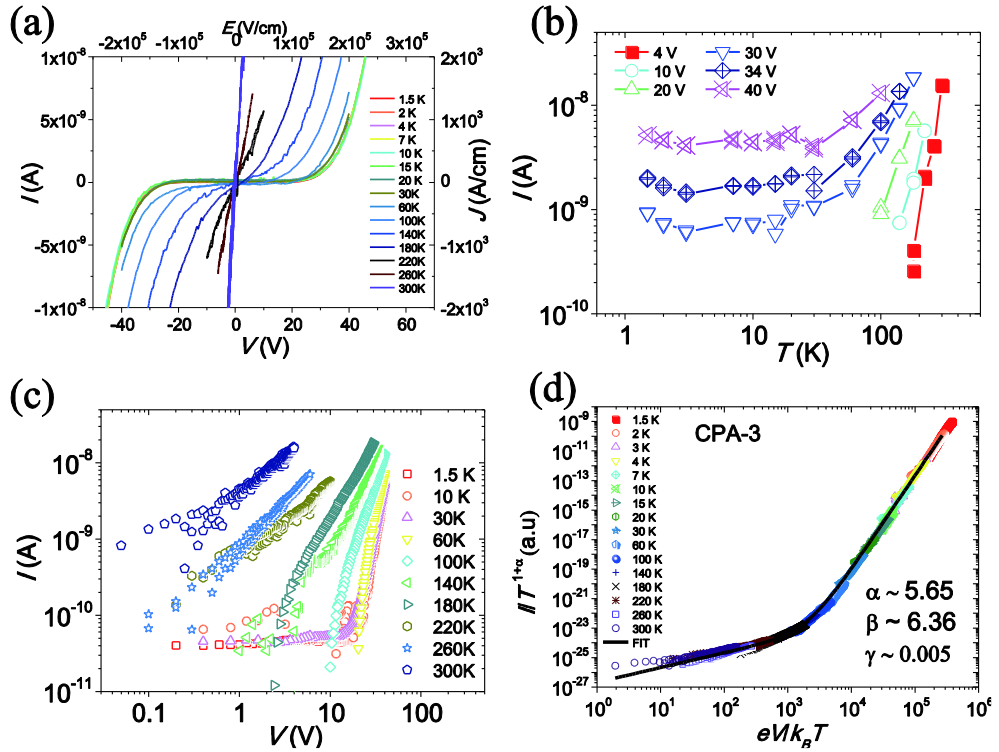


Figure 3.27 (a) Temperature dependence of I - V characteristics for CPA-3 nanofiber in linear scale. (b) Temperature dependence of current at various source-drain applied voltages. As voltage increases temperature dependence weakens and deviates from power law dependence at low voltages. (c) Temperature dependence of I - V characteristics plotted in double logarithmic scale shows quasi power law behavior. (d) I - V curves from different temperatures collapsed in a single universal curve. α is the exponent of the temperature dependence of conductivity, $G(T) \propto T^\alpha$ and β from the fitting.

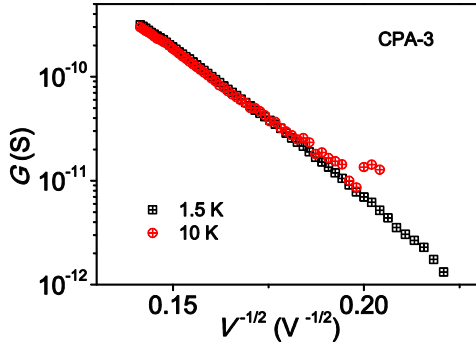


Figure 3.28 The bias voltage dependence of the non-Ohmic conductance at low temperatures ($T < 10$ K) and high voltages ($V > \sim 20$ V) shows the characteristic of ES-VRH, $G(V) \propto \exp[-(V_0/V)^2]$ in the CPA-3 nanofiber.

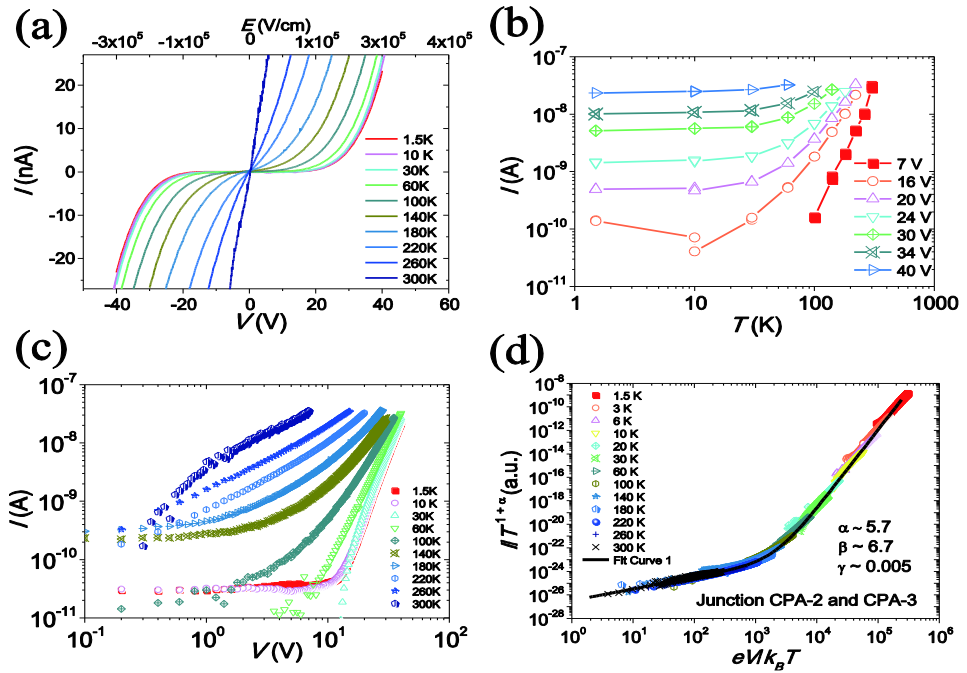


Figure 3.29 (a) Temperature dependence of I - V characteristics in linear scale for the cross-junction between the CPA-2 and the CPA-3 nanofibers. (b) Temperature dependence of current at various source-drain applied voltages. As voltage increases temperature dependence weakens and deviates from power law dependence at low voltages. (c) Temperature dependence of I - V characteristics plotted in double logarithmic scale shows quasi power law behavior. (d) I - V curves from different temperatures collapsed in a single universal curve. α is the exponent of the temperature dependence of conductivity, $G(T) \propto T^\alpha$ and β is obtained from the fitting.

Figure 3.29(a) shows temperature dependence of I - V characteristics for the cross-junction between the CPA-2 and the CPA-3 nanofibers (B-C in Fig. 3.24) measured in the two-probe geometry. Interestingly, it shows similar behaviors as those of CPA nanofibers without a junction: non-linearity, transport gap and weak temperature dependence at low temperatures. Other similar behaviors such as power law behavior of conductance at low bias and deviation from power law at high bias voltages [Fig. 3.29(b)], quasi power law behavior of I - V [Fig. 3.29(c)] and the scaling behavior of I - V curves [Fig. 3.29(d)] are also observed. It is interesting that the same scaling behavior is observed in a cross-junction of CPA nanofibers, which indicates that electrical transport through the cross-junction is not dominating the overall transport between the two electrodes. This finding also supports the hopping conduction in carbonized polymers, and refutes the LL transport.

3.3.7 Threshold Voltage and Contact Resistance

The threshold voltage at low temperatures [Fig. 3.18(a,b)] might arise from Coulomb blockade (CB) effects. When the system consists of metallic islands with small enough size and insulating surroundings, the charging energy $e^2/2C$, where C is the capacitance of the islands exceeds thermal energy $k_B T$, thereby the electron transport to the metallic island is blocked by Coulomb charging energy. The characteristic of CB in this temperature regime is the existence of threshold voltage which is mentioned in Chapter 3.3.4 briefly. Figure 3.30 and 3.31 show I^*dV/dI vs V in various CPA and CPANI nanofibers, respectively to clarify the value of the threshold voltage. The threshold voltage is independent of temperature below a certain temperature and decrease gradually as the temperature increases. The theory of CB transport in metallic dot arrays by Middleton and Wingreen predicts a current

dependence, $I \propto (V - V_t)^\zeta$ with $\zeta \sim 1$ in 1D, and $\zeta \sim 2$ or $5/3$ in 2D⁶³. However, the exponent ζ is usually larger than the theoretical value due to the topological inhomogeneity⁶⁴ as we observed $2.4 < \zeta < 4.1$ (Fig. 3.32). We considered the self-capacitance $C_0 = 4\pi\epsilon\epsilon_0 r$ of a crystalline island of radius r and the mutual capacitance $C_i = 2\pi\epsilon\epsilon_0 r \ln \left[\frac{r+d}{d} \right]$, where $2d$ is the spacing between crystalline islands. The radius $r = 0.5$ nm is used from localization lengths and the Raman spectroscopy analysis and $2d+2r = \gamma L$ gives $d = 2$ nm for both CPA and CPANI. Then, the charging energy $E_C \approx e^2/2(C_0 + 9C_i)$ is about 350 K, with dielectric constant $\epsilon \sim 20$ ⁶⁴⁻⁶⁶, which means that the threshold voltage should exist even at room temperature, which contradicts to our data. The threshold voltage exists below $T < 100$ K ($T < 30$ K) for CPA (CPANI) nanofibers. The sp^2 aromatic rings exist as confirmed by appearance of G and D bands (Fig. 3.9). But the broadness of Raman bands suggests that the aromatic rings do not form well-defined crystalline islands yet but randomly distributed in the sample. This point is different from other reported CB systems^{64,65} where well-defined crystalline islands exist for Coulomb blockade transport. Therefore, instead of CB, we ascribe the threshold voltage to the crossover from activation-less hopping to phonon emission hopping. At low temperature and low electric field, it is simply not able to flow current. At low temperature, the electric current is driven solely by the electric field with emission of phonons due to the lack of thermal activation.

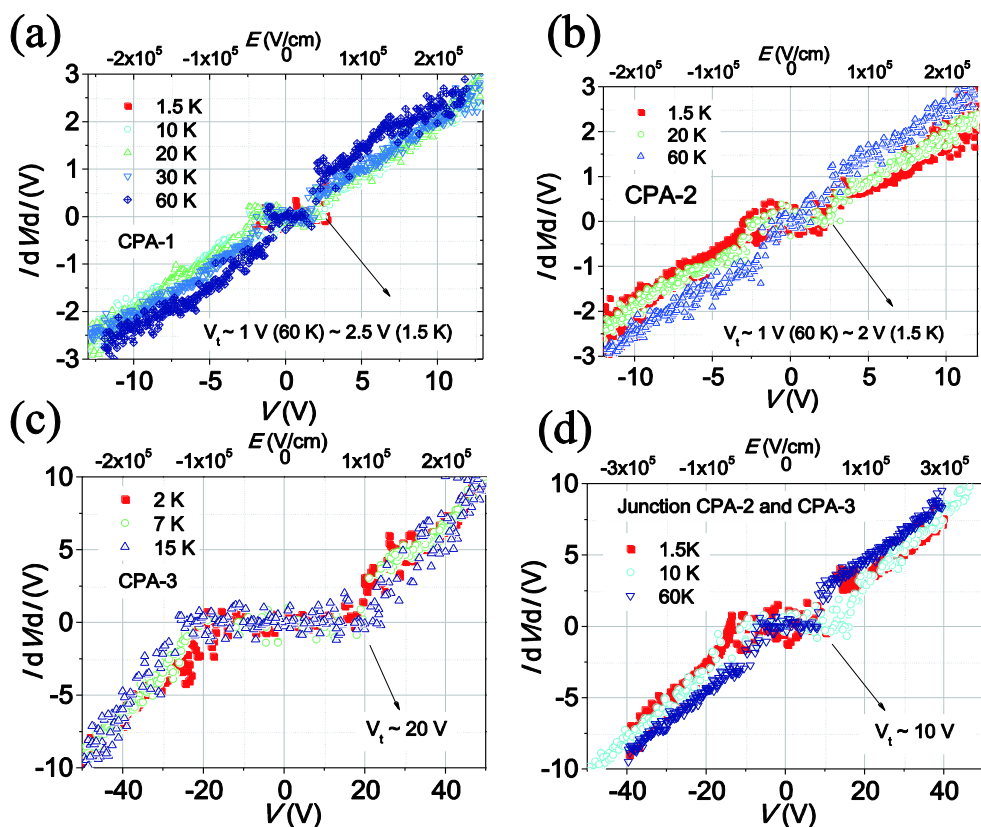


Figure 3.30 I^*dV/dI vs V plot of the CPA-1 (a), CPA-2 (b), CPA-3 (c), and the cross-junction between the CPA-2 and the CPA-3 nanofibers (d) and evaluated threshold voltages.

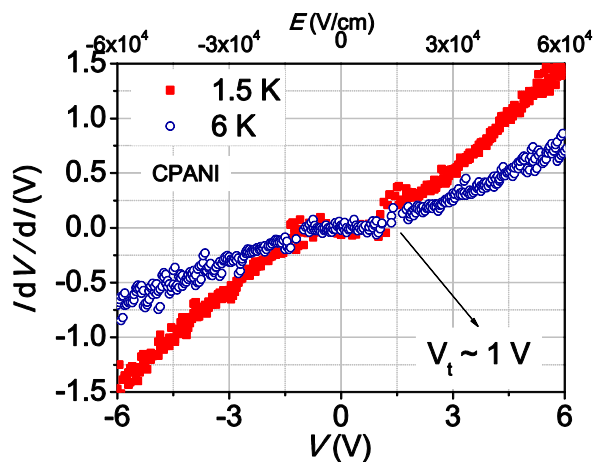


Figure 3.31 I^*dV/dI vs V plot of the CPANI nanofiber (CPANI-1) at 1.5 K and 6 K. Threshold voltage is around 1 V.

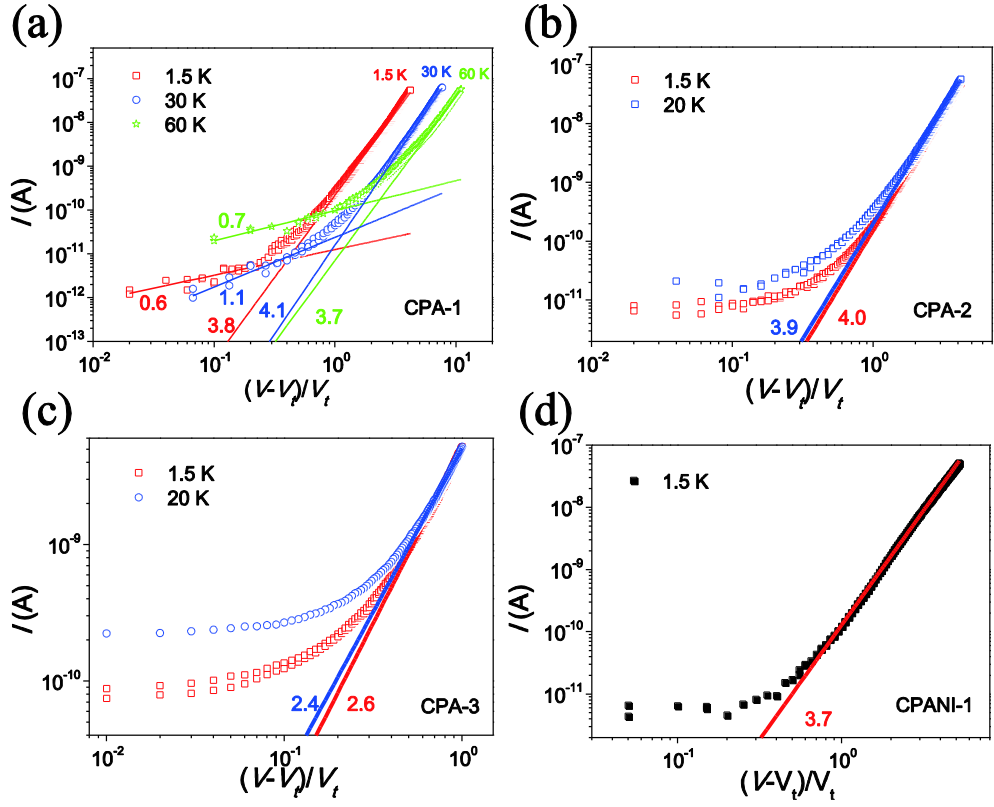


Figure 3.32 Current vs $(V-V_t)/V_t$ plot in double logarithmic scale for (a) CPA-1, (b) CPA-2, (c) CPA-3, and (d) CPANI-1 nanofiber. Slopes determining ζ in $I \propto \left[\frac{V-V_t}{V_t}\right]^\zeta$ are shown in each Figure.

Poor interfaces or work function mismatch might lead to high contact resistances and Schottky barriers which display themselves temperature-dependent non-linear I - V characteristic. At low temperatures, four-probe measurements are deliberately avoided due to high resistances of carbonized polymer nanofibers. Meanwhile, at room temperature, we have measured and compared two-probe (R_{2P}) and four-probe (R_{4P}) resistances using different metal contacts (Ti/Au, Ni, Pd). The contact resistance obtained as $R_c = R_{2p} - R_{4p}$ is usually small relative to the high sample resistance regardless of the metal used for contact. Therefore, contributions from the contact is not significant compared to the sample resistance. This relatively small contact resistance is presumably due to the fact that we contact wide metal electrodes

with 2 μm width on top of fibers using evaporation and the sample resistance is significantly high enough. Also the symmetric I - V at all temperatures is hardly originated from Schottky barriers. If the tunneling through Schottky barriers is dominant, the I - V is asymmetric as the two Schottky barriers at the source and drain electrodes cannot be the same. Therefore, we conclude that the non-linear I - V is not originated from Schottky barrier.

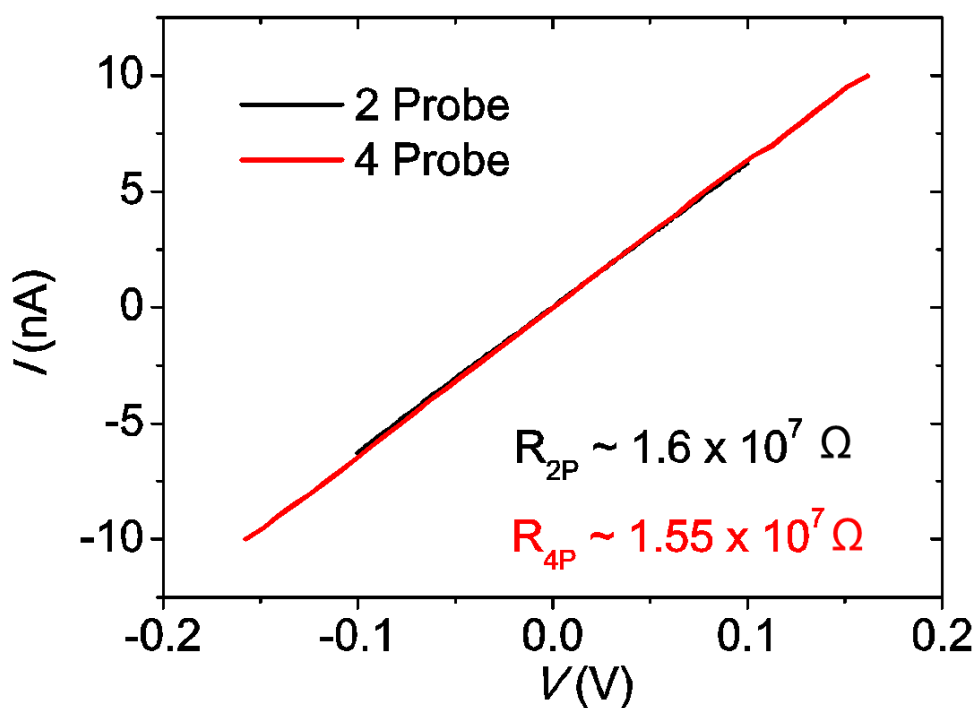


Figure. 3.33 Two-probe and four-probe measurements of a typical carbonized polymer nanofiber at room temperature. The contact resistance is small compared to the high sample resistance.

3.3.8 Magneto Conductance

Figure 3.34 is the magneto-conductance (MC) of the CPA nanofiber at 1.5 K at various voltages. The MC is the conductance difference due to the applied magnetic field divided by current at zero magnetic field. At fixed voltages, it is the current difference divided by zero field current ($MC = \Delta I / I = \{I(H) - I(0)\} / I(0)$). The MC of CPA is negative at $1.5 < T < 20$ K, which means that the conductance decreases in magnetic field. Interestingly, the magnitude of MC decreases as the source-drain electric field increases. Regardless of polymer kinds, MC behaviors are similar in both CPA and CPANI nanofibers. The qualitative similarities in magneto transport of both carbonized single polymer fibers, CPA and CPANI, most likely arises from the similarity in their structures after carbonization. In VRH conduction, both the spin alignment^{67,68} and the wave function shrinkage effect⁵⁰ have been considered for the decrease of conductance. The alignment effect influences the VRH transport because only electrons with spin singlet can occupy one localized state. Therefore, four possibilities of hopping: from singly occupied (SO) to SO, SO to unoccupied (UO), doubly occupied (DO) to SO, and DO to UO states can take place. Magnetic field suppresses hopping from SO to SO and consequently DO to UO due to the spin alignment^{67,68}. Moreover, the electron wave function shrinks in the direction perpendicular to the magnetic field in the presence of magnetic field (chapter 2.3). These two effects have been used to explain the negative and quadratic increase of MC at low magnetic field, which supports the initial quadratic behavior of MC in Fig. 3.34 and 3.35. However, the spin alignment model predicts saturation of MC at high magnetic field when all spins are aligned, contradicts to the data. Therefore, we ascribe the negative MC mainly to the effect of wave function shrinkage

On the electric field dependence of MC, Similar behavior of MC with increasing bias voltages has also been observed in InSb nanowires⁶⁹, polymer nanofibers^{11,16}, and network of PANI nanofibers⁷⁰. Depending on materials, the same behavior has

been explained in different origins: breaking of spin-charge separation in LL by magnetic field for InAs nanowire, and increasing number of spin-less carriers at high electric field for polymer nanofibers. It is obvious that none of these are applicable to carbonized polymer nanofibers because carbonized polymer nanofibers follow VRH. The VRH takes place in PANI nanofiber networks where the authors proposed that decrease of activation energy at high electric field is the origin of the electric field dependence⁷⁰. As discussed in chapter 2.2, electric field reduces potential energy barrier by the amount of $eE(r_j - r_i)$. In sufficiently high electric field ($E \gg 2k_B T / \epsilon \xi$), thermal activation energy is canceled out and the hopping distance becomes $r = r_j - r_i = \xi \sqrt{E_0 / E}$, which is electric field dependent. Qualitatively, the magnitude of MC is proportional to the hopping length because the diamagnetic potential energy is not only proportional to the magnetic field but also to the distance from the center of the wave function. We propose that the electric field dependence of hopping length explains the electric field dependence of MC observed in carbonized polymer nanofibers. At low electric field, the hopping length $r = r_j - r_i = \xi \sqrt{T_0 / T}$ is inversely proportional to the temperature. The electric field and temperature dependence of hopping length gives the electric field and temperature dependence of MC in carbonized polymer nanofibers.

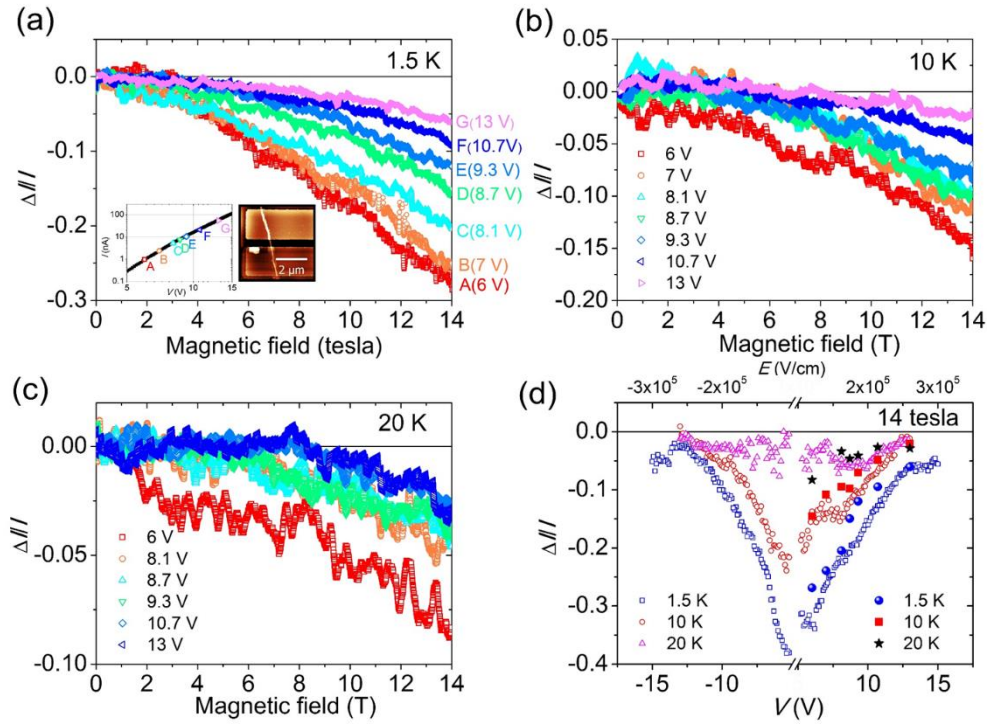


Figure 3.34 MC at fixed source-drain voltages of the CPA nanofiber for (a) at 1.5 K, (b) 10 K, and (c) 20 K. A – G refers to each excitation voltage at 1.5 K. (A: ~ 950 pA, 6 V; B: ~ 2.3 nA, 7 V; C: ~ 5.1 nA, 8.1 V; D: ~ 7.4 nA, 8.7 V; E: ~ 10 nA, 9.3 V; F: ~ 20 nA, 10.7 V; G: ~ 54 nA, 13 V). Inset is double logarithmic plot of I - V at 1.5 K and the AFM picture of the CPA nanofiber device. (d) MC at 14-tesla as a function of voltages at various temperatures of the CPA-1 nanofiber. Solid legends indicate MC at 14 tesla obtained from (a)– (c).

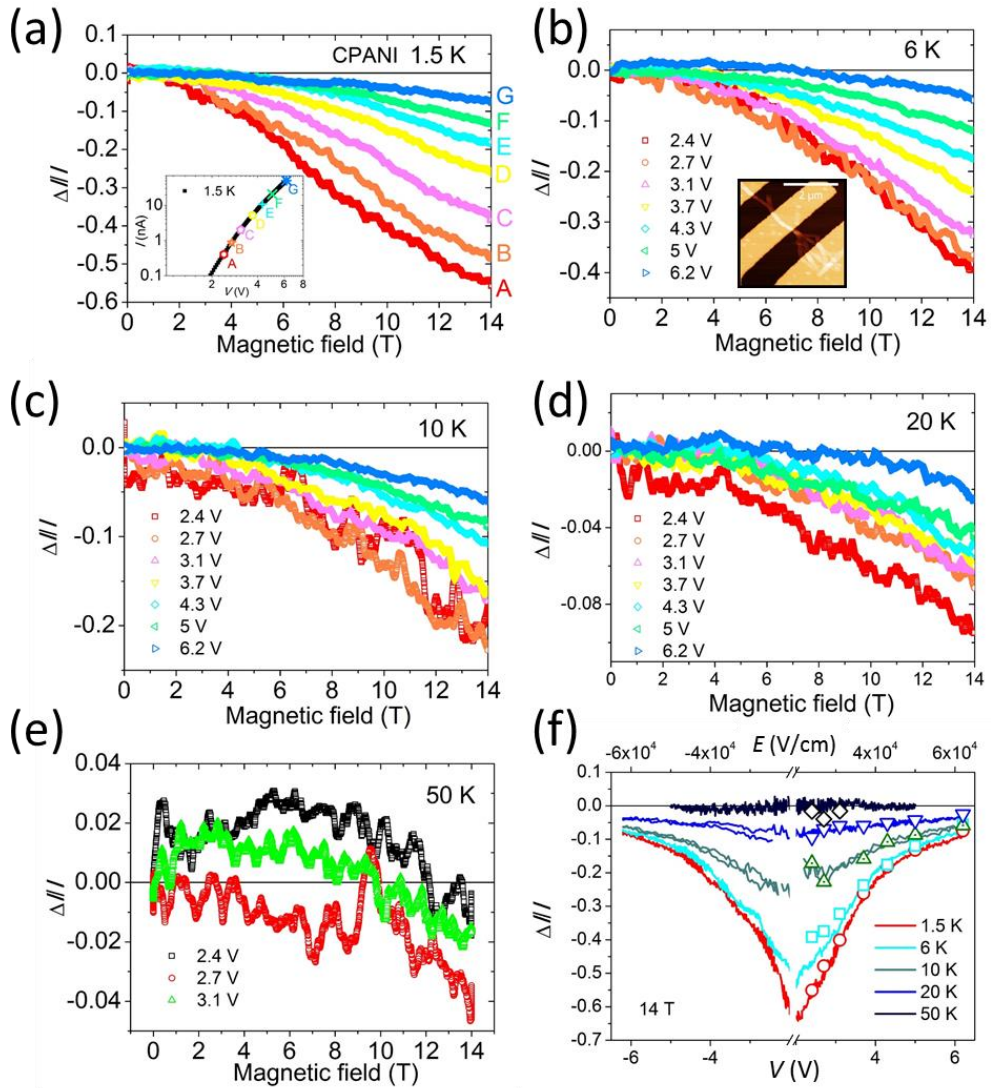


Figure 3.35 MC at fixed source-drain voltages of the CPANI nanofiber (CPANI-1) for (a) at 1.5 K, (b) 6 K, (c) 10 K, (d) 20 K, and (e) 50 K. Insets of (a) and (b) are the double logarithmic plot of I - V at 1.5 K and the AFM picture of the CPANI nanofiber device, respectively. A – G in (a) refer to each excitation voltage at 1.5 K. (A: 400 pA, 2.4 V; B: 900 pA, 2.7 V; C: 2 nA, 3.1 V; D: 5.2 nA, 3.7 V; E: 10 nA, 4.3 V; F: 20 nA, 5 V; G: 50 nA, 6.2 V). (f) MC at 14-tesla as a function of voltages at various temperatures. Open legends indicate MC at 14 tesla obtained from (a)– (e).

3.3.9 Comparison of Electrical Transport between Polymer Nanofibers and Carbonized Polymer Nanofibers

Less trivial to explain is the fact that the similarities of transport properties go beyond carbonized fibers and extend to pristine PA and PANI fibers, despite the fact that the macromolecular chain structure of polymers is dramatically modified after carbonization. Figure 3.36 shows a direct comparison of transport properties for both carbonized PA and PANI nanofibers and those of pristine polymers shown in ref. [16]. When transport measurements are plotted as $I/I_0 T^{1+\alpha}$ vs $\gamma eV/k_B T$, all curves from different polymer nanofibers show the same scaling behaviors before and after carbonization. We note that crossover of slopes in all scaled curves occur when $\gamma eV/k_B T \sim 1$, similar to those of polymer films in ref. [60].

The similarity of transport between pristine and carbonized polymer nanofibers suggests the need to revise the transport mechanism in pristine polymer nanofibers. The universal scaling, $I/T^{1+\alpha}$ vs $eV/k_B T$ observed in pristine polymer fibers^{15,16} was proposed as the evidence of 1D transport in polymer fibers, with the assumption that the building block for such nanofiber structures consist of inherently-1D polymer chains. In previous reports, authors propose that conductivity in pristine polymer nanofibers arises from of intra-chain transport (i.e. tunneling along 1D polymer chains), where each chain is a collection of Luttinger-liquid-like islands separated by intramolecular tunneling barriers^{15,16}. This conclusion was drawn solely from the observed power law variations of $G(T)$ and $I(V)$ and universal scaling, $I/T^{1+\alpha}$ vs $eV/k_B T$. However, in these systems is not obvious why in principle one should expect LL behavior, given that the pristine polymers are neither perfectly clean nor truly 1D, not to mention that the conditions for the fit to Eq. 2.1 in the context of LL, $\beta = \alpha + 1$ and $\gamma^{-1} = 1$, are not met^{15,16}. Polymer fibers differ from single molecule oligomers⁷¹ in that one fiber consists of large number of molecular chains stacked at best in polycrystalline structures. Moreover, and in comparison

with this work, the same universal scaling (Eq. 2.1) as well as the power law variations of $G(T)$ and $I(V)$ are observed in carbonized polymer fibers, in which the initially 1D polymer chains have undergone partial cross-linking upon pyrolysis forming quasi-amorphous networks of hexagonal carbon bonds (Fig. 3.3). The networking of polymer chains is expected to lessen the intra-chain transport (i.e. tunneling along 1D polymer chains), originally considered as transport mechanism in polymer nanofibers. Therefore, instead of tunneling of delocalized carriers along the polymer chains, proposed for pristine PA fibers^{15,16} transport in pristine polymers might as well occur due to hopping between localized states.

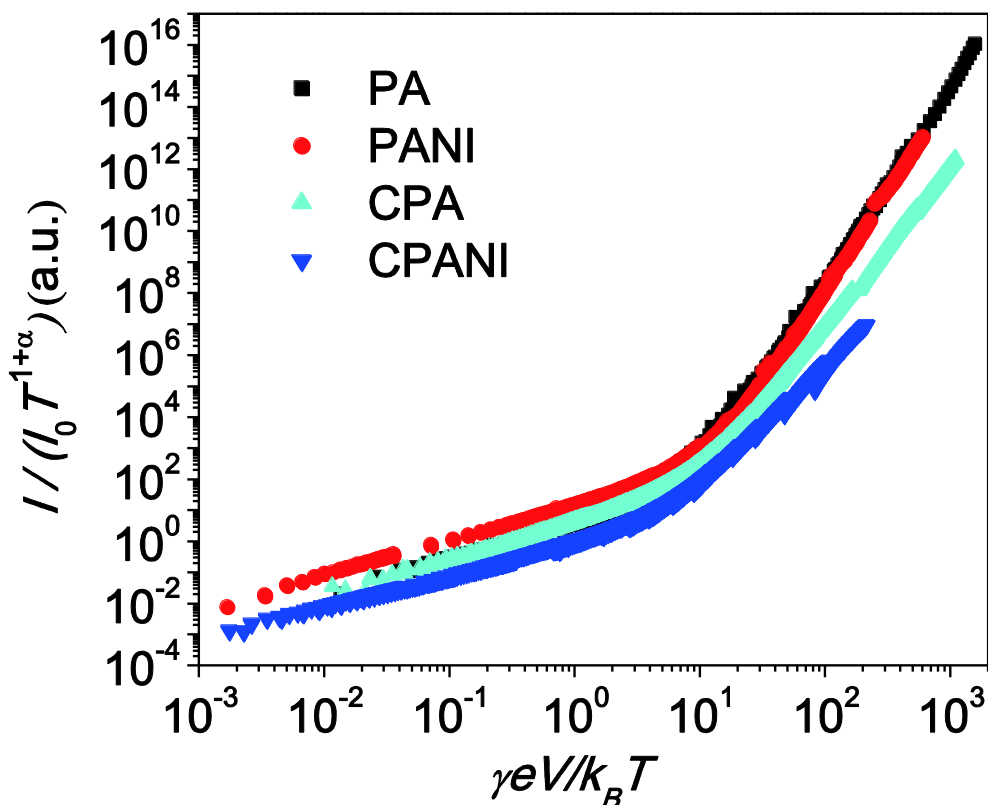


Figure 3.36 Comparison of universal scaling between pristine and carbonized polymer nanofibers. Normalized power law scaling $I/I_0 T^{1+\alpha}$ vs $\gamma e V/k_B T$ of both pristine and carbonized polymer nanofibers shows similar transport in these systems. Crossover of slopes in all scaled curves occur when $\gamma e V/k_B T \sim 1$

TABLE 3.1 Fitting parameters for pristine and carbonized polymer nanofibers

	α	β	$I_0 (A / K^{1+\alpha})$	γ^{-1}
PA ^a	5.47	6.88	4.9×10^{-23}	40
CPA	4.14	5.28	3.0×10^{-21}	100
PANI ^a	5.34	6.28	8.3×10^{-23}	303
CPANI	2.93	4.25	1.0×10^{-15}	205

^aref. [16].

Table 3.1 shows the fitting parameters of pristine and carbonized polymer nanofibers in the scaling of Fig. 3.36. The values of α and β are similar and order of magnitude similar values of γ^{-1} demonstrates common origin of transport in these systems. According to ref. [60], γ^{-1} in conjugated polymer films is proportional to the distance between source and drain electrodes which is 2 μm for PA and PANI, 500 nm for CPA, and 1 μm for CPANI.

In the hopping interpretation of transport in both pristine and carbonized polymer fibers, α and β are related to the dissipation coupling strength of an electron to the phonon bath; γ^{-1} is related to the number of hops needed for the charge carriers to traverse the distance between electrodes. Therefore, fitting parameters of Eq. 2.1 provides intuition for the charge transport of the system. Temperature and voltage dependence of conductance become faster as the coupling strength α and β increase because tunneling from metastable well slightly higher in energy is driven by the coupling to the phonon bath. Large number of γ^{-1} in carbonized fibers indicates large number of hops due to strong disorder. The

disordered structure presumably arises from defects during dehydrogenation and cross-linking processes. Moreover, the aromatic rings formed by carbonization are not crystallized yet. Therefore, order of magnitude comparable values of γ^{-1} in pristine polymers suggests that the structural disorder in stacking of molecular chains is significant.

According to the discussions in chapter 3.3.8, the MC of carbonized polymer nanofibers can be explained in the frame of VRH. Remarkably, the MC of pristine polymer nanofibers (Fig. 3.2) are qualitatively similar with that of carbonized polymer nanofibers. However, in the MC of pristine polymer nanofibers, the MC behaviors of PA and PANI nanofibers are different; i.e., the MC of PA nanofibers becomes zero and that of PANI is finite at high source-drain electric field¹⁶. This difference is interpreted as from the different chain structure of polymer nanofibers; i.e., degenerate (PA) and non-degenerate ground state polymer chain structures¹⁶. The difference of MC disappears in the carbonized polymer nanofibers presumably due to the carbonization process that destroys the difference between degenerate and non-degenerate ground states of polymer chains.

3.4 Conclusion

In conclusion, we have analyzed the transport data of the carbonized polymers in the framework of the ES-VRH and have compared charge transport in pristine and carbonized polymer nanofibers in the context of Eq. 2.1. Despite the different structure, confirmed by Raman spectroscopy, both types of materials give apparent power law dependence of current with voltage and temperature and scaling of all measurements into a single universal curve. The power law scaling in carbonized polymer nanofibers are interpreted as the manifestation of the ES-VRH in wide range of T and V parameters, which we suggest as the main transport mechanism of pristine polymer nanofibers as well.

Bibliography

1. V. N. Prigodin, and K. B. Efetov, Localization transition in a random network of metallic wires: A model for highly conducting polymers. *Phys. Rev. Lett.* **70**, 2932 (1993).
2. J. Tsukamoto, Recent advances in highly conductive polyacetylene. *Adv. Phys.* **41**, 509 (1992).
3. K. Akagi, *et al.* Helical Polyacetylene Synthesized with a Chiral Nematic Reaction Field. *Science* **282**, 1683 (1998).
4. M. Goh, M. Kyotani, and K. Akagi, Highly twisted helical polyacetylene with morphology free from the bundle of fibrils synthesized in chiral nematic liquid crystal reaction field. *J. Am. Chem. Soc.* **129**, 8519 (2007).
5. J. Huang, and S. Virji, Polyaniline nanofibers: facile synthesis and chemical sensors. *J. Am. Chem. Soc.* **125**, 314 (2003).
6. M. Kyotani, *et al.* Entanglement-free fibrils of aligned polyacetylene films that produce single nanofibers. *Nanoscale* **2**, 509 (2010).
7. H. D. Tran, Y. Wang, J. M. D'Arcy, and R. B. Kaner, Toward an understanding of the formation of conducting polymer nanofibers. *ACS Nano* **2**, 1841 (2008).
8. H. J. Lee, *et al.* Dispersion and current-voltage characteristics of helical polyacetylene single fibers. *J. Am. Chem. Soc.* **126**, 16722 (2004).
9. Y.-Z. Long, *et al.* Recent advances in synthesis, physical properties and applications of conducting polymer nanotubes and nanofibers. *Prog. Polym. Sci.* **36**, 1415 (2011).
10. Y. Long, *et al.* Electronic transport in single polyaniline and polypyrrole microtubes. *Phys. Rev. B* **71**, 165412 (2005).
11. A. Choi, *et al.* Suppression of the magneto resistance in high electric fields

- of polyacetylene nanofibers. *Synth. Met.* **160**, 1349 (2010).
12. J. G. Park, *et al.* Nanotransport in polyacetylene single fiber: Toward the intrinsic properties. *Synth. Met.* **119**, 53 (2001).
 13. A. B. Kaiser, and Y. W. Park, Comparison of tunnelling conduction in polyacetylene nanofibres, CDW and SDW systems. *Synth. Met.* **135–136**, 245 (2003).
 14. J. G. Park, *et al.* Tunneling conduction in polyacetylene nanofiber. *Synth. Met.* **135–136**, 299 (2003).
 15. A. N. Aleshin, H. J. Lee, Y. W. Park, and K. Akagi, One-dimensional transport in polymer nanofibers. *Phys. Rev. Lett.* **93**, 196601 (2004).
 16. A. Choi, *et al.* Probing spin-charge relation by magnetoconductance in one-dimensional polymer nanofibers. *Phys. Rev. B* **86**, 155423 (2012).
 17. M. Sassetti, and U. Weiss, Transport of 1D interacting electrons through barriers and effective tunnelling density of states. *Europhys. Lett.* **27**, 311 (2007).
 18. J. D. Yuen, *et al.* Nonlinear transport in semiconducting polymers at high carrier densities. *Nat. Mater.* **8**, 572 (2009).
 19. M. W. Bockrath, *et al.* Luttinger-liquid behavior in carbon nanotubes transport. *Science* **397**, 598 (1999).
 20. J. L. Bredas, and G. B. Street, Polarons, bipolarons and solitons in conducting polymers. *Acc. Chem. Res.* **18**, 309 (1985).
 21. A. J. Heeger, S. Kivelson, J. R. Schrieffer, and W. P. Su, Solitons in conducting polymers. *Rev. Mod. Phys.* **60**, 781 (1988).
 22. M. Kyotani, *et al.* Helical carbon and graphitic films prepared from iodine-doped helical polyacetylene film using morphology-retaining carbonization. *J. Am. Chem. Soc.* **130**, 10880 (2008).
 23. Z. Morávková, M. Trchová, M. Exnerová, and J. Stejskal, The carbonization of thin polyaniline films. *Thin Solid Films* **520**, 6088 (2012).

24. M. Trchová, E. N. Konyushenko, J. Stejskal, J. Kovářová, & G. Ćirić-Marjanović, The conversion of polyaniline nanotubes to nitrogen-containing carbon nanotubes and their comparison with multi-walled carbon nanotubes. *Polym. Degrad. Stab.* **94**, 929 (2009).
25. M. Trchová, *et al.* Structural and conductivity changes during the pyrolysis of polyaniline base. *Polym. Degrad. Stab.* **91**, 114 (2006).
26. Z. Rozlívková, M. Trchová, M. Exnerová, and J. Stejskal, The carbonization of granular polyaniline to produce nitrogen-containing carbon. *Synth. Met.* **161**, 1122 (2011).
27. S. Matsushita, M. Kyotani, and K. Akagi, Hierarchically controlled helical graphite films prepared from iodine-doped helical polyacetylene films using morphology-retaining carbonization. *J. Am. Chem. Soc.* **133**, 17977 (2011).
28. S. Matsushita, and K. Akagi, Macroscopically Aligned Graphite Films Prepared from Iodine-Doped Stretchable Polyacetylene Films Using Morphology-Retaining Carbonization. *J. Am. Chem. Soc.* **137**, 9077 (2015).
29. M. Kyotani, S. Matsushita, T. Nagai, Y. Matsui, and K. Akagi, Structural properties of carbon prepared from aligned polyacetylene thin films. *Synth. Met.* **157**, 546 (2007).
30. M. Kyotani, *et al.* Tubular-shaped nanocarbons prepared from polyaniline synthesized by a self-assembly process and their electrical conductivity. *J. Nanosci. Nanotechnol.* **8**, 1999 (2008).
31. A. Goto, *et al.* Structure of pyrolytic carbon from polyacetylene. *Carbon* **39**, 2082 (2001).
32. A. Goto, *et al.* Nanostructures of pyrolytic carbon from a polyacetylene thin film. *Carbon* **41**, 131 (2003).
33. C. A. Di, *et al.* Patterned graphene as source/drain electrodes for bottom-contact organic field-effect transistors. *Adv. Mater.* **20**, 3289 (2008).
34. W. Liu, *et al.* Large scale pattern graphene electrode for high performance in

- transparent organic single crystal field-effect transistors. *ACS nano* **4**, 3927 (2010).
35. Y. Cao, *et al.* High-performance photoresponsive organic nanotransistors with single-layer graphenes as two-dimensional electrodes. *Adv. Funct. Mater.* **19**, 2743 (2009).
 36. J. Jang, *et al.* Self-organizing properties of triethylsilylethynyl-anthradithiophene on monolayer graphene electrodes in solution-processed transistors. *Nanoscale* **5**, 11094 (2013).
 37. J. K. Park, *et al.* Graphene Gate Electrode for MOS Structure-based Electronic Devices. *Nano Lett.* **11**, 5383 (2011).
 38. J. Li, *et al.* A new exploration on the substantial improvement of rectifying behaviors for a donor-acceptor molecular diode by graphene electrodes. *Carbon* **61**, 284 (2013).
 39. F. Léonard, and A. A. Talin, Electrical contacts to one- and two-dimensional nanomaterials. *Nat. Nanotechnol.* **6**, 773 (2011).
 40. T. Pei, *et al.* Electronic transport in single-walled carbon nanotube/graphene junction. *Appl. Phys. Lett.* **99**, 113102 (2011).
 41. X. Huang, Z. Zeng, Z. Fan, J. Liu, and H. Zhang, Graphene-based electrodes. *Adv. Mater.* **24**, 5979 (2012).
 42. H. Shirakawa, T. Ito, and S. Ikeda, Raman scattering and electronic spectra of poly(acetylene). *Polym. J.* **4**, 460 (1973).
 43. G. A. Arbuckle, *et al.* Spectroscopic properties of polyacetylenes synthesized via three modifications of Ziegler-Natta catalytic system. *Synth. Met.* **79**, 183 (1996).
 44. A. Ferrari, and J. Robertson, Interpretation of Raman spectra of disordered and amorphous carbon. *Phys. Rev. B* **61**, 14095 (2000).
 45. J. Schwan, S. Ulrich, V. Batori, H. Ehrhardt, and S. Silva, Raman spectroscopy on amorphous carbon films. *J. Appl. Phys.* **80**, 440 (1996).

46. A. C. Ferrari, and J. Robertson, Raman spectroscopy of amorphous, nanostructured, diamond-like carbon, and nanodiamond. *Philos. Trans. A. Math. Phys. Eng. Sci.* **362**, 2477 (2004).
47. A. C. Ferrari, S. E. Rodil, and J. Robertson, Resonant Raman spectra of amorphous carbon nitrides: The G peak dispersion. *Diam. Relat. Mater.* **12**, 905 (2003).
48. A. Choi, *Magneto resistance of one-dimensional polymer nanofibers*. Ph. D. Thesis, Seoul National University (2012).
49. J. J. Langer, and S. Golczak, Highly carbonized polyaniline micro- and nanotubes. *Polym. Degrad. Stab.* **92**, 330 (2007).
50. B. I. Shklovskii, and A. L. Efros, *Electronic properties of doped semiconductors*. (1984).
51. N. F. Mott, and E. A. Davis, *Electronic processes in non-crystalline materials*. (1971).
52. A. L. Efros, and B. I. Shklovskii, Coulomb gap and low temperature conductivity of disordered systems. *J. Phys. C Solid State Phys.* **8**, L49 (1975).
53. H. Shinaoka, and M. Imada, Single-particle excitations under coexisting electron correlation and disorder: A numerical study of the anderson-hubbard model. *J. Phys. Soc. Jpn.* **78**, 094708 (2009).
54. D. Yu, C. Wang, B. L. Wehrenberg, and P. Guyot-Sionnest, Variable range hopping conduction in semiconductor nanocrystal solids. *Phys. Rev. Lett.* **92**, 216802 (2004).
55. V. N. Prigodin, and A. J. Epstein, Comment on ‘Voltage-Induced Metal-Insulator Transition in Polythiophene Field-Effect Transistors’. *Phys. Rev. Lett.* **98**, 259703 (2007).
56. A. S. Dhoot, G. M. Wang, D. Moses, and A. J. Heeger, Voltage-induced metal-insulator transition in polythiophene field-effect transistors. *Phys. Rev. Lett.* **96**, 246403 (2006).

57. M. Pollak, and I. A. Riess, Percolation treatment of high-field hopping transport. *J. Phys. C Solid State Phys.* **9**, 2339 (2001).
58. N. F. Mott, Introductory talk; Conduction in non-crystalline materials. *J. Non. Cryst. Solids* **8–10**, 1 (1972).
59. R. M. Hill, Hopping conduction in amorphous solids. *Philos. Mag.* **24**, 1307 (1971).
60. A. S. Rodin, and M. M. Fogler, Apparent power-law behavior of conductance in disordered quasi-one-dimensional systems. *Phys. Rev. Lett.* **105**, 106801 (2010).
61. L. Li, N. Lu, and M. Liu, Physical origin of nonlinear transport in organic semiconductor at high carrier densities. *J. Appl. Phys.* **116**, 164504 (2014).
62. H. Abdalla, K. van de Ruit, and M. Kemerink, Effective temperature and universal conductivity scaling in organic semiconductors. *Sci. Rep.* **5**, 16870 (2015).
63. A. A. Middleton, and N. S. Wingreen, Collective transport in arrays of small metallic dots. *Phys. Rev. Lett.* **71**, 3198 (1993).
64. R. Parthasarathy, X.-M. Lin, and H. M. Jaeger, Electronic transport in metal nanocrystal arrays: The effect of structural disorder on scaling behavior. *Phys. Rev. Lett.* **87**, 186807 (2001).
65. M. Akai-Kasaya, Y. Okuaki, S. Nagano, T. Mitani, and Y. Kuwahara, Coulomb blockade in a two-dimensional conductive polymer monolayer. *Phys. Rev. Lett.* **115**, 196801 (2015).
66. D. Joung, and S. I. Khondaker, Structural evolution of reduced graphene oxide of varying carbon sp^2 fractions investigated via coulomb blockade transport. *J. Phys. Chem. C* **117**, 26776 (2013).
67. K. A. Matveev, L. I. Glazman, P. Clarke, D. Ephron, and M. R. Beasley, Theory of hopping magnetoresistance induced by Zeeman splitting. *Phys. Rev. B* **52**, 5289 (1995).

68. A. Kurobe, and H. Kamimura, Correlation effects on variable range hopping conduction and the magnetoresistance. *J. Phys. Soc. Jpn* **51**, 1904 (1982).
69. S. V. Zaitsev-Zotov, Y. A. Kumzerov, Y. A. Firsov, and P. Monceau, Unconventional magnetoresistance in long InAs nanowires. *JETP Letters*. **77**, 135–139 (2003).
70. K. D. Bozdag, N. R. Chiou, V. N. Prigodin, and A. J. Epstein, Magnetic field, temperature and electric field dependence of magneto-transport for polyaniline nanofiber networks. *Synth. Met.* **160**, 271 (2010).
71. S. K. Lee, *et al.* Universal temperature crossover behavior of electrical conductance in a single oligothiophene molecular wire. *ACS Nano* **6**, 5078 (2012).

Chapter 4

Electrical Transport of Poly (2,5-dioctyloxy-*p*-phenylene vinylene-*alt*-3,4-ethylenedioxythiophene vinylene)

4.1 Introduction

Poly(arylenevinylene) polymers are an interesting class of materials having luminescence properties, well known for the light-emitting poly(*p*-phenylenevinylene) (PPV)¹. We prepared alternating copolymers containing phenylene-vinylene and electron rich 3,4-ethylenedioxythiophene (EDOT) units (poly (phenylene-vinylene-EDOT-vinylene), (PV-EDOTV) copolymer), which is the key monomer of the well-known conducting polymer mixture, PEDOT-PSS². Previously, alternating copolymer containing phenylene-vinylene and heterocycles are alternatively linked by vinylene unit has been reported as a polymer transistor with high mobility of 0.03 cm²/V•sec despite of amorphous structures³. In this study, the heterocycle was replaced by 3,4-EDOT unit, aiming higher electrical conductivity.

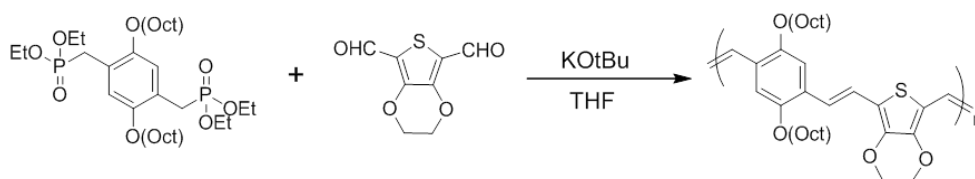


Figure 4.1 Synthesis scheme for the poly(phenylene-vinylene-EDOT-vinylene) copolymer.

We focus on interesting behaviors of MR on this material. MR, defined as $[\rho(B) - \rho(0)]/\rho(0)$, where ρ is the resistivity, and B is the magnetic field, is one of the most important tools used to study transport properties of conducting polymers⁴. Variable range hopping (VRH) among localized sites has been considered as the dominant transport mechanism in disordered conducting polymers⁵⁻⁷. In these systems, large and positive MR at cryogenic temperatures has been widely observed⁸ and explained in the frame of shrinkage of wave function in the presence of magnetic fields⁹ or the spin dependent hopping mechanism^{10,11}. Interestingly, negative MR has also been frequently observed at low temperatures in VRH systems in carbon nanotube¹², PANI nanocomposites¹³, magnetic nanoparticles in polymer matrix¹⁴, carbon nanotube aggregates¹⁵, and inorganic semiconductors such as CdTe¹⁶, Ni_xSi_{1-x}¹⁷, Indium Oxides¹⁸, InP¹⁹, CdAs₂²⁰, GaAs²¹, CuInSe₂²², and CdSe²³. The origin of the negative MR in VRH has attracted less attention compared with that of the positive MR. Moreover, the negative MR is not general and the reason of the presence and absence of the negative MR is still not well understood²⁴. The negative MR in VRH has been described in terms of quantum interference²⁵⁻²⁹: a quantum effect on transport in the strong localization regime. For the comprehensive understanding of MR in the VRH regime, further investigations are still required.

We investigate the MR of FeCl₃-doped (PV-EDOTV) copolymer in which EDOT and phenylene are alternatively linked by vinylene units at temperatures $T < 7$ K in magnetic field up to 35 T. The high magnetic field investigation reveals a crossover behavior of MR from negative to positive followed by exponential increase of the positive one at high magnetic field. The temperature dependence of conductivity displays the characteristic of the ES-VRH. The MR behavior is explained in the frame of the wave function shrinkage effect and the quantum interference effect within their theoretical validity.

4.2 Experimental

4.2.1 Sample Preparation

To synthesize the (PV-EDOTV) copolymer, anhydrous solvents and 1 M potassium *tert*-butoxide (*t*-BuOK) in THF were purchased from Sigma-Aldrich (Sigma-Aldrich Co., St. Louis, MO, USA). 1,4-bis(diethylphosphonatemethyl)-2,5-dioctyloxybenzene³⁰ and 3,4-ethylenedioxythiophene-2,5-dicarboxaldehyde³¹ were prepared using known methods. A solution of 1 M *t*-BuOK in THF was added dropwise to a flask charged with two monomers in THF solution. The reaction was refluxed for 12 h under an argon atmosphere. The polymerization reaction was quenched by the addition of aqueous ammonium chloride. After aqueous work-up, the polymer solution was precipitated into excess methanol, followed by a second precipitation into excess acetone. The filtered polymer was drop-casted in a glass substrate and dried overnight under vacuum. The thickness of the dried film was approximately 20 μm . The sample was synthesized by Tae-Lim Choi Laboratory in Department of Chemistry in SNU and I received it for the transport experiment.

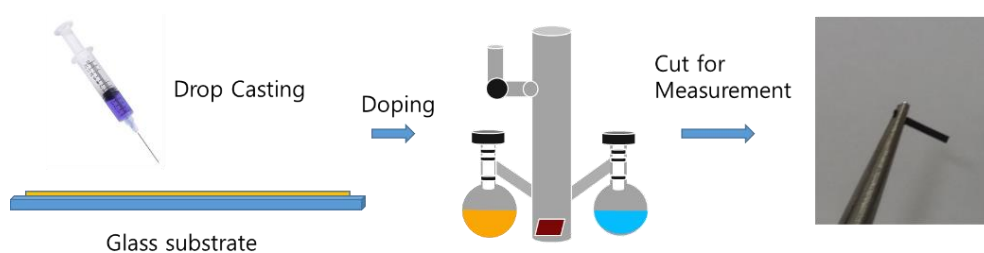


Figure 4.2 Schematics of drop casting of the polymer solution and subsequent solution doping. In the doping apparatus, one vessel is contained with FeCl_3 /nitromethane and the other with nitromethane for washing. The doped copolymer is cut for four-probe measurement.

4.2.2 Doping and Electrical Measurement

Anhydrous FeCl_3 powder was purchased from Sigma-Aldrich and used as received. 0.08 g of FeCl_3 powder was dissolved in 5 mL of nitromethane, and the pristine polymer film was immersed for 5 min in the 0.1 M FeCl_3 /nitromethane solution (Fig. 4.2) and washed with nitromethane several times. The pristine film was yellow in color but turned black during the doping process. The doped film was dried overnight in vacuum. All doping processes were conducted under argon atmosphere.

The high magnetic field measurements were performed at the National High Magnetic Field Laboratory, Tallahassee, up to 35 T, in DC field. The sample is cut by 5 mm x 2 mm x 20 μm . Gold wires were attached by carbon paste to the doped (PV-EDOTV) copolymer film, and the films were covered with N-grease (M&I Materials, Manchester, UK) to avoid exposure to air. The electrical conductivity was measured using the DC four-probe method. The MR was measured from the Ohmic regions of the I - V curves.

4.3 Results and Discussion

4.3.1 Pristine and Doped Copolymer

The pristine (PV-EDOTV) copolymer was found to be soluble in common organic solvents, such as THF, chloroform. The optical band-gap of the polymer, as measured by UV/Vis, was 1.9 eV and the HOMO level was 4.9 eV as measured by cyclic voltammetry (CV). The X-ray diffraction (XRD) of the pristine (PV-EDOTV) copolymer film shows that the polymer is almost amorphous. The electrical conductivity of the drop-casted pristine copolymer free standing film was $7.5 \times 10^{-7} - 9 \times 10^{-7}$ S/cm at room temperature and increased to 1 – 100 S/cm after FeCl_3 doping, corresponding to a $10^6 - 10^8$ times increase (Fig. 4.3). The weight percent of the dopant is 20 – 40 wt.% and density of the dopant is $\sim 10^{21} \text{ cm}^{-3}$.

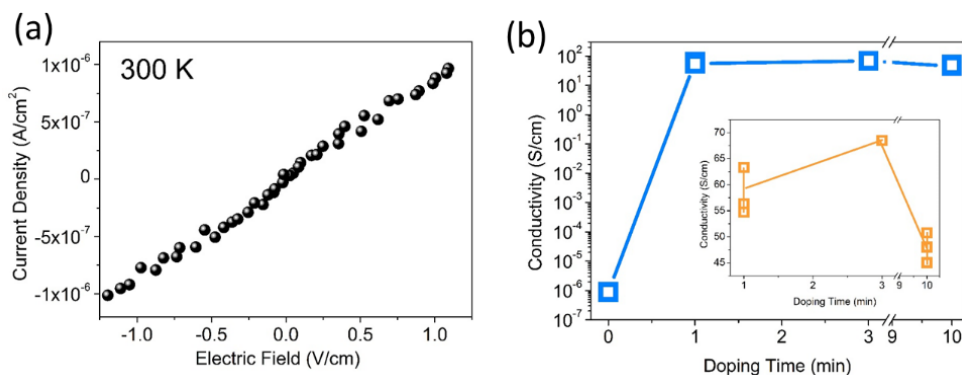


Figure 4.3 Current density vs electric field curve of a pristine polymer film (a) and doping time dependence of conductance (b). Inset of (b) shows conductivities of the (PV-EDOTV) copolymer doped for 1, 3, and 10 min. All measurements are conducted at room temperature in vacuum with four-probe geometry.

After FeCl₃ doping, the electronic state of the FeCl₃-doped (PV-EDOTV) copolymer film was investigated by X-ray photoemission spectroscopy (XPS). The XPS spectra of the Fe 2P_{3/2} peak was fitted by two main peaks at 711.1 eV and 709.9 eV, with two satellite peaks at 717.5 eV and 714.4 eV. These peaks are assigned to the Fe³⁺ of FeCl₄⁻ and Fe²⁺ of FeCl₂, respectively³². The chlorine 2P_{3/2} peak was decomposed to two peaks at 198.8 eV and 200.0 eV, where the peak at 198.8 eV (200 eV) is attributed to chlorine attached to FeCl₄⁻ or FeCl₂, and chlorine bonded to carbon³³, respectively. The existence of C-Cl bonding implies that the ion FeCl₄⁻ is attached to carbon by C-Cl bonding. Anhydrous FeCl₃ is known to exist as a dimer and undergoes dissociation in nitromethane solution to FeCl₄⁻ and FeCl₂⁺ (FeCl₃ = Fe(III)Cl₄⁻ + Fe(III)Cl₂⁺)³². The FeCl₂⁺ can be hydrated to FeCl₂ + nH₂O, which is insoluble in nitromethane³⁴. Figure 4.4(c,d) displays the presence of H₂O in the sample which can hydrate FeCl₂⁺. Therefore, we conclude that both FeCl₄⁻ and hydrated FeCl₂ are present in the FeCl₃-doped (PV-EDOTV) copolymer and that the charge transfers from FeCl₄⁻ attached to carbon is responsible for the increased conductivity observed after doping. We also observed the O-Fe bond [Fig. 4.4(d)].

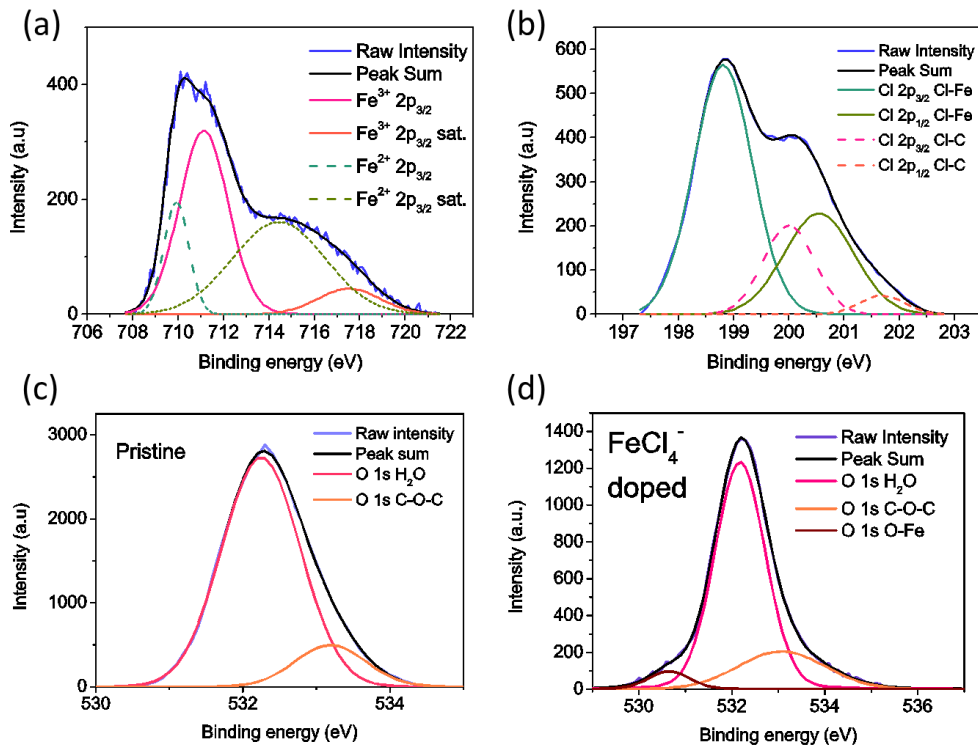


Figure 4.4 XPS spectra of pristine and FeCl₃-doped (PV-EDOTV) copolymer film. (a) The Fe 2p_{3/2} peak is decomposed into Fe³⁺ (solid) and Fe²⁺ (dashed) peaks. The Fe³⁺ and Fe²⁺ peaks originate from FeCl₄⁻ and FeCl₂, indicates that the sample is hole-doped. (b) The Cl 2p peak is decomposed into two sets of peaks, from Fe-Cl and C-Cl bonds, which indicates the presence of FeCl₄⁻, FeCl₂ and C-Cl bonding. (c) O 1s peak of pristine (PV-EDOTV) copolymer shows the presence of water and C-O-C bonds. The water is presumably absorbed during the peeling off process of dried film on glass substrates where the sample is immersed in water for peeling off. (d) After doping, O-Fe peak appears in the O 1s XPS peak.

4.3.2 Temperature Dependence of Conductivity

Figure 4.5 shows the conductivity of the FeCl₃-doped (PV-EDOTV) copolymer film as a function of temperature. The rapid decrease in conductivity at low temperatures is the characteristic of VRH among localized states, and the conductivity follows the Mott VRH equation, $\sigma = \sigma_0 \exp[-(T_0/T)^x]$, where σ_0 , T_0 , and x are constants^{9,35}. The

power, $x = 1/d+1$, is related to the sample dimensionality (d -dimension). FeCl₃ doped (PV-EDOTV) copolymer follows the Mott VRH with $x = 1/2$ though the sample is three-dimensional, as confirmed by the sample thickness measurement: 20 μm . The reduced activation energy $W = d \ln \sigma(T)/d \ln T$ is frequently used to obtain the value of the exponent x in the relation $\ln W = \ln(xT_0^x) - x \ln T$. Figure 4.5(b) shows the plot of $\ln W$ vs. $\ln T$ where the value of x is 0.55, confirming that the Mott VRH with $x = 1/2$. The functional dependence of 1D VRH which appears in 3D systems is explained by the ES-VRH^{9,36} where a parabolic soft energy gap known as the Coulomb gap with energy $\Delta_{\text{CG}} = k_{\text{B}}T_{\text{CG}}$ at the Fermi level plays important role. For the ES-VRH, the temperature dependence of the conductivity follows $\sigma = \sigma_0 \exp[-(T_0/T)^{1/2}]$ at $T < T_{\text{CG}}$, where $T_0 = \eta e^2/k_{\text{B}}\varepsilon\xi$ is the characteristic temperature, ε is the effective dielectric permittivity, ξ is the localization length, e is the electron charge, and η is a numerical constant with a value of 6.2 in 2-D and 2.8 in 3-D⁹. Figure 4.5(a) shows that the logarithmic plot of the conductivity versus $1/T^{1/2}$ is linear below ~ 70 K, with a slight deviation above ~ 70 K. T_0 is 270 K and $T_{\text{CG}} = 30$ K is estimated from $T_{\text{CG}} = T_0/\eta(4\pi)^{1/2}$ with $\eta = 2.8$.

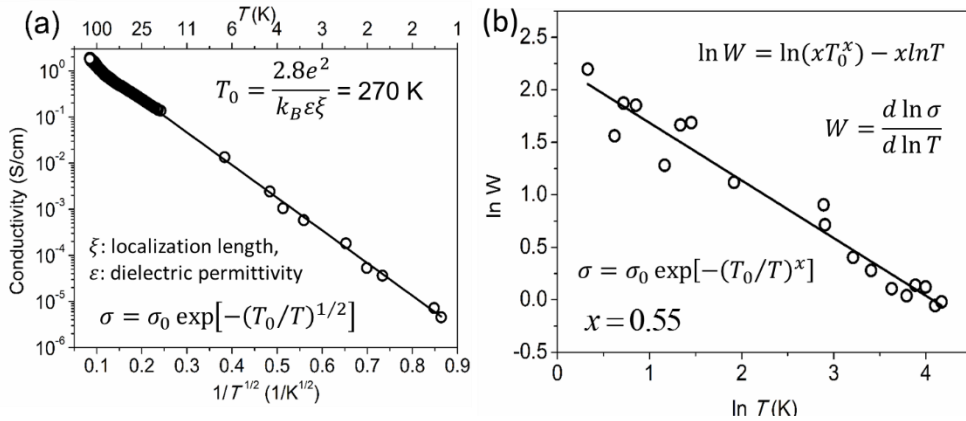


Figure 4.5 (a) The temperature-dependence of conductivity of the FeCl₃-doped (PV-EDOTV) copolymer film follows Coulomb gap VRH, satisfying $\sigma = \sigma_0 \exp[-(T_0/T)^{1/2}]$. (b) The plot of $\ln W$ vs. $\ln T$, shows the exponent of T . The solid line is a linear fit with a slope of -0.55, which confirms that the exponent of T is -1/2.

4.3.3 Magneto Resistance

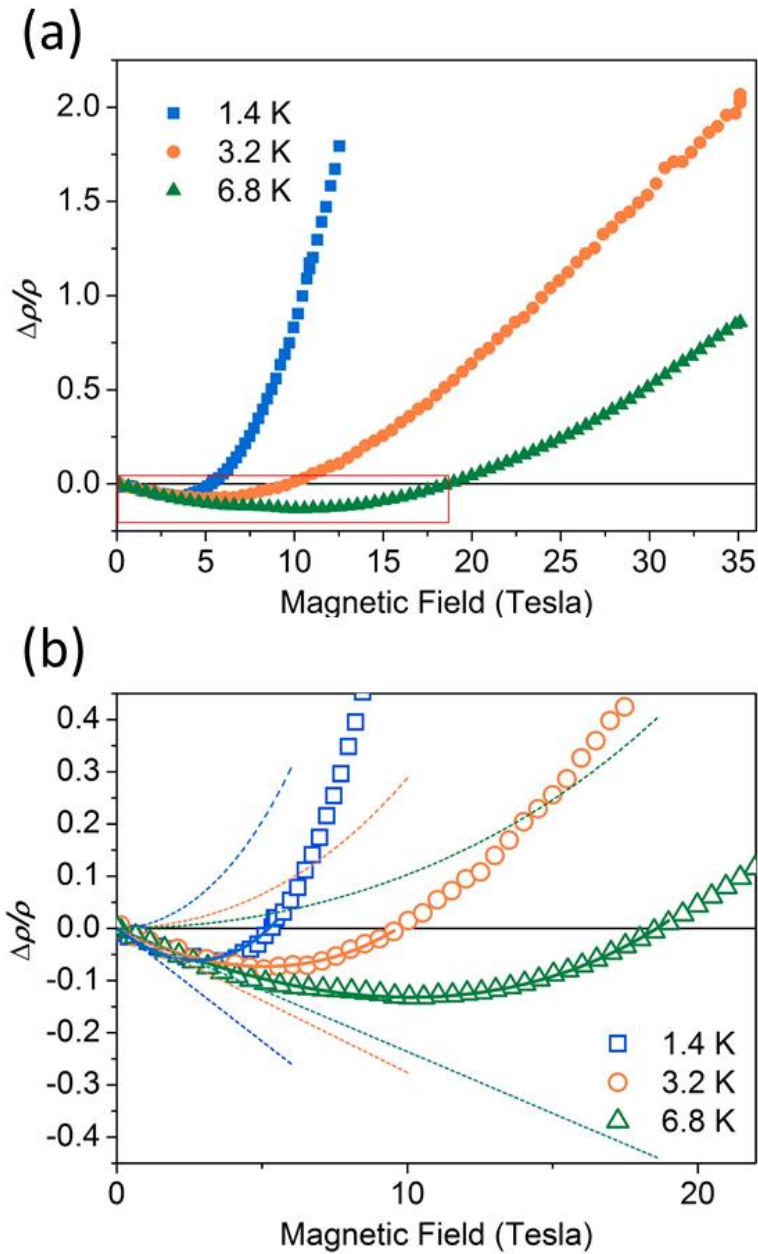


Figure 4.6 (a) MR of the FeCl₃-doped (PV-EDOTV) copolymer film at 1.4, 3.2, and 6.8 K up to 35 T. Negative MR is marked with a red box. (b) An expanded view of the crossover (red box in Fig. (a)). The solid lines are the fitting curves based on Eq. (4.2) and the dot lines are theoretical positive and negative contributions of the MR from wave function shrinkage and quantum interference, respectively.

Figure 4.6(a) shows the transverse MR of the FeCl₃-doped (PV-EDOTV) copolymer film up to 35 T at 1.4 K, 3.2 K, and 6.8 K. The sign of MR changes from negative to positive as the field increases. The magnetic field range where negative value of MR is observed decreases as temperature decreases. For sufficiently large magnetic fields, MR increases rapidly without saturation. No anisotropy observed up to 35 T. Figure 4.7 shows the change of resistance of the doped copolymer at 1.4 K due to magnetic field change from 0 T to 35 T. The resistance increased about 23 times by applying 35 T compared with the resistance at zero magnetic field. This means that the effect of magnetic field is stronger at low temperatures and that the positive MR continues to increase without saturation.

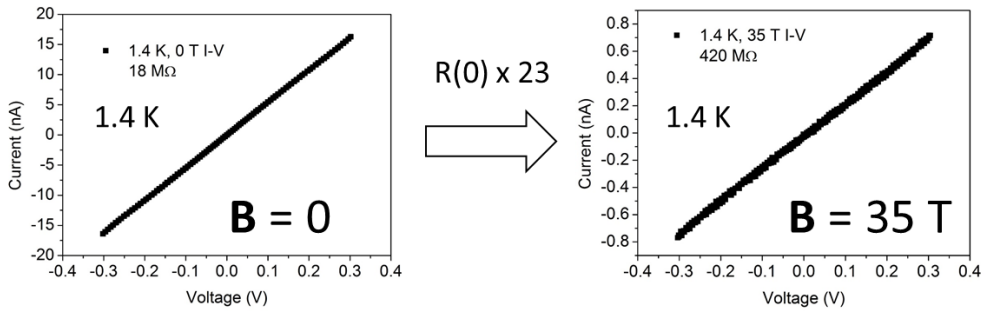


Figure 4.7 Resistance change at 1.4 K due to magnetic field 35 tesla. The resistance increases about 23 times (From $1.8 \times 10^7 \Omega$ to $4.2 \times 10^8 \Omega$).

We considered shrinkage of wave function due to magnetic field and the effect of spin alignment as possibilities of the positive MR. According to the literature, magnetic field retracts the wave function of localized electrons by the diamagnetic effect (chapter 2) and leads to positive MR:

$$\ln [\rho (H)/\rho (0)] = t (\zeta^4 / \lambda^4) (T_0/T)^p \quad (4.1)$$

, where $t = 0.0015$ and $p = 3/2$ for Coulomb gap VRH ($t = 5/2016$ and $p = 3/4$ for Mott's 3-D VRH), $\lambda = (\hbar/eH)^{1/2}$ is the magnetic length, H is the magnetic field, ρ is the resistivity, and ζ is the localization radius of the states⁹. The effect of spin

alignment is ruled out because when all spins are aligned, MR should saturate, which contradicts our data.

For the negative part of MR, we considered quantum interference models in VRH. These models explain the negative MR by breaking of destructive interferences in the presence of magnetic field. Nguyen *et. al.* considered quantum interference of multiple scattering paths connecting two hopping sites^{25,26}. From numerical simulations, they found that under certain conditions linear negative MR arises even ignoring the weak localization effect. Schirmacher²⁸ considered only one-site between the two hopping states, which is realistic for many cases, compared with the multiple scattering of Nguyen's model. He also derived linear negative MR. Sivan *et. al.*^{27,37} showed that, in the deep VRH regime, the MR is quadratic in magnetic field at low field and becomes linear at intermediate fields, followed by saturation at strong fields ($Hr^{3/2}\xi^{1/2} \gg h/e$). Raikh and Wessels²⁹ considered only a few scatterings between hopping sites in a single hop and also obtained the similar behavior as the magnetic field increases. The model of Fukuyama and Yoshida³⁸ considered the repopulation of localized states in the presence of magnetic field due to Zeeman shift as the origin of the negative MR in VRH. However, this model does not fit our data well.

If we assume that the two negative and positive contributions are additive, as tried in previous literatures^{12,15-17}, the total MR is given by

$$[\rho(H) - \rho(0)] / \rho(0) = \alpha(T)H + \exp(\beta(T)H^2) - 1 \quad (4.2)$$

, where $\alpha(T)$ and $\beta(t)$ are negative and positive temperature-dependent fitting parameters. Equation 4.2 is the sum of the linear negative contribution from the wave function interference and the positive contribution due to the effect of shrinking wave function. The fitting of MR by Eq. 4.2 is shown in Fig. 4.6(b), which agrees well with the data. For low fields, the negative hopping MR predicts both linear^{25,28,39} and

quadratic^{27,29,37} dependence. However, the negative contribution is approximately represented as a linear term because it is difficult to determine from our data whether the negative contribution of MR possesses a quadratic dependence [Fig. 4.6(b)], and because quadratic dependence is expected only in exponentially small magnetic fields^{28,29}. From this analysis, it is understood that the crossover results from the competition between the quantum interference effect and the wave function shrinkage effect in the presence of magnetic fields: The effect of quantum interference dominates at low magnetic fields, raising negative MR, which crosses over to positive values as the wave function shrinkage reduces the overlap of localized wave functions significantly at higher magnetic fields.

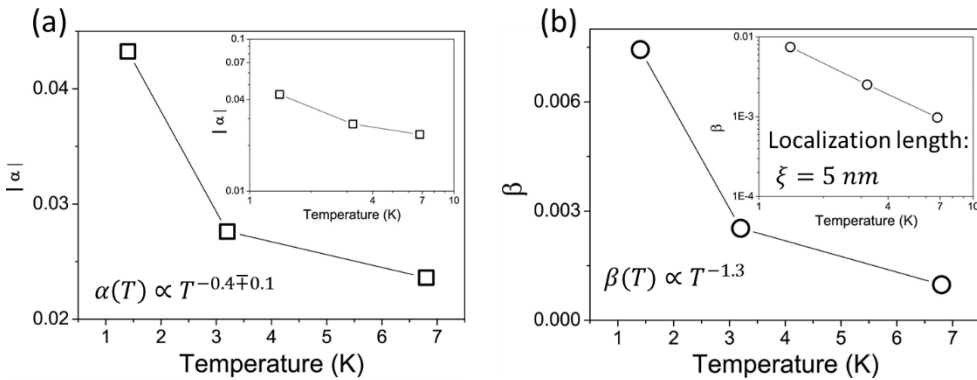


Figure 4.8 The temperature-dependence of fitting parameters $|\alpha|$ and $\beta(t)$ in Eq. (2) obtained from the fit of Fig. 4.7(b). Insets are represented by the log-log scale, indicating the power law behavior of α and β as a function of temperature. Localization length 5 nm is obtained.

In the analysis of the fitting parameters, it is found that $|\alpha| \propto 1/T^{0.4 \pm 0.1}$, in agreement with the values in literatures where the parameter $|\alpha|$ is expected to follow a power law dependence of $1/T^s$ with $s = 7/8$ ²⁸ and $s = 1/2$ or $s = 1$ ²⁹ in the regime of linear MR. The quantum interference is more active at lower temperatures as seen from the temperature dependence of $|\alpha|$, though the magnitude

of the negative MR decreases at low temperatures. In the temperature dependence of β , the power law relation of $\beta \propto T^p$ with $p = 1.3$ is close to the expected dependence of $\beta \propto T^p$ with the exponent $p = 1.5$ (Eq. 4.1). This result is consistent with the presence of a Coulomb gap in the analysis of temperature-dependence of conductivity. The localization length calculated from the intercept of the logarithmic plot of $\beta(T)$ is 5.3 nm. Substitution of ζ for 5.3 nm and T_0 for 270 K in the expression $T_0 = \eta e^2 / k_B \epsilon \zeta$ gives dielectric constant $\epsilon_r = 33$. The density of states $N(E_F)$ is obtained from $\epsilon = 4\pi e^2 N(E_F) \zeta^2$, gives the Coulomb gap energy $\Delta_{CG} = e^3 N(E_F)^{1/2} / \epsilon^{3/2} = k_B T_{CG}$ about 30 K⁴⁰. This value is in good agreement with the T_{CG} value of 30 K obtained from $T_{CG} = T_0 / \eta (4\pi)^{1/2}$ with $\eta = 2.8$ (See chapter 4.3.2), indicating that the value of localization length obtained from the MR analysis based on adding the two positive and negative contributions is reasonable.

The fitting of Eq. 4.2 is successful only within the limited range of magnetic fields. According to Shklovskii and Spivak³⁹, the linear approximation for negative MR is valid for $H < \pi \hbar / r^{3/2} \zeta^{1/2} e$, where r is the average hopping distance. The average hopping length is estimated from $r = 0.25 \zeta (T_0/T)^{1/2}$, which is 10 nm at 6.8 K and 20 nm at 1.4 K⁴⁰. Therefore, at 1.4, 3.2, and 6.8 K, the upper limit of the magnetic field is 11, 20, and 31 T, respectively. We fit the negative MR below 5.4, 9.6, and 18.6 T for 1.4, 3.2, and 6.8 K, respectively, which is below the limiting field. For the positive contribution, Eq. 4.1 is valid for $H < 6\hbar / [e \zeta^2 (T_0/T)^{1/2}]^{9,17}$. The upper limit is 10, 14, and 19 T, at 1.4, 3.2, and 6.8 K, respectively. Thus, fitting of Eq. 4.2 is performed within the theoretical limits of the magnetic fields [Fig. 4.6(b)].

4.4 Conclusion

We synthesized copolymers based on phenylene-vinylene and EDOT-vinylene units which is solution processible and capable with doping. In the FeCl_3 -doped (PV-EDOTV) copolymer films, charge transfer from FeCl_3 to the copolymer gives 10^7 times increase after doping. The FeCl_3 -doped (PV-EDOTV) copolymer displays the ES-VRH behavior of temperature dependence of conductivity where the MR at $T < 7$ K shows crossover from negative to positive values. This MR arises from the interplay of the quantum interference of scattered electrons in the course of tunneling and the effect of magnetic field to the localized electron wave function. The effect of quantum interference dominates at low magnetic fields, resulting in negative MR, which crosses over to positive values as the wave function shrinkage reduces the overlap of localized wave functions significantly.

Bibliography

1. J. H. Burroughes, *et al.* Light-emitting diodes based on conjugated polymers. *Nature* **347**, 539 (1990).
2. L. Groenendaal, F. Jonas, D. Freitag, H. Pielartzik, and J. R. Reynolds, Poly(3,4-ethylenedioxythiophene) and its derivatives: past, present, and future. *Adv. Mater.* **12**, 481 (2000).
3. T. L. Choi, *et al.* High Performance Organic Thin-Film Transistor based on Amorphous A, B-Alternating Poly(arylenevinylene) Copolymers. *Macromolecules* **43**, 6045 (2010).
4. A. Choi, *et al.* Probing spin-charge relation by magnetoconductance in one-dimensional polymer nanofibers. *Phys. Rev. B* **86**, 155423 (2012).
5. R. Menon, Conductivity and magnetoconductance in iodine-doped polyacetylene. *Synth. Met.* **80**, 223 (1996).
6. J. F. Kwak, T. C. Clarke, R. L. Greene, and G. B. Street, Transport properties of heavily AsF₅ doped polyacetylene. *Solid State Commun.* **31**, 355 (1979).
7. Y. W. Park, Magneto resistance of polyacetylene nanofibers. *Chem. Soc. Rev.* **39**, 2428 (2010).
8. T. A. Skotheim, and J. R. Reynolds, *Handbook of conducting polymers: conjugated polymers processing and applications.* (2007).
9. B. I. Shklovskii, and A. L. Efros, *Electronic properties of doped semiconductors.* (1984).
10. A. Kurobe, and H. Kamimura, Correlation effects on variable range hopping conduction and the magnetoresistance. *J. Phys. Soc. Jpn* **51**, 1904 (1982).

11. K. A. Matveev, L. I. Glazman, P. Clarke, D. Ephron, and M. R. Beasley, Theory of hopping magnetoresistance induced by Zeeman splitting. *Phys. Rev. B* **52**, 5289 (1995).
12. M. Jaiswal, W. Wang, K. A. S. Fernando, Y.-P. Sun, and R. Menon, Magnetotransport in transparent single-wall carbon nanotube networks. *Phys. Rev. B* **76**, 113401 (2007).
13. J. Zhu, *et al.* Carbon nanostructure-derived polyaniline metacomposites: Electrical, dielectric, and giant magnetoresistive properties. *Langmuir* **28**, 10246 (2012).
14. S. Shekhar, V. Prasad, and Subramanyam, S. V. Quantum interference effect in strongly localized system of polymer-nanocomposites. *Phys. Lett. Sect. A* **371**, 486 (2007).
15. M. Salvato, *et al.* Low temperature conductivity of carbon nanotube aggregates. *J. Phys. Condens. Matter* **23**, 475302 (2011).
16. N. V. Agrinskaya, and V. I. Kozub, Suppression of negative magnetoresistance in Coulomb gap regime: quantum interference and spin effects in CdTe. *Phys. Stat. Sol* **205**, 11 (1998).
17. R. Rosenbaum, T. Murphy, E. Palm, S. Hannahs, and B. Brandt, Magnetoresistance of insulating amorphous $\text{Ni}_x\text{Si}_{1-x}$ films exhibiting Mott variable-range hopping laws. *Phys. Rev. B* **63**, 94426 (2001).
18. Z. Ovadyahu, Anisotropic magnetoresistance in a Fermi glass. *Phys. Rev. B* **33**, 6552 (1986).
19. R. Abdia, A. El Kaaouachi, A. Nafidi, G. Biskupski, and J. Hemine, Variable range hopping conductivity and negative magnetoresistance in n-type InP semiconductor. *Solid. State. Electron.* **53**, 469 (2009).

20. G. Giskupski, Positive and negative magnetoresistance in the variable-range-hopping regime of doped semiconductors. *Philos. Mag. B* **65**, 723 (1992).
21. F. Tremblay, *et al.* Negative magnetoresistance in the variable-range-hopping regime in n-type GaAs. *Phys. Rev. B* **39**, 8059 (1989).
22. J. Essaleh Galibert, S. M. Wasim, E., L. J. Hernandez, Low-field negative magnetoresistance in the variable-range-hopping regime in copper indium diselenide. *Phys. Rev. B* **50**, 40 (1994).
23. Y. P. Zhang, and M. Sarachik, Negative magnetoresistance in the variable-range-hopping regime in n-type CdSe. *Phys. Rev. B* **43**, 7212 (1991).
24. P. Dai, R. Jonathan, R. Friedman, and M. P. Sarachik, Hopping conduction in doped silicon: The apparent absence of quantum interference. *Phys. Rev. B* **48**, 4875 (1993).
25. V. L. Nguyen, B. Z. Spivak, and B. I. Shklovskii, Aaronov-Bohm oscillations with normal and superconducting flux quanta in hopping conductivity. *JETP Lett.* **41**, 42 (1985).
26. V. L. Nguen, B. Z. Spivak, and B. I. Shklovskii, Tunnel hopping in disordered systems. *Sov. Phys. JETP* **62**, 1021 (1985).
27. U. Sivan, O. Entin-Wohlman, and Y. Imry, Orbital magnetoconductance in the variable range hopping regime. *Phys. Rev. Lett.* **60**, 1566 (1988).
28. W. Schirmacher, Quantum-interference magnetoconductivity in the variable-range-hopping regime. *Phys. Rev. B* **41**, 2461 (1990).
29. M. E. Raikh, and G. F. Wessels, Single-scattering-path approach to the negative magnetoresistance in the variable-range-hopping regime for two-dimensional electron systems. *Phys. Rev. B* **47**, 15609 (1993).

30. A. K. Mohanakrishnan, A. Hucke, M. A. Lyon, M. V. Lakshmikantham, and M. P. Cava, Functionalization of 3,4-ethylenedioxythiophene. *Tetrahedron* **55**, 11745 (1999).
31. H. Detert, D. Schollmeyer, and E. Sugiono, Synthesis, structure and solvatochromism of the emission of cyano-substituted oligo(phenylenevinylene)s. *European J. Org. Chem.* **2001**, 2927 (2001).
32. A. Furlani, *et al.* Spectroscopic studies of FeCl₃-doped polymers of polyphenylacetylene. *Appl. Spectrosc.* **44**, 331 (1990).
33. M. V. Russo, G. Polzonetti, and A. Furlani, XPS and IR investigations of FeCl₃-doped polyphenylacetylene: the solvent effect. **39**, 291 (1991).
34. A. Pron, *et al.* Comments on Magnetic phase transition, aggregate formation, and electrical conductivity in FeCl₃-doped polyacetylene. *Phys. Rev. B* **31**, 4690 (1985).
35. N. F. Mott, and E. A. Davis, *Electronic processes in non-crystalline materials.* (1971).
36. A. L. Efros, and B. I. Shklovskii, Coulomb gap and low temperature conductivity of disordered systems. *J. Phys. C Solid State Phys.* **8**, L49 (1975).
37. O. Entin-Wohlman, Y. Imry, and U. Sivan, Orbital magnetoconductance in the variable-range-hopping regime. *Phys. Rev. B* **40**, 8342 (1989).
38. H. Fukuyama, K. Yoshida, Negative magnetoresistance in the Anderson localized states. *J. Phys. Soc. Jpn* **46**, 102 (1979).
39. B. I. Shklovskii, and B. Z. Spivak, *Scattering and Interference Effects in Variable Range Hopping Conduction.* (1991).
40. M. Pollak, & B. I. Shklovskii, *Hopping Transport in Solids.* (1991).

Chapter 5

Conclusion

In this dissertation, electrical transport properties of carbonized polymer nanofibers and a (PV-EDOTV) copolymer are probed. Comparing electrical transport between pristine and carbonized polymer nanofibers, transport via hopping of localized carriers with Coulomb interaction is argued as the main transport mechanism in conjugated polymer nanofibers. This means that the disorder in polymer nanofibers is significant enough to localize charge carriers. Moreover, similar transport between pristine and carbonized polymer nanofibers refutes the transport along LL islands connected by intra-junction tunnel barriers originally proposed in pristine polymer nanofibers. In the electrical transport study of FeCl₃-doped (PV-EDOTV) copolymer, similar hopping transport with Coulomb interaction was observed. Therefore, the ES-VRH is common in both nanofibers and the conjugated copolymer film.

Interesting are magneto-transport behaviors in these VRH polymer conductors. In carbonized polymer nanofibers, negative MC (i.e., positive MR) is explained by the shrinkage of wave function in the magnetic field and the electric field dependence of MR is interpreted as the manifestation of reduced hopping length due to the electric field. In the FeCl₃-doped (PV-EDOV) copolymer, crossover of MR from negative to positive values is analyzed in terms of the competition between quantum interference during forward hopping which gives negative MR and the effect of magnetic field on the localized electron wave function causing positive MR. At low magnetic field, the negative contribution dominates the overall MR, which eventually turns to positive MR due to the significant reduction of overlap arising from shrinkage of the wave function by the diamagnetic effect of the magnetic field.

요약 (국문 초록)

김 경 호

서울대학교

자연과학대학 대학원

물리천문학부

고분자 나노 섬유의 전기 전도와 탄화 (carbonization, 炭化)된 고분자 나노 섬유의 전기 전도를 비교함으로써 고분자 나노 섬유의 전기 전도를 논의하였다. 또한 새롭게 합성된 공중합체 (copolymer, 共重合體)의 전기 전도 특성을 조사하였다. 원칙적으로 본 연구에 사용된 폴리아세틸렌, 폴리아닐린과 같은 전도성 고분자 나노 섬유는 고유의 1차원 사슬 (chain) 구조로 인해 1차원 전도체 연구의 시험대가 되어왔다. 하지만 구조적인 불규칙성으로 인해 전도성 고분자 나노 섬유의 전기 전도를 잘 정의된 전도 모델들로 설명하는 데에 어려움이 있다. 우리는 고분자 나노 섬유의 1차원 사슬을 800 °C의 높은 온도에서 탄화하여 1차원 사슬 구조에 변화를 준 후 탄화 전·후 나노 섬유의 전기 전도를 비교하였다. 탄화된 고분자 나노 섬유의 라만 분광 스펙트럼에서는 흑연의 D와 G 밴드가 넓게 나타나는데 이로부터 벤젠 고리가 거의 무정형 (almost amorphous, 無定形)의 탄소 덩어리 속에 불규칙적으로 분포하고 있는 구조임을 알 수 있다. 이것은 탄화 과정에 의해 1차원 분자들이 교차 결합한 증거이며 이러한 교차 결합에 의해 전도성 고분자 나노 섬유에서 제안되었던 집단적인 전기 전도 즉, 1차원 고분자 사슬의 루틴저 액체(Luttinger liquid) 섬 (islands) 들이 사슬 내 터널링 장벽 (tunneling barriers)을 터널링 (tunneling) 하는 전하

수송 메커니즘이 탄화 이후에는 적용되지 않을 것으로 예상된다. 그러나 우리는 넓은 범위의 온도 및 전기장에서의 전류-전압 곡선 측정 결과 탄화 전과 후에서 유사한 전기 전도 모습을 발견하였다. 전기 에너지가 열 에너지보다 매우 작은 낮은 전압에서 보이는 선형적인 전도도와 전기 에너지가 열 에너지보다 매우 큰 전압에서 보이는 비선형적인 전도도는 에프로스-슈클로프스키 (Efros-Shklovskii)의 변덕버렁 깡충뛰기 (variable range hopping) 전도 모델의 특성을 보이는데, 이것은 또한 멱급수 (power law, 冪級數)의 선형 전도도-온도, 비선형 전류-전압의 관계를 보인다. 또한 두 종류의 탄화된 고분자 나노 섬유는 측정된 전류-전압 곡선이 하나의 보편(universal, 統括)적인 멱급수 곡선으로 모이는 특성을 보인다. 이 보편적인 곡선은 열 에너지로 규격화(normalize, 規格化)된 전류를 열 에너지로 규격화된 전기 에너지에 대해 나타내었을 때 멱급수 관계를 보인다. 또한 전기 에너지가 열 에너지와 비슷하게 되는 전압에서 선형 전도에서 비선형 전도로의 전환이 곡선의 기울기의 변화로 나타난다. 전도성 고분자 나노 섬유에서 1차원 전자 액체인 루틴저 액체의 가능성은 이들 전도성 고분자 나노 섬유가 1차원 사슬 구조라는 것과 이들에서 멱급수 보편 스케일링(power law universal scaling) 및 멱급수 전도 특성이 관측된다는 것에 의존하고 있다. 하지만 탄화 이후에도 이러한 특성이 유지되는 것은 전도성 고분자 나노 섬유의 루틴저 액체 전도의 근거가 명확하지 않음을 보여준다. 이와 같이 에프로스-슈클로프스키의 가변 거리 뛰기 전도에서 통괄적인 멱급수 법칙이 성립하는 것과 탄화된 고분자 나노 섬유에서 보편적인 멱급수 법칙이 성립하는 것은 본 연구의 중요한 발견이다. 이 발견은 이 멱급수 스케일링 이면의 물리를 이해하는 것과 고분자 나노 섬유의 전기 전도를 이해하는 데에 중요하다. 에프로스-

슈클로프스키 변덕버렁 깡충뛰기에서 멱급수 보편 스케일링이 나타나는 것은 꼭 루틴저 액체가 아니라 에프로스-슈클로프스키 변덕버렁 깡충뛰기에서도 보편 스케일링이 나타날 수 있다는 것을 보여준다. 탄화 전·후 고분자 나노 섬유에서 유사한 전기 전도를 보인다는 것은 고분자 나노 섬유의 전기 전도 역시 에프로스-슈클로프스키 변덕버렁 깡충뛰기 메커니즘에 의한 것임을 시사한다.

탄화된 고분자 나노 섬유의 자기 (magnetic, 磁氣) 수송에서 우리는 음의 자기 전도도, 즉 자기장 하에서는 자기장이 없을 때에 비해 전기 전도도가 감소하는 것을 발견하였는데 자기 전도도의 크기는 양 단자에 걸리는 전압과 온도가 증가함에 따라 감소한다. 우리는 외부 전기장이 세 짐에 따라 뛰는 거리가 감소하는 것이 높은 전기장에서 낮은 전기장일 때에 비해 자기 전도도의 크기를 감소시킨다고 분석하였으며 탄화된 고분자 나노 섬유의 자기 수송 특성은 전반적으로 변덕버렁 깡충뛰기 전도 분석을 지지한다.

염화제이철이 도핑된 공중합체의 자기 저항은 자기장이 증가함에 따라 음의 자기 저항 (자기장이 없을 때에 비해 자기장이 있을 때 저항이 감소)에서 양의 값 (자기장이 없을 때에 비해 자기장이 있을 때 저항 증가)으로 교차한다. 전기 전도도의 온도 의존성은 에프로스-슈클로프스키 변덕버렁 깡충뛰기 모델을 따른다. 자기 저항의 교차는 전자가 한 번 깡충 뛸 때 (hopping) 가능한 여러 터널링 경로들이 서로 간섭하는 효과와 자기장에 의해 국소화된 전자의 파동 함수가 수축하는 효과의 경쟁에 의한 것으로 분석된다. 낮은 자기장에서는 간섭 효과가 주도적이고 파동 함수의 수축이 현저하지 못하기 때문에 음의 자기 저항이 나타나고 높은 자기장에서는 파동 함수의 수축이 전기 전도의

변화를 주도하게 되어 양의 자기 저항이 나타난다.

.....
주요어: 전도성 고분자 나노 섬유, 탄화, 변덕버링 강충뛰기, 전도도의
보편 스케일링, 피닐린-비닐린-에틸렌디옥시타이오펜-비닐린 공중합체,
자기-수송

학번: 2009-22960